ANL/LWRS-14/02

Online Stress Corrosion Crack and Fatigue Usages Factor Monitoring and Prognostics in Light Water Reactor Components: Probabilistic Modeling, System Identification and Data Fusion Based Big Data Analytics Approach

Nuclear Engineering Division

About Argonne National Laboratory
Argonne is a U.S. Department of Energy laboratory managed by UChicago Argonne, LLC under contract DE-AC02-06CH11357. The Laboratory's main facility is outside Chicago, at 9700 South Cass Avenue, Argonne, Illinois 60439. For information about Argonne and its pioneering science and technology programs, see www.anl.gov.

DOCUMENT AVAILABILITY

Online Access: U.S. Department of Energy (DOE) reports produced after 1991 and a growing number of pre-1991 documents are available free via DOE's **SciTech Connect** (http://www.osti.gov/scitech/)

Reports not in digital format may be purchased by the public from the National Technical Information Service (NTIS):

U.S. Department of Commerce
National Technical Information Service
5301 Shawnee Rd
Alexandra, VA 22312
www.ntis.gov
Phone: (800) 553-NTIS (6847) or (703) 605-6000
Fax: (703) 605-6900
Email: **orders@ntis.gov**

Reports not in digital format are available to DOE and DOE contractors from the Office of Scientific and Technical Information (OSTI):

U.S. Department of Energy
Office of Scientific and Technical Information
P.O. Box 62
Oak Ridge, TN 37831-0062
www.osti.gov
Phone: (865) 576-8401
Fax: (865) 576-5728
Email: **reports@osti.gov**

Disclaimer
This report was prepared as an account of work sponsored by an agency of the United States Government. Neither the United States Government nor any agency thereof, nor UChicago Argonne, LLC, nor any of their employees or officers, makes any warranty, express or implied, or assumes any legal liability or responsibility for the accuracy, completeness, or usefulness of any information, apparatus, product, or process disclosed, or represents that its use would not infringe privately owned rights. Reference herein to any specific commercial product, process, or service by trade name, trademark, manufacturer, or otherwise, does not necessarily constitute or imply its endorsement, recommendation, or favoring by the United States Government or any agency thereof. The views and opinions of document authors expressed herein do not necessarily state or reflect those of the United States Government or any agency thereof, Argonne National Laboratory, or UChicago Argonne, LLC.

ANL/LWRS-14/02

Online Stress Corrosion Crack and Fatigue Usages Factor Monitoring and Prognostics in Light Water Reactor Components: Probabilistic Modeling, System Identification and Data Fusion Based Big Data Analytics Approach

Subhasish Mohanty[1], Bryan Jagielo[2], William Iverson[3], Chi Bum Bhan[4], William Soppet[1], Saurin Majumdar[1], and Ken Natesan[1]

[1]Nuclear Engineering Division, Argonne National Laboratory

[2]2014 DOE-SULI summer intern at Argonne National Laboratory from Oakland University, Rochester

[3]2014 DOE-SULI summer intern at Argonne National Laboratory from University of Illinois, at Urbana-Champaign, Champaign

[4]Former Employee of Argonne National Laboratory, Currently at Pusan National University, South Korea

September 2014

This page intentionally left blank

ABSTRACT

Nuclear reactors in the United States account for roughly 20% of the nation's total electric energy generation, and maintaining their safety in regards to key component structural integrity is critical not only for long term use of such plants but also for the safety of personnel and the public living around the plant. Early detection of damage signature such as of stress corrosion cracking, thermal-mechanical loading related material degradation in safety-critical components is a necessary requirement for long-term and safe operation of nuclear power plant systems. At present, only preventative maintenance and in-service inspection through nondestructive evaluation (NDE) techniques are viable methods for damage detection and quantification. However, the current state of the art nondestructive evaluation (NDE) techniques used in nuclear reactor structural inspection are manual, labor intensive, time consuming, and only used when the reactor has been shut down. Despite periodic inspection of plant components, a failure mode such as stress corrosion and/or fatigue crack can initiate in between two scheduled inspections and can become critical before the next scheduled inspection. In this context, real time monitoring of nuclear reactor components is necessary for continuous and autonomous health monitoring and life prognosis of safety critical reactor components. However real time monitoring of structural components is a highly complex multidisciplinary area requiring intermixing of knowledge base in advanced structural mechanics (such as in fracture mechanics, material damage physics modeling) with knowledge base in big data analytics approaches (such as in data mining probabilistic modeling, system identification, data fusion, etc.).

In this report, first the basic background and futuristic scopes related to online structural health monitoring and prognostics are discussed. Then the basic concepts behind structural health monitoring and prognostic are demonstrated through two examples such as through a) the demonstration of various system identification and data fusion based approaches for online monitoring of stress corrosion cracking in a pressurized water reactor steam generator tube using active ultrasonic sensor networks b) then through the demonstration of a framework for real time estimation of probabilistic fatigue usages factor and remaining life of light water reactor steel based on real time strain measurements under different environmental and loading conditions. The report is organized into three major sections such as:

1. A Futuristic Online Structural Health Monitoring and Prognostics Framework for US Nuclear Reactors.

2. Linear and Nonlinear System Identification and Sensor Data Fusion Based Big Data Analytics Approach for Stress Corrosion Crack Monitoring in Nuclear Reactor Components Using Active Ultrasonic Sensor Networks.

3. Gaussian Process Based Probabilistic Framework for Online Fatigue Usage Factor Monitoring & Remaining Life Forecasting in Nuclear Reactor Components.

This page intentionally left blank

TABLE OF CONTENTS

ABSTRACT i

Table of Contents iii

List of Figures iv

Abbreviations viii

Acknowledgments ix

1 A Futuristic Online Structural Health Monitoring and Prognostics Framework for US Nuclear Reactors 10

1.1 Introduction 10

1.2 Online structural health monitoring 10

1.3 Online Structural Health Prognostics 12

2 Linear and Nonlinear System Identification and Sensor Data Fusion Based Big Data Analytics Approach for Stress Corrosion Crack Monitoring in Nuclear Reactor Components Using Active Ultrasonic Sensor Networks 13

2.1 Introduction 13

2.2 Experiments and OSHM System Design 13

2.2.1 Experimental Setup, Pulse Generation, and Data Acquisition 14

2.2.2 Fast Scale Signal Processing 16

2.2.3 Slow-Scale Damage Anomaly Estimation 20

2.2.4 Multi-Node Sensor Data Fusion 49

2.3 Conclusion 54

3 A Bayesian Statistic Based Probabilistic Framework for Online Fatigue Usage Factor Monitoring & Remaining Life Forecasting in Nuclear Reactor Components 55

3.1 Introduction 55

3.2 Theoretical Background 55

3.2.1 Online mean usage factor and remaining useful life prediction under in-air-fatigue loading 55

3.2.2 Probabilistic modeling of usage factor and remaining useful life 57

3.2.3 Online mean and probabilistic usage factor and remaining useful life prediction under light water reactor environment condition fatigue loading 59

3.3 Numerical Results 61

3.3.1 High purity water and elevated temperature live fatigue test 61

3.3.2 PWR water and elevated temperature live fatigue test 71

3.3.3 In-air and room temperature live fatigue test 74

3.3.4 Simulated random strain transients under PWR water condition 78

3.4 Conclusions 82

LIST OF FIGURES

Figure 1. 1 A fault tree diagram of a national level OSHM system. 11
Figure 1. 2 Schematic of already degraded states of structure estimated through an OSHM system and forecasted states and their probability bound through an OLP system... 12
Figure 2. 1 A schematic of the fast scale pulsing in reference to the slow scale process. 14
Figure 2. 2 A general schematic of the experimental setup and sensor configuration. 15
Figure 2. 3 a) Experimental setup of actual U-bend specimen with screw jack b) Magnified view showing the rectangular PZT actuator and sensor in group 1. 15
Figure 2. 4 Data acquisition and processing path of OSHM system. 16
Figure 2. 5 Sample signal from actuator, sensor group 1, sensor group 2, and noise sensor. . 17
Figure 2. 6 Sample spectrogram of signal from actuator, sensor group 1, sensor group 2, and noise sensor. 18
Figure 2. 7 Selected signal from original sample of signal from actuator, sensor group 1 19
Figure 2. 8 Example spectrogram of windowed and filtered signal from actuator, sensor group 1, sensor group 2, and noise sensor. 20
Figure 2. 9 Scatter plot of first, quarter life, half-life, three quarters life, and end of life complete signal from sensor group 1 and sensor group 2. 21
Figure 2. 10 Scatter plot of first, quarter life, half-life, three-quarters life, and end of life windowed and filtered signal from sensor group 1 and sensor group 2. 22
Figure 2. 11 Calculated means from sensor group 1 and sensor group 2 23
Figure 2. 12 Calculated variances from sensor group 1 and sensor group 2. 24
Figure 2. 13 Covariance between actuator and sensor group 1 and actuator and sensor group 2. 25
Figure 2. 14 Covariance between sensor group 1 and sensor group 2. 26
Figure 2. 15 Sample scatter plot of mapping between sensors in group 1 with regression line. 27
Figure 2. 16 Linear fit parameters for mapping between actuator and sensor group 1. 28
Figure 2. 17 Linear fit parameters for mapping between actuator and sensor group 2 29
Figure 2. 18 Linear fit parameters for mapping between sensors in group 1 and sensors in group 2. 30
Figure 2. 19 Plot of the damage index computed from linear mapping between sensors in group 1. 31
Figure 2. 20 Plot of the damage index computed from linear mapping between sensors in group 2. 31
Figure 2. 21 Predicted and actual output using CRA mapping between sensors in group 1... 33
Figure 2. 22 Prediction and actual output using CRA mapping between sensors in group 2.. 33
Figure 2. 23 Computed damage index from CRA mapping between sensors in group 1..... 34
Figure 2. 24 Computed damage index from CRA mapping between sensors in group 2..... 35
Figure 2. 25 Predicted and actual output using ETFE mapping between sensors in group 1.. 36

Figure 2. 26 Predicted and actual output using ETFE mapping between sensors in group 2.. 37
Figure 2. 27 Computed damage index from ETFE mapping between sensors in group 1. 38
Figure 2. 28 Computed damage index from ETFE mapping between sensors in group 2. 38
Figure 2. 29 Predicted output with two standard deviation error bounds and predicted and actual output from mapping between sensors in group 1. 41
Figure 2. 30 Magnified version of Figure 2.29. 42
Figure 2. 31 Predicted output with two standard deviation error bounds and predicted and actual output from mapping between sensors in group 2. 42
Figure 2. 32 Magnified version of Figure 2.31. 43
Figure 2. 33 Hyperparameters for Gaussian Process model computed between sensors in group 1. 44
Figure 2. 34 Hyperparameters for Gaussian Process model computed between sensors in group 2. 44
Figure 2. 35 $\ell 2$-norm of hyperparameters computed between sensors in group 1. 45
Figure 2. 36 $\ell 2$-norm of hyperparameters computed between sensors in group 2. 45
Figure 2. 37 Computed prediction error for Gaussian Process mapping between sensors in group 1. 46
Figure 2. 38 Computed prediction error for Gaussian Process mapping between sensors in group 2. 47
Figure 2. 39 Computed baseline referenced damage index for Gaussian Process mapping between sensors in group 1. 48
Figure 2. 40 Computed baseline referenced damage index for Gaussian Process mapping between sensors in group 2 48
Figure 2. 41 A diagram of the data path for PCA dimension reduction. 49
Figure 2. 42 All damage index time series from Gaussian Process mapping. 51
Figure 2. 43 Computed damage index using Gaussian Process mapping and PCA based sensor fusion. 51
Figure 2. 44 A picture of the U-bend pipe specimen after test. 52
Figure 2. 45 The damage index computed with Gaussian Process and PCA at quarter-life, half-life, three quarters life, and end of life. 53
Figure 2. 46 The damage index computed recursively at each damage level with the Gaussian Process and PCA and range in computed damage indices due to mathematical error. 53
Figure 3. 1 ANL environmental test frame with live fatigue monitoring system 62
Figure 3. 2 Intermittent cyclic stress history for the high purity water fatigue test 65
Figure 3. 3 Magnified stress history 66
Figure 3. 4 Intermittent transformed cyclic strain history for the high purity water fatigue test using stroke-strain mapping 66
Figure 3. 5 Time history of environmental correction factor $Fenk$ 67

Figure 3. 6 Stroke sensor measurement based real time estimated usages factor time history for the high purity water fatigue test using both NUREG-6909 based approach and GP based approach 67
Figure 3. 7 Load cell or stress sensor measurement based real time estimated usages factor time history for the high purity water fatigue test using both NUREG-6909 based approach and GP based approach 68
Figure 3. 8 Strain Amplitude vs Fatigue Life for stainless steel in PWR high temperature water 68
Figure 3. 9 Example histogram and probability density function of logarithmically scaled fatigue life approximately at 0.6 % strain amplitude for PWR data shown in Figure 3.8 69
Figure 3. 10 GP estimated logarithmically scaled mean cycle to failure and associated 2σ confidence bound as estimated at any given fatigue cycle 69
Figure 3. 11 Stroke sensor measurement based real time forecasted fatigue life for the high purity water fatigue test specimen at any given fatigue cycle 70
Figure 3. 12 Load cell sensor measurement based real time forecasted fatigue life for the high purity water fatigue test specimen at any given fatigue cycle 70
Figure 3. 13 Intermittent transformed cyclic strain history for the LWR water fatigue test using stroke-strain mapping 72
Figure 3. 14 Time history of environmental correction factor $Feni$ 72
Figure 3. 15 GP estimated logarithmically scaled mean cycle to failure and associated 2σ confidence bound as estimated at any given fatigue cycle 73
Figure 3. 16 Stroke sensor measurement based real time estimated usage factor time history for the PWR water fatigue test using both NUREG-6909 based approach and GP based approach 73
Figure 3. 17 Strain gage sensor measurement based real time forecasted fatigue life for the PWR water fatigue test specimen at any given fatigue cycle 74
Figure 3. 18 Cyclic strain history for the in air fatigue test 75
Figure 3. 19 Strain amplitude vs in-air test fatigue life for stainless steel 76
Figure 3. 20 Example histogram and probability density function of logarithmically scaled fatigue life approximately at 0.2% strain amplitude for in-air condition data shown in Figure 3.19 76
Figure 3. 21 Strain gage sensor measurement based real time forecasted fatigue life for the in air fatigue test specimen at any given fatigue cycle 77
Figure 3. 22 Strain gage measurement based real time estimated usage factor time history for the in air fatigue test using both NUREG-6909 based approach and GP based approach 77
Figure 3. 23 Strain gage sensor measurement based real time forecasted fatigue life for the in air fatigue test specimen at any given fatigue cycle 78
Figure 3. 24 Pseudorandom cyclic strain history 79
Figure 3. 25 Time history of environmental correction factor $Feni$ 80

Figure 3. 26 Predicted logarithmically transformed time history of fatigue life (mean, upper and lower bounds), as it would be estimated through GP in a realistic reactor condition 80
Figure 3. 27 Estimated usage factor time history for pseudorandom cycles using both NUREG-6909 based approach and GP based approach 81
Figure 3. 28 Forecasted time history of fatigue life for random cycles 81
Figure 3. 29 Magnified Figure 3.28 showing clear decreasing trend of cycles to failure 82

ABBREVIATIONS

ANL	Argonne National Laboratory
CF	Corrosion Fatigue
DOE	Department of Energy
FEM	Finite Element Method
LWR	Light Water Reactor
LWRS	Light Water Reactor Sustainability
RT	Room Temperature
ET	Elevated Temperature
SCC	Stress Corrosion Cracking
SS	Stainless Steel

ACKNOWLEDGMENTS

This research was partially supported through the U.S. Department of Energy - Light Water Reactor Sustainability program under the work package of environmental fatigue study and partially supported through U.S Nuclear Regulatory Commission sponsored steam generator tube integrity program. In addition, substantial part of the research was also conducted through two DOE SULI summer (2014) interns at ANL.

1 A Futuristic Online Structural Health Monitoring and Prognostics Framework for US Nuclear Reactors

1.1 Introduction

The longevity of safety critical components in the current line of operating nuclear reactors requires the implementation of regular in-service inspection (ISI) and repair strategies. The current approach for ISI is to perform nondestructive evaluation (NDE) on the components during routine refueling or unscheduled shutdowns of the plant. NDE must be performed manually or in a semi-automated way and in a regular interval. As a result, NDE is costly, time consuming, and puts personnel at risk for exposure to high doses of radiation. The goal of NDE is to inspect all components to ensure safe operation during the length of the next usage cycle. However, usage cycle may have a duration at which the previous NDE is an inappropriate benchmark for the current health of the structure and failures may occur between inspections. Consequently, on-line structural health monitoring (OSHM) and on-line prognostics (OLP) are necessary to ensure that the components remain safe for operation during the entirety of the usage cycle [1-5]. Below, a futuristic OSHM and OLP framework is discussed briefly.

1.2 Online structural health monitoring

Unlike NDE's periodic manual and/or semi-automated interrogation of structural integrity, OSHM automatically and continuously interrogates structural health using an array of sensors permanently bonded to components. These sensors collect information about how components respond to the chosen interrogation method. The information can be processed and used to determine characteristics about the system. Under the basis of big data analytics approaches such as system identification, advanced signal processing, and data mining, the signals recorded by the sensors can be used to determine the changing transfer function of components. This transfer function can be monitored over time to determine the deviation of the components from the baseline measurements due to damage growth. The information can be used for early detection of cracks and relayed to an online prognostics algorithm for further analysis such as for predicting the remaining life of component based on condition estimated through OSHM system at any given instant of time.

OSHM system can be scaled up from monitoring of small regions of a component to a national level monitoring center for monitoring all the structural components of the plants from a centralized location (say for example from US Nuclear Regulatory Commission head quarter at Washington DC) . Figure 1.1 depicts the schematic of a scaled up system. Each plant can be divided into subsystems containing components with individual sensor nodes. The sensor nodes can connect to a subsystem network via wired or wireless connection [1-5]. The subsystem network will relay all of the information from all the nodes to the plant control center. Plant managers can be presented with real-time continuous updates regarding the overall plant structural integrity (SI) and can easily diagnose problems quickly down to the smallest component. Additionally, the health information for each plant can be transmitted to a regional control center and national control center for further monitoring and regulation. The national monitoring system would allow in depth aging and health analysis of the nation's fleet of nuclear plants efficiently and in real time. This research focuses on a component level real time monitoring framework.

Scaling up the OSHM system is beyond the scope of this investigation but can be a goal of future work.
up the OSHM system is beyond the scope of this investigation but can be a goal of future work.

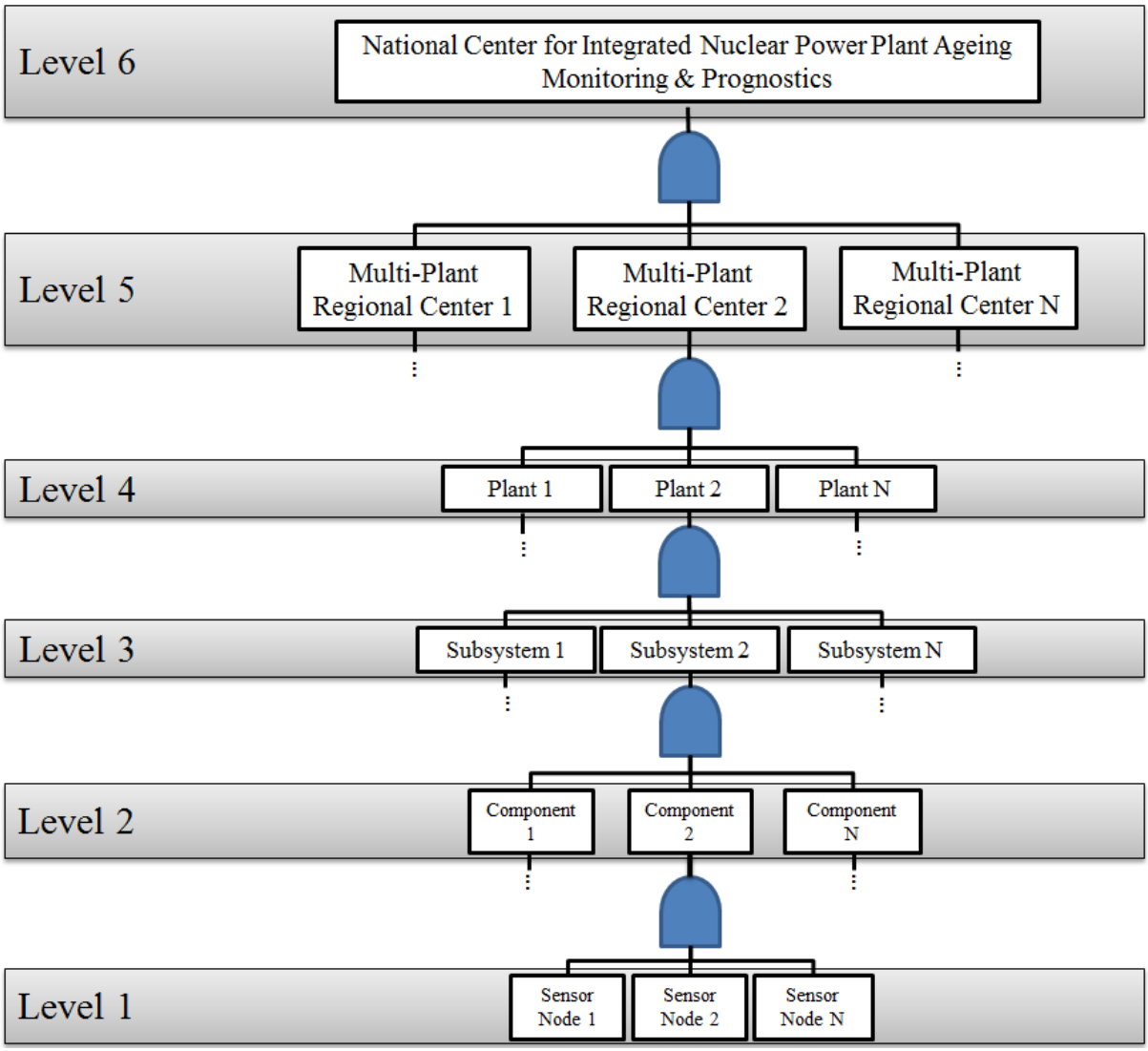

Figure 1. 1 A fault tree diagram of a national level OSHM system.

1.3 Online Structural Health Prognostics

In addition to online monitoring, online prognostics (OLP) can be used to help forecasting the remaining life of structural components. Currently, no such system available rather the retirement of the components are decided based on the offline NDE inspection data and/or based on the offline stress/strain versus life curves. However, there are many restrictions on the accuracy of the current approach since the stress/strain versus life curves might not always reflect the actual material microstructure, environment and loading condition the component in question subjected to. In contrary an OLP system associated with an OSHM system can incorporate real time material condition (e.g. through material dependent stress-strain hardening/softening), environment (e.g. light water reactor water chemistry, temperature, etc.) and loading condition (e.g. strain/load amplitude and rate, loading sequence, etc.). This will not only help to forecast the structural state and remaining useful life (RUL) in real time, but also will help to provide more accurate results. Figure 1.2 depicts the schematic showing the forecasted structural states with respect to the OSHM system estimated state information at any given instant of time.

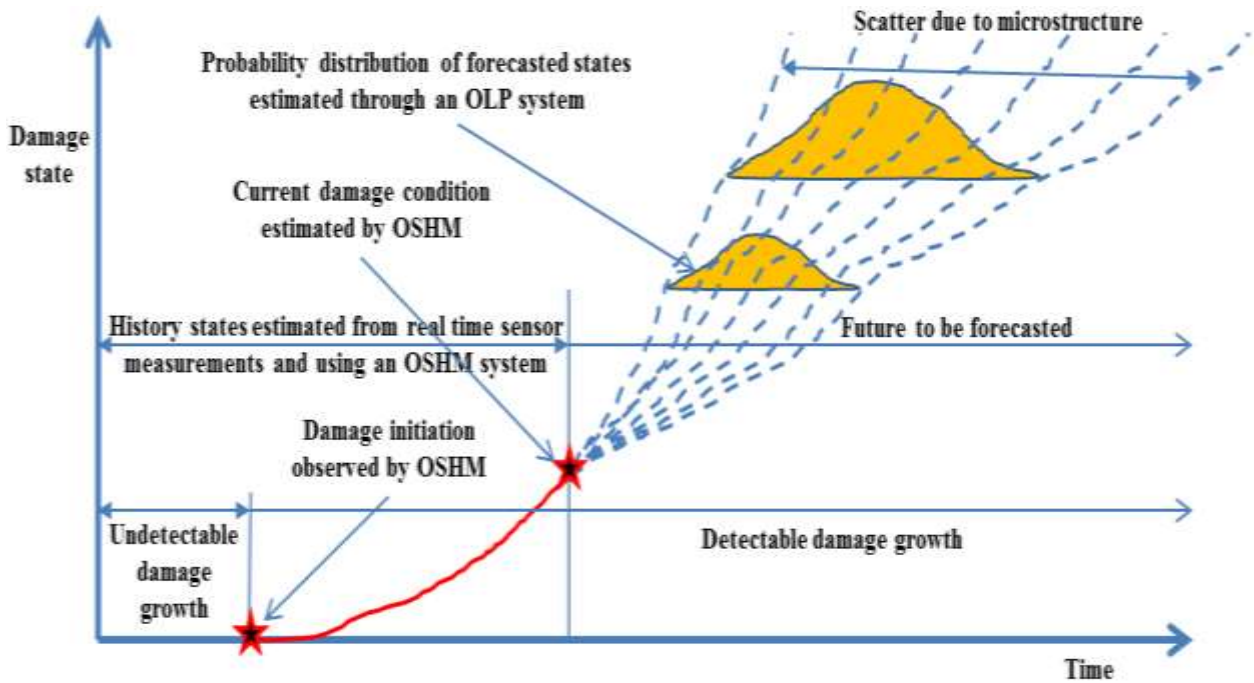

Figure 1. 2 Schematic of already degraded states of structure estimated through an OSHM system and forecasted states and their probability bound through an OLP system [1, 4].

In this report, first an ultrasound based approach is discussed, that can be used for online monitoring of stress corrosion cracking, and then a strain measurement based online fatigue usages factor monitoring and online remaining life forecasting approaches are discussed, through multiple example cases.

2 Linear and Nonlinear System Identification and Sensor Data Fusion Based Big Data Analytics Approach for Stress Corrosion Crack Monitoring in Nuclear Reactor Components Using Active Ultrasonic Sensor Networks

(Subhasish Mohanty, Bryan Jagielo, Chi Bum Bhan, Saurin Majumdar, Ken Natesan)

2.1 Introduction

The current state of the art nondestructive evaluation (NDE) techniques used in nuclear reactor structural inspection are manual labor intensive, time consuming, and only used when the reactor has been shut down. Also, despite periodic inspection of plant components, a failure mode such as stress corrosion crack can initiate in between two scheduled inspections and can become critical before the next scheduled inspection. In this context, real time monitoring of nuclear reactor components is necessary for continuous and autonomous monitoring of component structural health. In this research, an active ultrasonic based on-line monitoring (OSHM) framework is developed which can be used for real-time monitoring of degradation (e.g stress corrosion cracking) of nuclear power plant systems, and components. Different system identification based methods are investigated to estimate the structural degradation in real-time. Active broadband ultrasound input is used for damage interrogation and a multi-sensor data fusion technique is implemented to improve accuracy in state estimation. The damage index at any particular time is computed using linear techniques such as linear regression, correlation analysis, and empirical transfer function estimation and nonlinear techniques such as Gaussian Process probabilistic modeling. The success of each method is discussed and the necessity of sensor fusion is evaluated. The framework was demonstrated through the monitoring of anomaly trend in a nuclear reactor steam generator tube undergoing stress corrosion cracking (SCC) testing at ANL's Steam Generator Tube Integrity Facilities. The various steps involved are briefly discussed below.

2.2 Experiments and OSHM System Design

The on-line monitoring system estimates the current state of the structure through two components, the fast scale ultrasonic signal acquisition system and signal processor and the slow scale structural anomaly (e.g. in this case SCC) state estimator. In the fast scale process the host structure was excited with high frequency ultrasound waves using a piezoelectric actuator and the respective fast scale sensor signals were collected and processed. This process was intermittently conducted to capture the entire structural degradation process. To note that compared to fast scale ultrasound pulsing the structural degradation process is a slower process and occurs over a very long duration of time. Also note that unlike the low frequency based vibrations/temperature/strain sensor signals, which are typically, acquired continuously, the high frequency ultrasound signal cannot be acquired continuously due to large computer memory and processing time requirements. The intermittently collected fast scale ultrasound signal were processed first then transferred to a second stage signal processor that estimates the state of the structure to capture the slow scale damage progression in a structure. To note that in the discussed accelerated laboratory test case the damage process occurred over multiple hours, however in the real nuclear reactor components the damage process occurs over years. Hence, two distinct signal processing

stages/procedures to be followed for ultrasonic based structural damage or anomaly trend estimation. Figure 2.1 shows a schematic demonstrating the difference between the fast scale ultrasound pulsing and the slow scale structural anomaly trend. The details of the experiment setup, fast scale signal processing, and slow scale state estimation are discussed further in the following subsections.

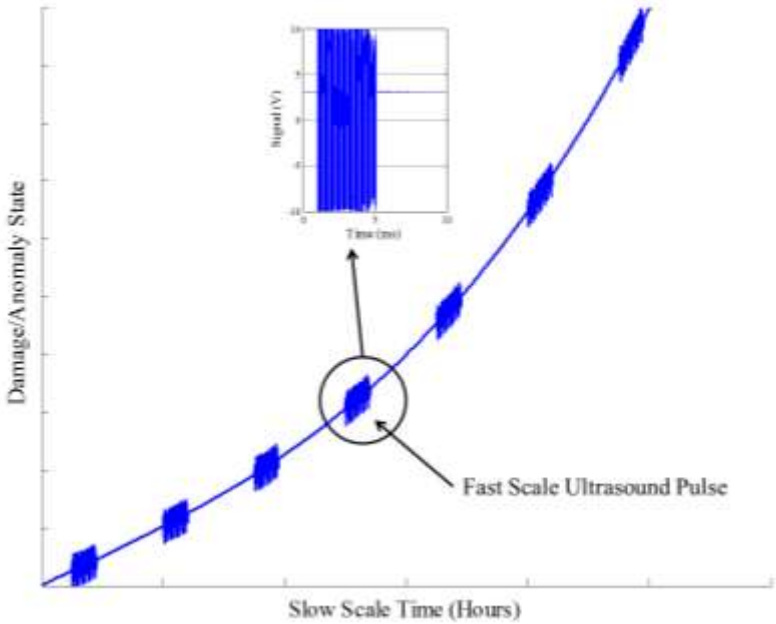

Figure 2. 1 A schematic of the fast scale pulsing in reference to the slow scale process.

2.2.1 Experimental Setup, Pulse Generation, and Data Acquisition

The test setup is a US-NRC sponsored test facility [6] to perform structural integrity test of steam generator tubes for evaluating SCC under simulated laboratory conditions. While performing usual NRC regulated tube integrity test, additional instrumentation was made for online monitoring of SCC using permanently bonded active ultrasonic actuator and sensor nodes. The aim of this exercise was to demonstrate the basic SHM capability on nuclear reactor component and the overall system can be scaled up for component, subsystem, plant level, and multi-plant level application as shown in Figure 1.1. SCC testing was performed on a U-bend pipe specimen. The test setup diagram is illustrated in Figure 2.2 and the actual test setup is displayed in Figure 2.3a. The testing apparatus consisted of a U-bend section of pipe and a screw jack placed around each end of the specimen. The screw jack was used to simulate stress on the U-bend by displacing the legs toward the centerline. Sodium Tetrathionate solution was placed at the apex of the U-bend to accelerate corrosion and cracking within the specimen. Piezoelectric crystals were permanently bonded to the pipe in two groups near the ends of the U-bend. Sensor group 1 contained one piezoelectric actuator and two piezoelectric sensors and sensor group 2 contained two piezoelectric sensors. The rectangular type piezoelectric actuator and sensor arrangement of sensor group 1 is displayed in Figure 2.3b. Additionally, a disk type piezoelectric sensor was placed in the open air to measure external acoustic and electromagnetic noise. A National Instruments PXI data

acquisition system was used to excite the piezoelectric actuator and to collect corresponding ultrasonic data from each of the piezoelectric sensors.

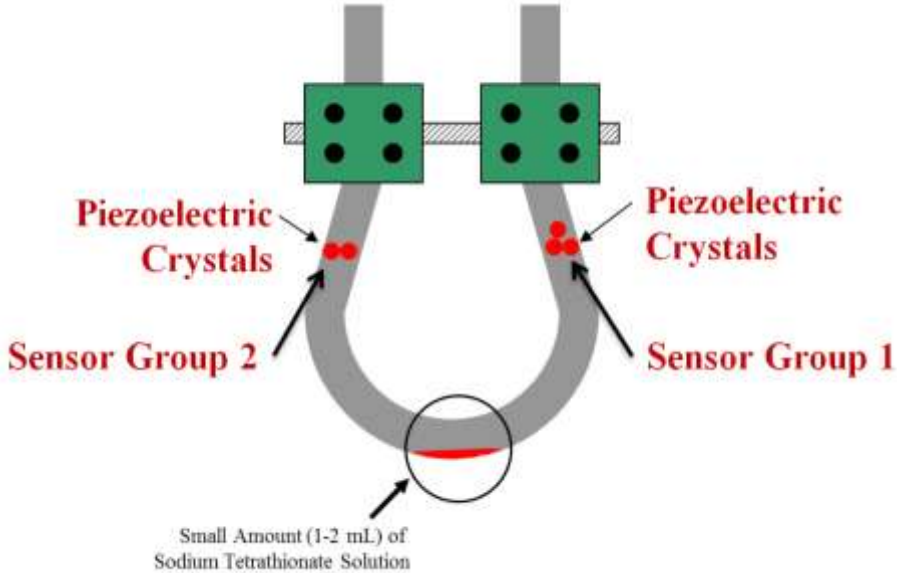

Figure 2. 2 A general schematic of the experimental setup and sensor configuration.

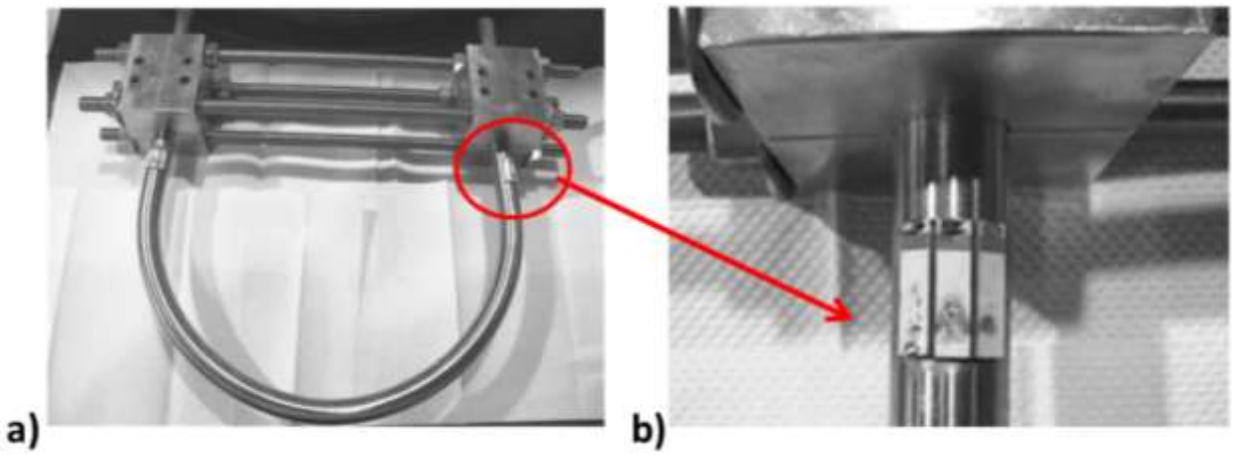

Figure 2. 3 a) Experimental setup of actual U-bend specimen with screw jack b) Magnified view showing the rectangular PZT actuator and sensor in group 1.

In the active ultrasonic system interrogation, data collection occurred in several steps. The data path for data collection is illustrated in Figure 2.4. Every 30 minutes, the piezoelectric actuator emitted a chirp signal, sweeping frequencies from 50 kHz to 350 kHz. The piezoelectric sensors placed on both ends of the U-bend received the resulting signal both direct and reflected signals from different locations across the structure. The sensor signals were processed by a high pass, passive filter to eliminate low frequency noise before being received by the data acquisition system. The filtered signal was captured by a NI PXI data acquisition system and stored in data files. Lastly, data files were processed by a MATLAB

signal processing and state estimation algorithm. The design of the MATLAB signal processor and state estimator will be discussed further in the upcoming sections.

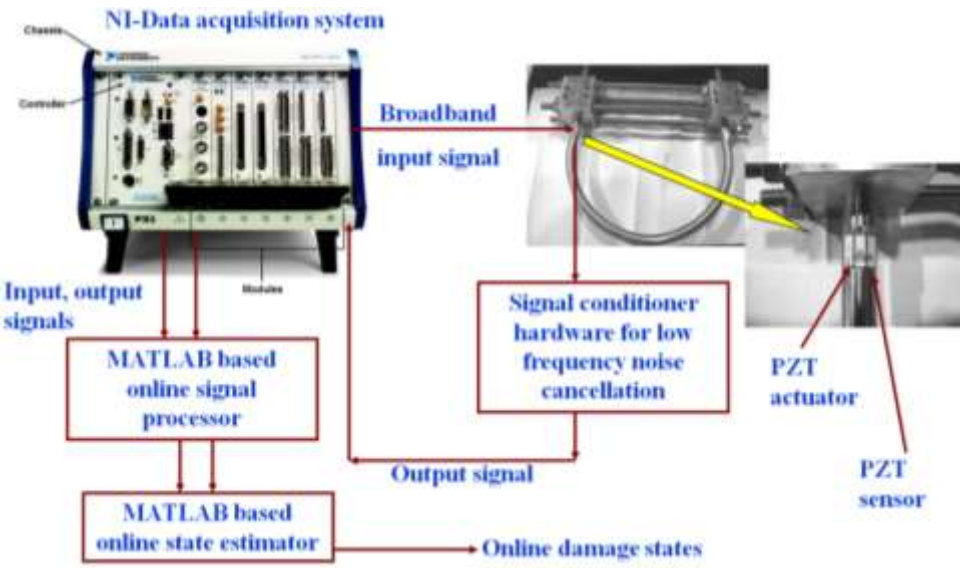

Figure 2. 4 Data acquisition and processing path of OSHM system.

The fast scale signals were collected in real time using National Instruments (NI) based PXI data acquisition system (as shown in Figure 2.4) and LABVIEW based data acquisition software. Once the sensor data was acquired at a given instant of time, the slow scale anomaly estimator processed these signal and estimate the state of the structure at that given instant. A MATLAB based signal processor and state estimator was developed to work along with LABVIEW for real time monitoring.

2.2.2 Fast Scale Signal Processing

Before the state of the structure can be accurately estimated, the fast scale process signals must be processed to ensure that they contain the valuable information. The fast scale signal processor designed incorporates two components: the window selector and frequency filter. The window selector chooses a portion of the signals containing the least noise for further analysis while attenuates any residual noise within the windowed signal. The window selector and filter parameters were determined after close study of the characteristics of the signals. The fast scale process signal is composed of six signals: the actuator's input on channel one, the near sensor pair's output on channels two and three (refer sensor group 1 Figure 2.2), the far sensor pair's output on channels four and five (refer sensor group 2), and an external noise sensor not attached to the structure on channel six. The actuator inputs into the test structure a broadband chirp signal ranging from 50 kHz to 350 kHz through a PXI pulse generator card. Simultaneously, all 4 sensor signals (Ch. 2, 3, 4, and 5), noise (Ch. 6), and actuator signal (Ch.1) were acquired through a PXI ADC input card. Figure 2.5 shows sample signals from each of the channels during a single chirp pulse on the actuator. The broadband signals have a length of 10ms and were received at a frequency of 2 MHz, whereas, the broadband input signal was transmitted by the PXI pulse generator at a frequency of 1 MHz.

Displayed in Figure 2.5, the signals created by the actuator and observed by the sensors demonstrate various characteristics. The actuator signals in channel 1 has an initial offset voltage of +3.1V while all other channels have an offset of 0V. The initial offset voltage in the actuator channel could be due to residual charge build up due to the capacitive self-sensing nature of the piezoelectric actuator that receives reflected signals from the structure. The signals were observed to decrease in magnitude as the distance between the sensor and the actuator increased. The actuator signal, observed in channel 1, had a peak amplitude of 10V. In contrast, sensor group 1's signals have a peak amplitude 1.3V in channel 2 and 3.7V in channel 3 while sensor group 2's signals had a peak amplitude of 0.3V in channel 4 and 0.3V in channel 5. The external noise signal, displayed in channel 6, had a peak amplitude of 0.23V. The differences in the amplitudes of the signals were due to losses or attenuation within the structure of the pipe and bonding of the sensors. The acoustic and electromagnetic noise (Ch. 6) contained similar a peak amplitude when compared to sensor group 2's signals during the actuator's chirp cycle. However, the noise (Ch. 6) considerably decreased immediately after the actuator's chirp cycle had completed, offering a window of significantly less noise.

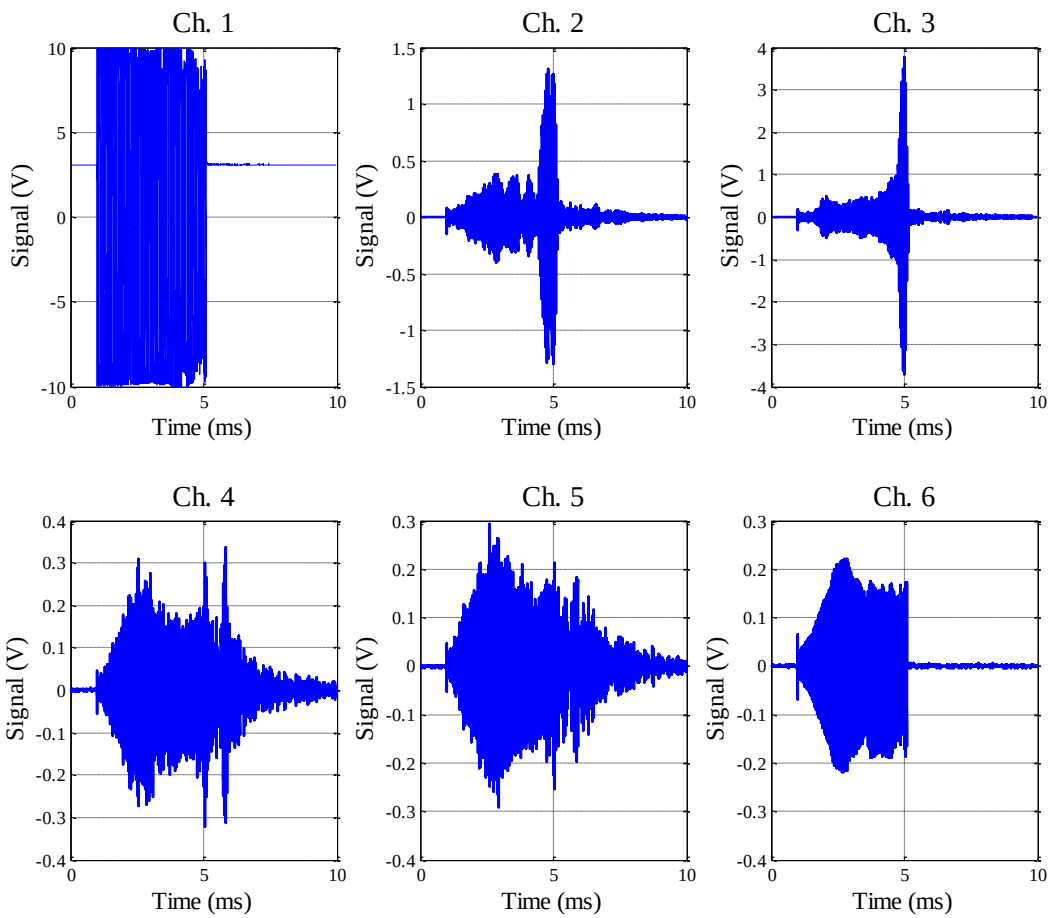

Figure 2. 5 Sample signal from actuator (top left), sensor group 1 (top center and top right), sensor group 2 (bottom left and bottom center), and noise sensor (bottom right).

The time-frequency plot of signals also offers significant insight into the acoustic and electromagnetic noise within the signals. The spectrogram in Figure 2.6 demonstrates further that the signal has a

significant component of high frequency noise during the chirp cycle due to equipment related electromagnetic interference. The high frequency noise can be observed across all channels from 1-5ms. Also, in Figure 2.6, the time frequency behavior of the noise channel (refer Ch. 6) was similar to the other channels from 1-5ms despite not being bonded to the structure. The noise dramatically decreases after pulsing has completed at 5ms. Some residuals from the external noise with frequency exceeding the maximum frequency of input signal (3.e. 350 kHz) still remain prominent within all signals after the chirp cycle.

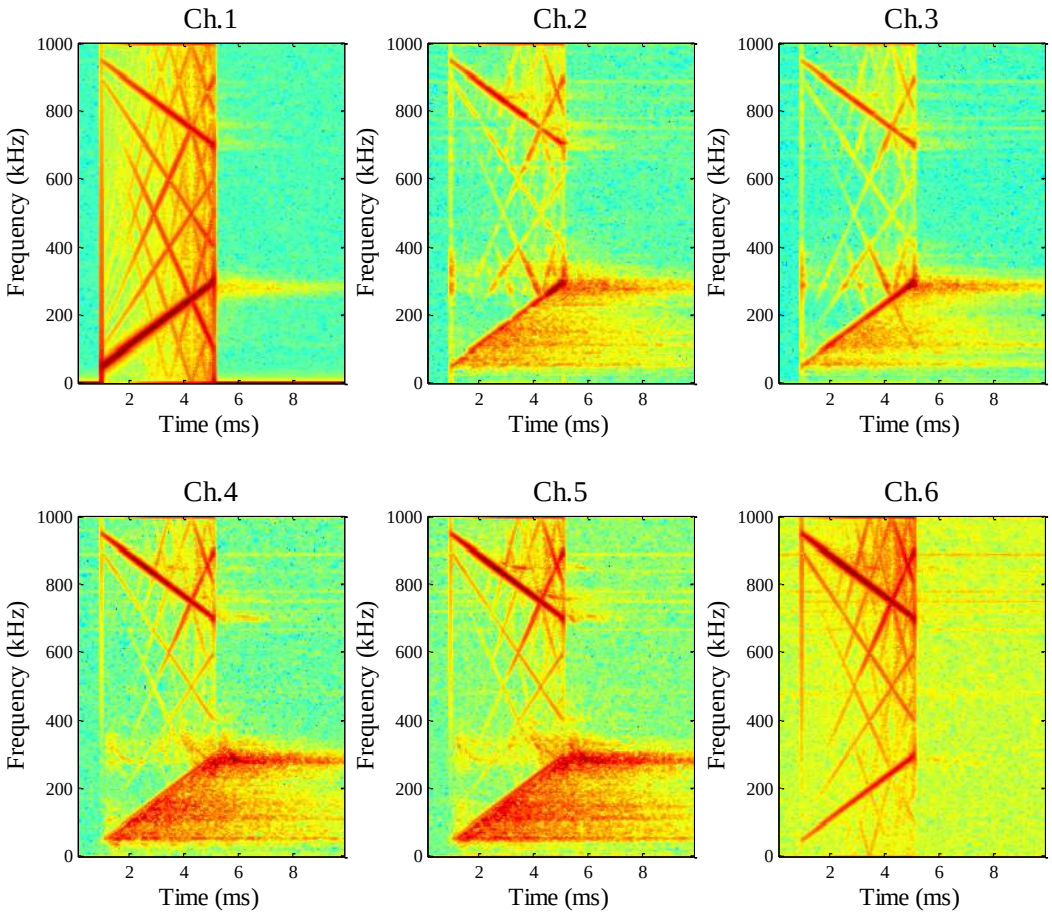

Figure 2. 6 Sample spectrogram of signal from actuator (top left), sensor group 1 (top center and top right), sensor group 2 (bottom left and bottom center), and noise sensor (bottom right).

2.2.2.1 Window Selection

Since the region immediately after the chirp input cycle was shown to have significantly less noise, it was selected as the window for analysis. In order to isolate this section of the signal, the actuator signal from channel 1 and a threshold based algorithm were used. Since all signals were recorded simultaneously, only the actuator signal is needed for the windowing procedure. First, the actuator signal was normalized by using the following expression:

$$z_i = \left|\frac{x_i - \mu}{\sigma}\right| \tag{2.1}$$

where x_i is the nth data point from channel 1, σ is the standard deviation of the signal, and μ is the offset obtained by averaging the first ten data points of the signal. Using the normalized signal, a search was performed from the end to beginning of the normalized signal according to the pseudocode in equation (2.2).

$$\begin{aligned} &for\ i = end\ to\ 1 \\ &\quad if\ z_i > z_{max} \cdot \eta \\ &\qquad exit\ loop \\ &end \end{aligned} \tag{2.2}$$

where η is threshold constant between 0 and 1. In this instance, η has a value of 0.02.Upon exiting the loop, the data window of interest begins with data point x_{i+1}. Figure 2.7 depicts the entire signal of each channel with the selected window plotted in red for a single chirp cycle.

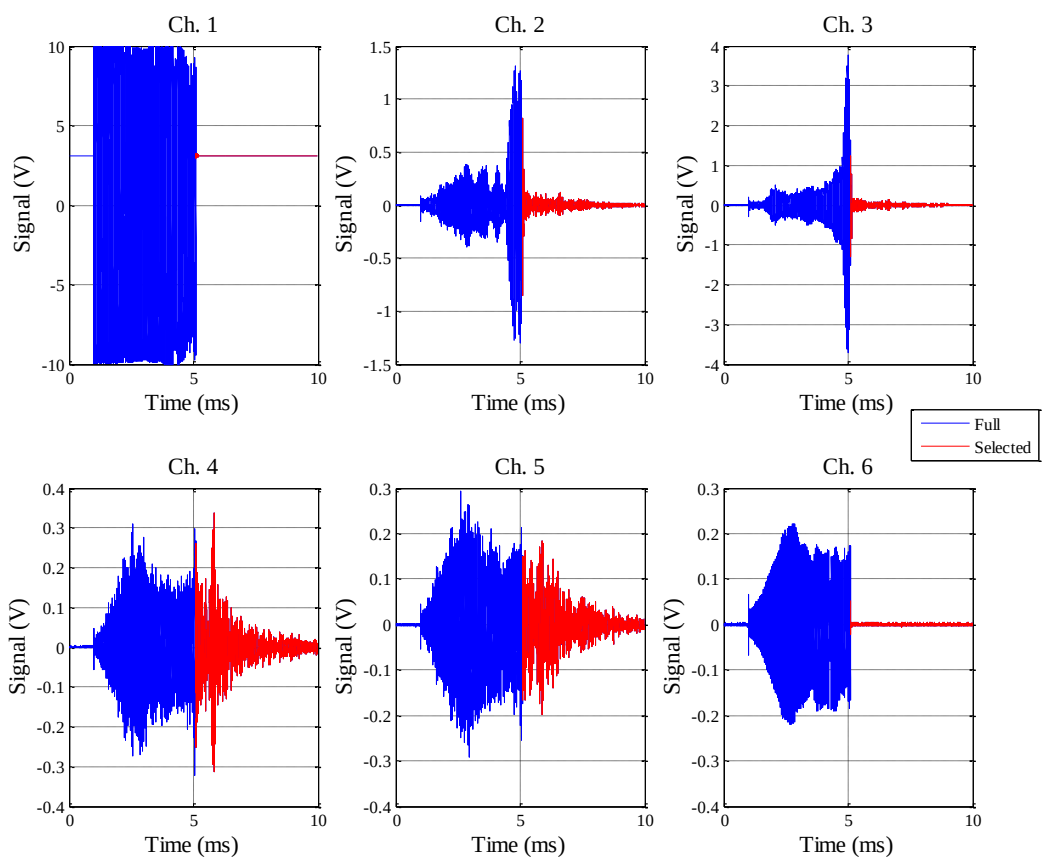

Figure 2. 7 Selected signal (red) from original sample of signal from actuator (top left), sensor group 1 (top center and right), sensor group 2 (bottom left and bottom center), and noise sensor (bottom right).

2.2.2.2 Digital filter implementation

To further isolate the residuals of the chirp signal from internal and external sources of interference, a band pass filter is used with corner frequencies 50 kHz and 350 kHz. By implementing a finite impulse response type (FIR) Butterworth filter in MATLAB on the windowed data from all channels, the residuals of the electromagnetic interference noise has been attenuated. Figure 2.8 shows the example of time-frequency response of windowed and filtered signal.

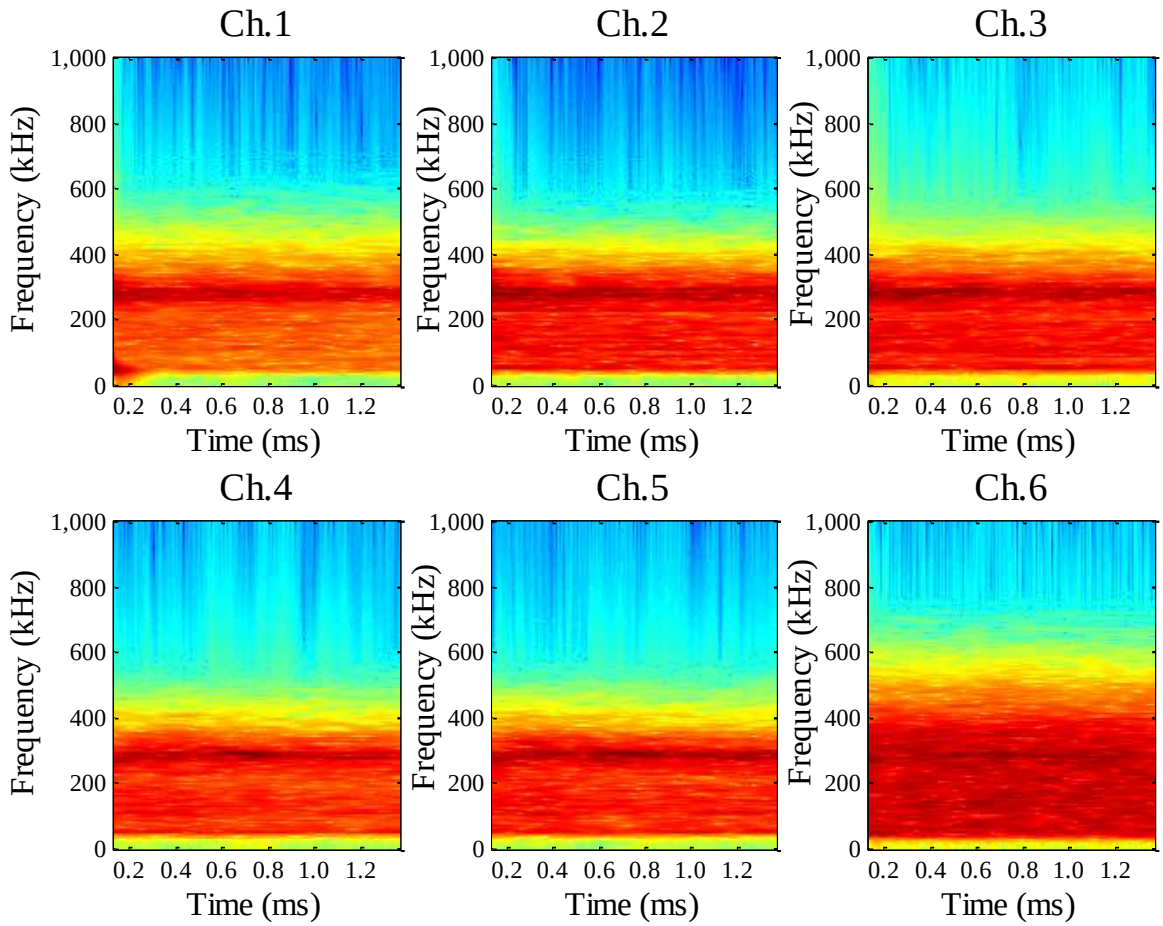

Figure 2. 8 Example spectrogram of windowed and filtered signal from actuator (top left), sensor group 1 (top center and right), sensor group 2 (bottom left and bottom center), and noise sensor (bottom right).

2.2.3 Slow-Scale Damage Anomaly Estimation

Using the fast scale signal discussed earlier, the slow scale damage growth were estimated using various linear and nonlinear system identification methods. This is essentially by mapping the transfer function (input-output relation) between different fast scale sensor channels and then tracking the change in transfer function over a longer slow scale period. These are discussed in detail in this section. As seen in Figure 2.5, the fast scale process of the actuator's pulsing and data acquisition only takes fractions of a

second to complete. In comparison, the slow scale predictor considers multiple data points separated by time increments of 30 minutes. Consequently, the transfer function mapped between the input and output signal during the fast scale process is assumed to be time invariant. However, during the slow scale the estimated transfer function will not remain fixed and is expected to be time variant as the system degrades structurally. As a result, the anomaly in the transfer function over the slow scale time axis can be modeled and can be used to estimate the anomaly of the structure. General statistics and linear system identification methods including correlation analysis, empirical transfer function estimation [7], and Gaussian Process probabilistic modeling [8] are discussed in detail; These are used individually for slow scale damage/anomaly trend time-series estimation.

2.2.3.1 Basic Scatter Plot Based Anomaly Analysis

The full signal and the filtered post-chirp data were compared over the life of the test structure. Figure 2.9 and Figure 2.10 display the scatter plots of both the full signal and the filtered windowed signal, respectively. Each plot displays the data from the structure's initial cycle and consecutive quarter lives.

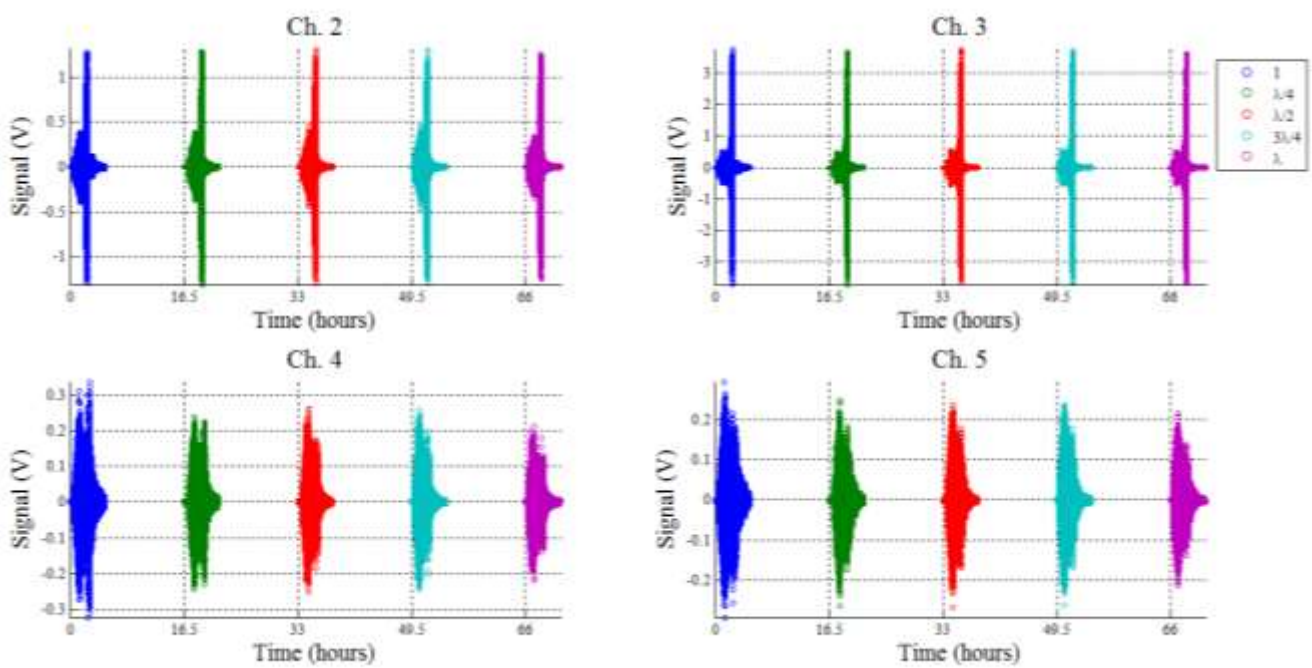

Figure 2. 9 Scatter plot of first, quarter life, half-life, three quarters life, and end of life complete signal from sensor group 1 (top left and top right) and sensor group 2 (bottom left and bottom right).

Only channels 4 and 5 in Figure 2.10 displayed an anomaly that the extremes of the signal were being attenuated over the slow scale. However, this trend is not clear and could be due to a blind zone discussed later. Also, sensors located away from the actuator (as in case of group 2 sensors refer Figure 2.2) are not always preferable due to requirement of more wiring and possibility of blind zone. If sensors are placed away from the ultrasonic actuator a blind zone can be formed due to a crack between the actuator and sensor. The blind zone may not allow the actuator signal to reach the sensor. If the sensor

does not receive the signals it may not help to predict the correct anomaly even though the damage actually continued growing. This can be seen from channels 4 and 5 data shown in Figure 2.10 that after 33 hours the signal amplitude remained constant after dropping significantly. Since inspection of the scatter plots did not yield a substantial slow scale anomaly, more intensive methods of analysis were necessary.

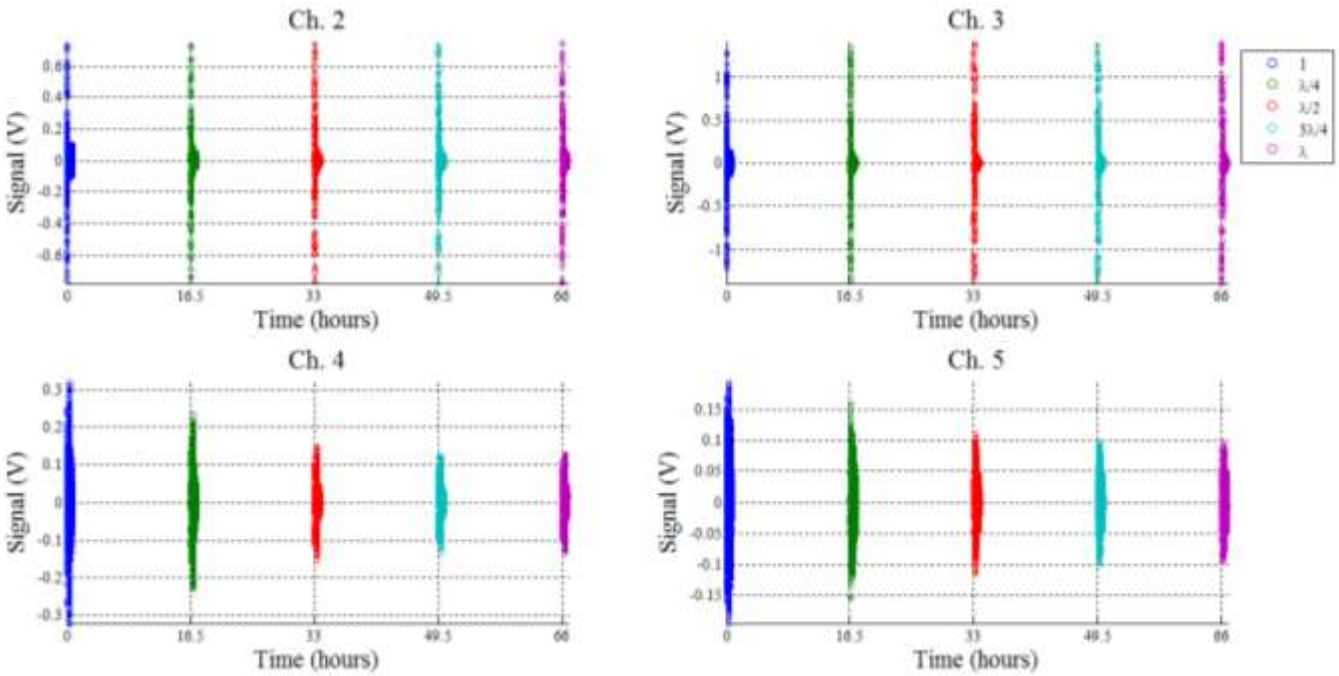

Figure 2. 10 Scatter plot of first, quarter life, half-life, three-quarters life, and end of life windowed and filtered signal from sensor group 1 (top left and top right) and sensor group 2 (bottom left and right).

2.2.3.2 Single Channel Mean and Variance Based Anomaly Prediction

The means and variances of the sensor data were computed for each sample at every chirp cycle. Figure 2.11 and Figure 2.12 displays the plots of the means and variances, respectively, over the slow scale time axis. From Figure 2.11, it can be seen that the mean of sensor signals from different channels do not show any clear trend. Whereas from Figure 2.12 it can be seen that for channels 3, 4, and 5, the variance shows an anomaly trend up to some extent as the structure degrades. However, the channel 2 variance does not demonstrate such a relationship. In channels 4 and 5, the variance appears to change very little after 35 hours which could be due to a possible blind zone developing due to through cracking of steam generator pipe. A growing SCC crack through the surface of a structure would inhibit the signal from being passed from the actuator to sensors of sensor group 2 (refer Figure 2.2). The attenuated signal would decrease the overall variance in the signal and would not carry a complete picture of the overall anomaly. Overall, the first order statistics fail to completely capture the desired relationship between time and the structure's degradation.

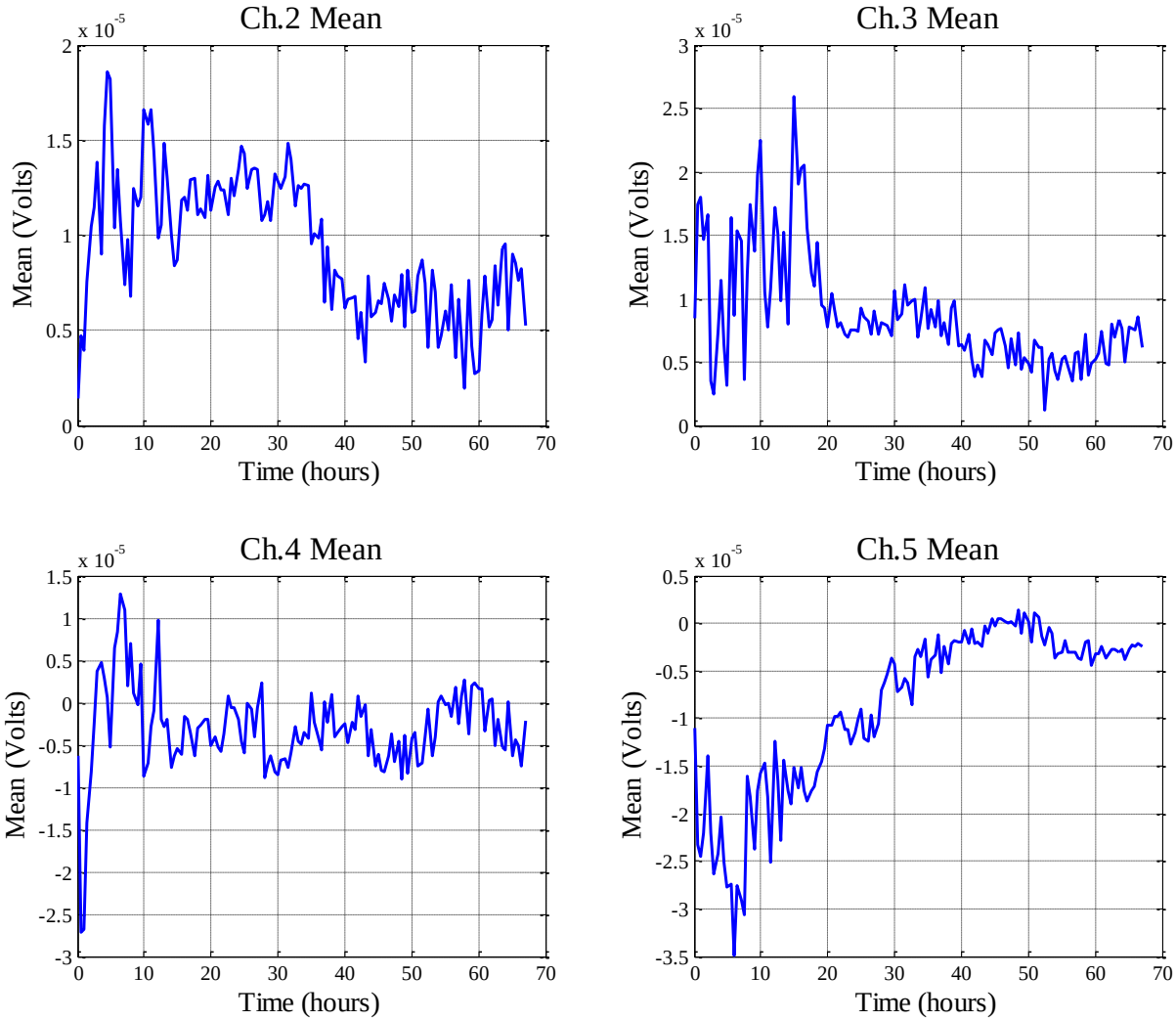

Figure 2. 11 Calculated means from sensor group 1 (top right and top left) and sensor group 2 (bottom right and bottom left).

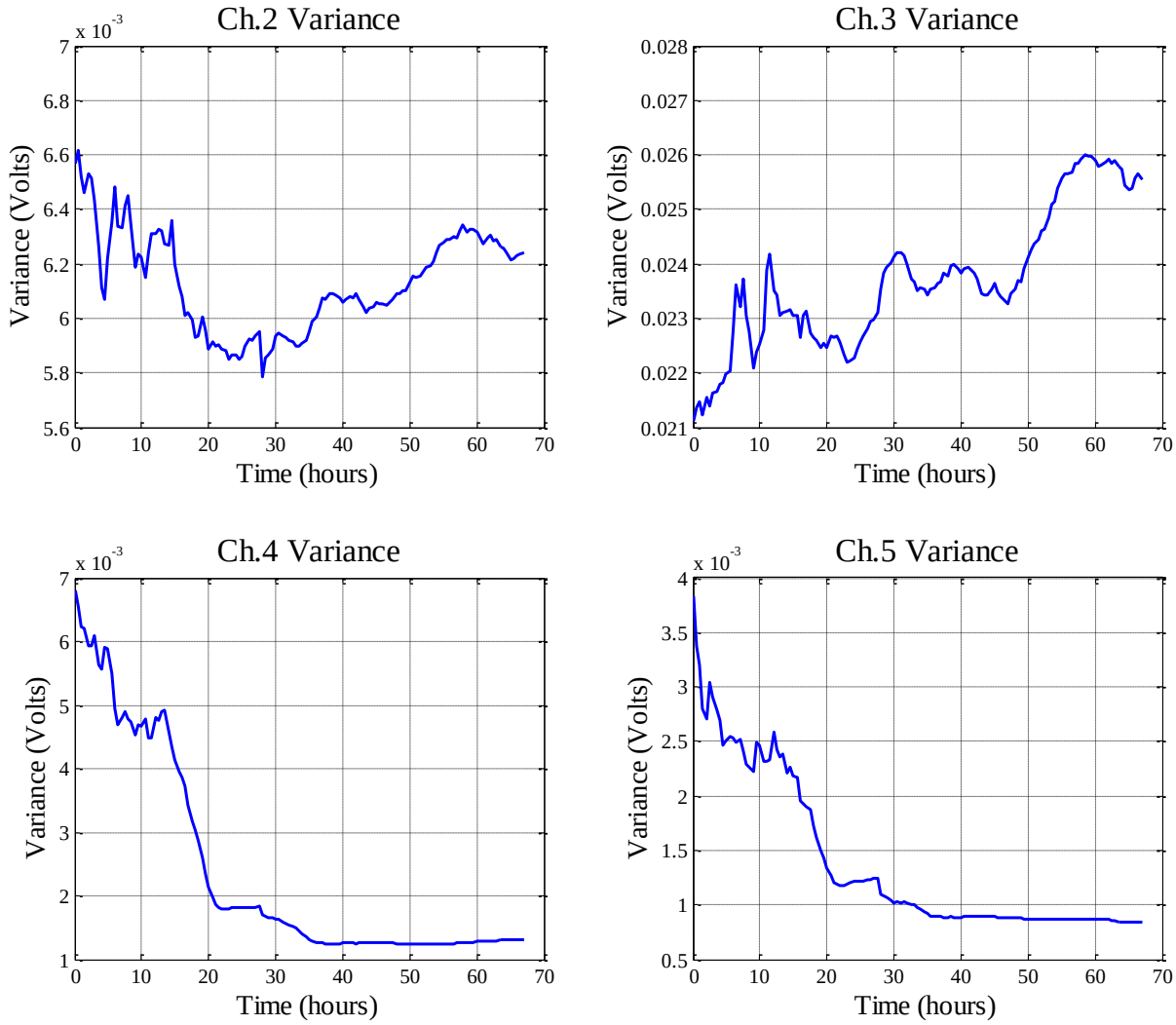

Figure 2. 12 Calculated variances from sensor group 1 (top right and top left) and sensor group 2 (bottom right and bottom left).

2.2.3.3 Multi-Channel Covariance Base Damage Estimation

Since first order analysis using single sensor data failed to demonstrate a substantial consistent anomaly trend prediction from each and every sensor channel, more intensive methods were necessary. Contrary to mean and variance based single channel data analysis, the covariance was computed for each chirp cycle between channels. The covariance for each cycle was plotted against the slow scale time axis and examined for long term anomalies, illustrated in Figure 2.13 and Figure 2.14. From Figure 2.13, it can be seen that, whenever a sensor channel measurement (from Ch. 2, 3, 4, and 5) was correlated with the actuator channel data (Ch. 1), the covariance based anomaly time-series does not show any noteworthy anomaly. The actuator channel may not capture more frequency content in the selected time-frequency window although the actuator piezoelectric placed near to the sensor piezoelectric (Ch. 2 and 3) should work ideally as a receiver after the pulsing is completed. The time-frequency plot shown in Figure 2.6 and Figure 2.8 supports this claim. Comparing channel 1 and 2's time frequency plot, frequencies

between 50 kHz and 350 kHz are significantly less prominent post-pulse in channel 1 than channel 2. However, the covariance between sensor channels (2, 3, 4, and 5) shows some anomaly as shown in Figure 2.14. On the other hand, it can be noticed from Figure 2.14 that if either or both of channel 4 and 5 are used the anomaly history does not show any clear trend other than the covariance between channel 2 and 4 and that is again up to first 30-35 hours. In addition, using these channels, it is observed that there is not much change in anomaly trend after 30-35 hours, which could be due to the development of a blind zone.

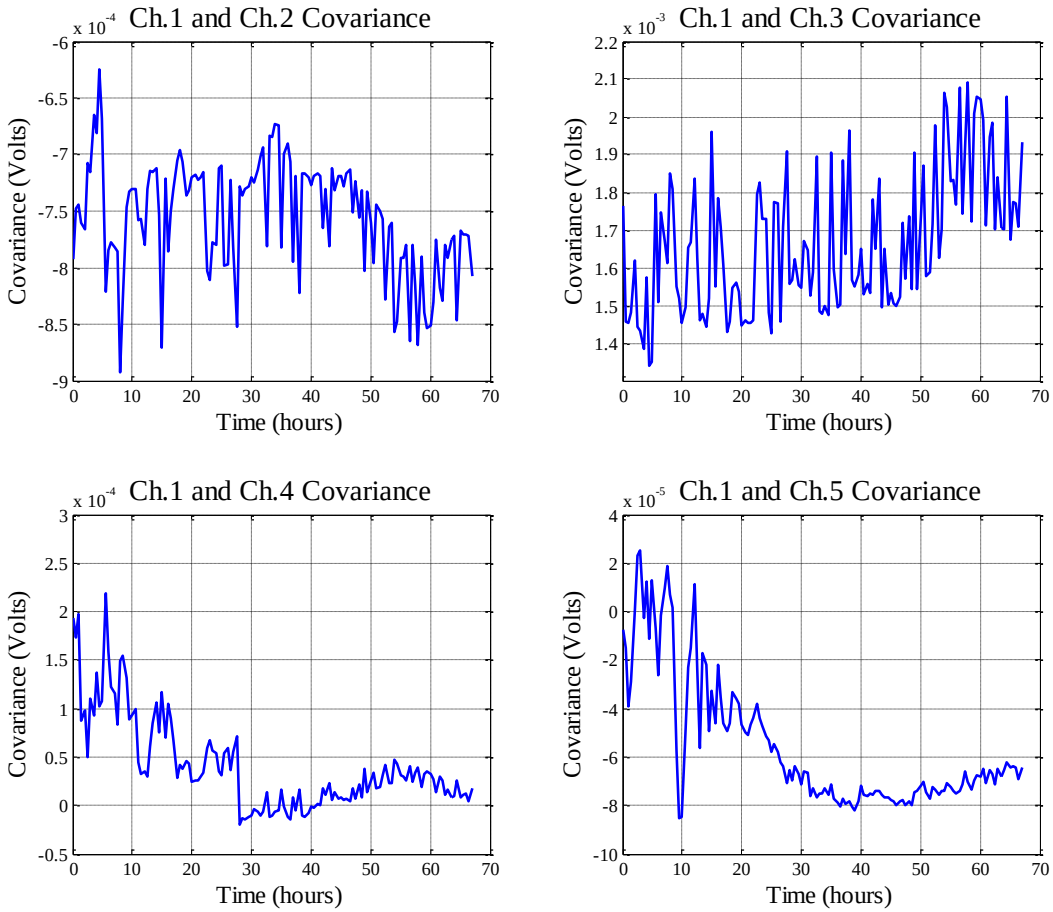

Figure 2. 13 Covariance between actuator and sensor group 1 (top right and top left) and actuator and sensor group 2 (bottom right and bottom left).

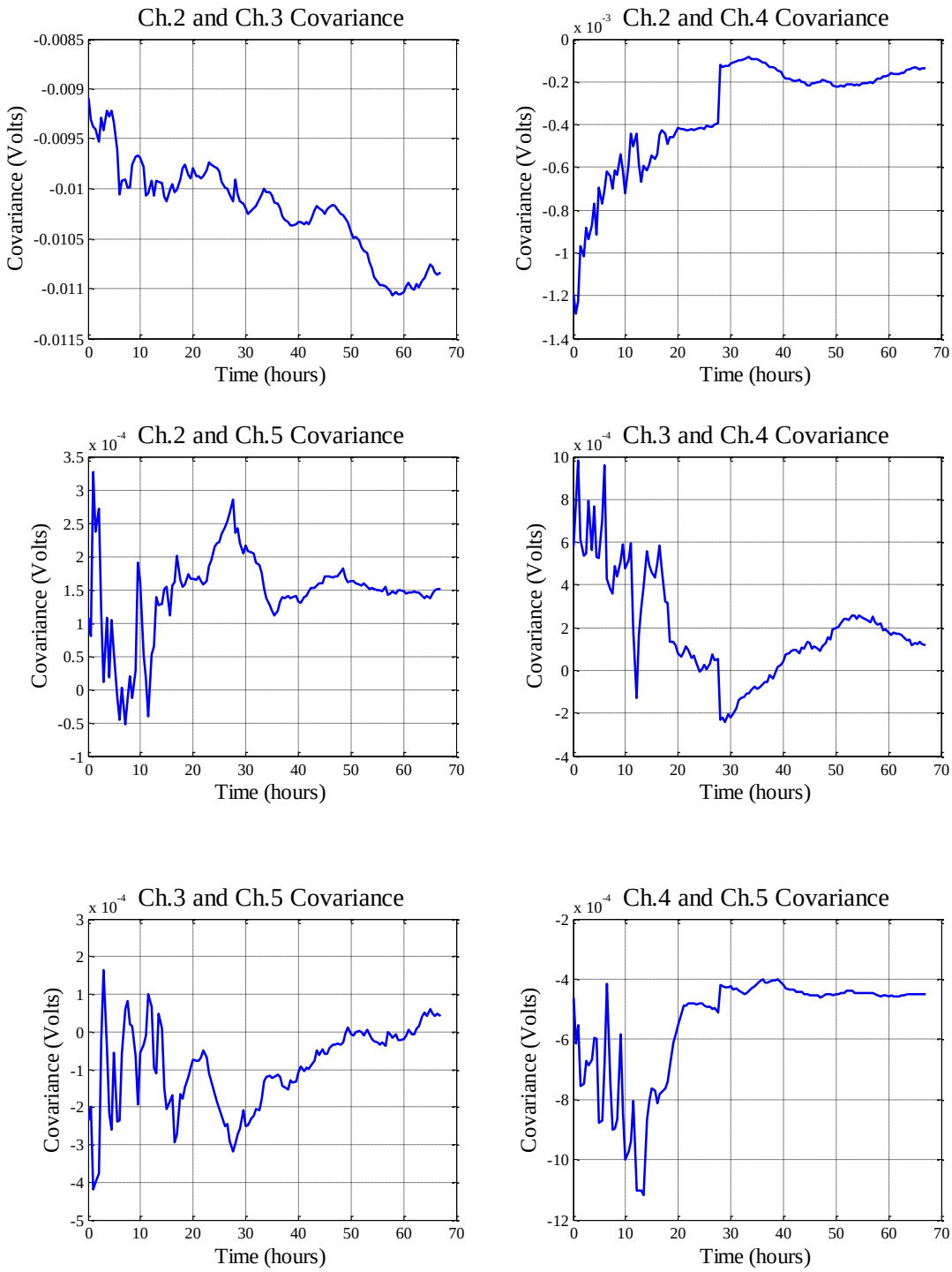

Figure 2. 14 Covariance between sensor group 1 and sensor group 2.

2.2.3.4 Linear Regression Based Damage Estimation

There are multiple linear system identification based approaches were evaluated for anomaly time-series estimation. In this subsection a linear regression based approach is discussed. This is based on the assumption that there exists a transfer function (TF) mapping between individual sensor channel measurements. This TF ideally would stay unchanged if there is no damage. However, if there is any damage, the TF, which has to be recursively estimated, would also change. Tracing the change in parameters of TF, the anomaly or damage time-series can be estimated in real time. This is the basic motivation behind the approach discussed in this subsection and subsequent subsection.

For this purpose, the data was directly mapped across channels to determine a linear relationship of the form

$$\boldsymbol{y} = b_1\boldsymbol{x} + b_0 \tag{2. 3 }$$

where x is the input signal, y is the output signal, b_1 is the regression line's slope, and b_0 is the offset. The regression algorithm solves for the $b_{i=0,1}$ coefficients through the linear system of equations

$$\begin{bmatrix} y_1 \\ y_2 \\ \vdots \\ y_n \end{bmatrix} = \begin{bmatrix} 1 & x_1 \\ 1 & x_2 \\ \vdots & \vdots \\ 1 & x_n \end{bmatrix} \begin{bmatrix} b_0 \\ b_1 \end{bmatrix} \tag{ 2.4 }$$

by using the linear least squares estimation. Figure 2.15 for example displays a scatter plot of channel 2 versus channel 3 and the computed best fit line. While the linear regression fails to completely depict the relationship between the channels, it appears to indicate a general inverse relationship between channels.

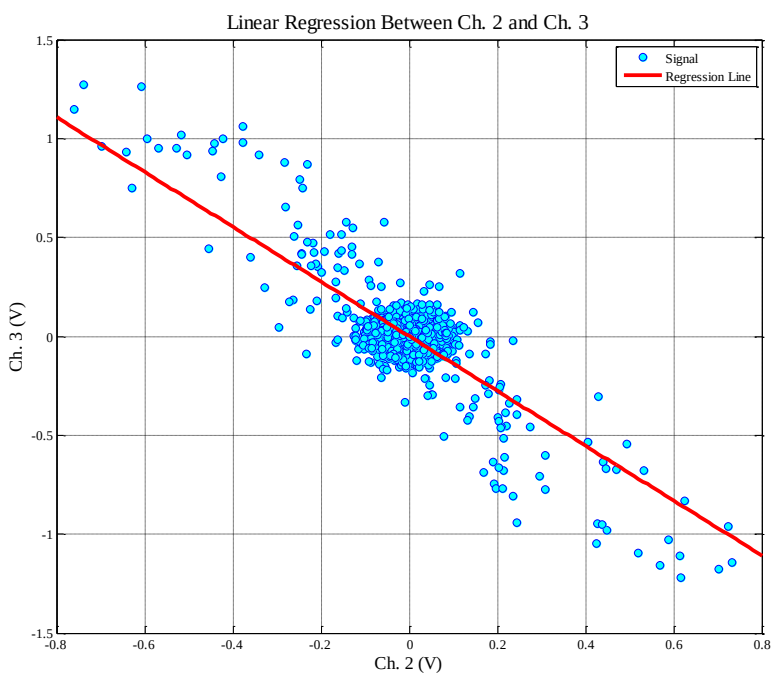

Figure 2. 15 Sample scatter plot of mapping between sensors in group 1 with regression line.

The coefficients for each cycle's best fit line were plotted over the slow scale time axis, illustrated in Figure 2.16, Figure 2.17, and Figure 2.18. Except between Ch. 1 and 5 (Figure 2.17) and Ch. 4 and 5 (Figure 2.18), the offset coefficients, b_0, for the linear mapping across any of the channels did not demonstrate any notable anomalies over the slow scale time axis. Similarly, the slope coefficients, b_1, only for the linear mapping between channel 2 and 3 and channel 4 and 5 displayed a significant anomaly, as exhibited in Figure 2.18. Moreover, the slope coefficient b_1 based anomaly was only observed on linear mapping between sensors on the same sensor group.

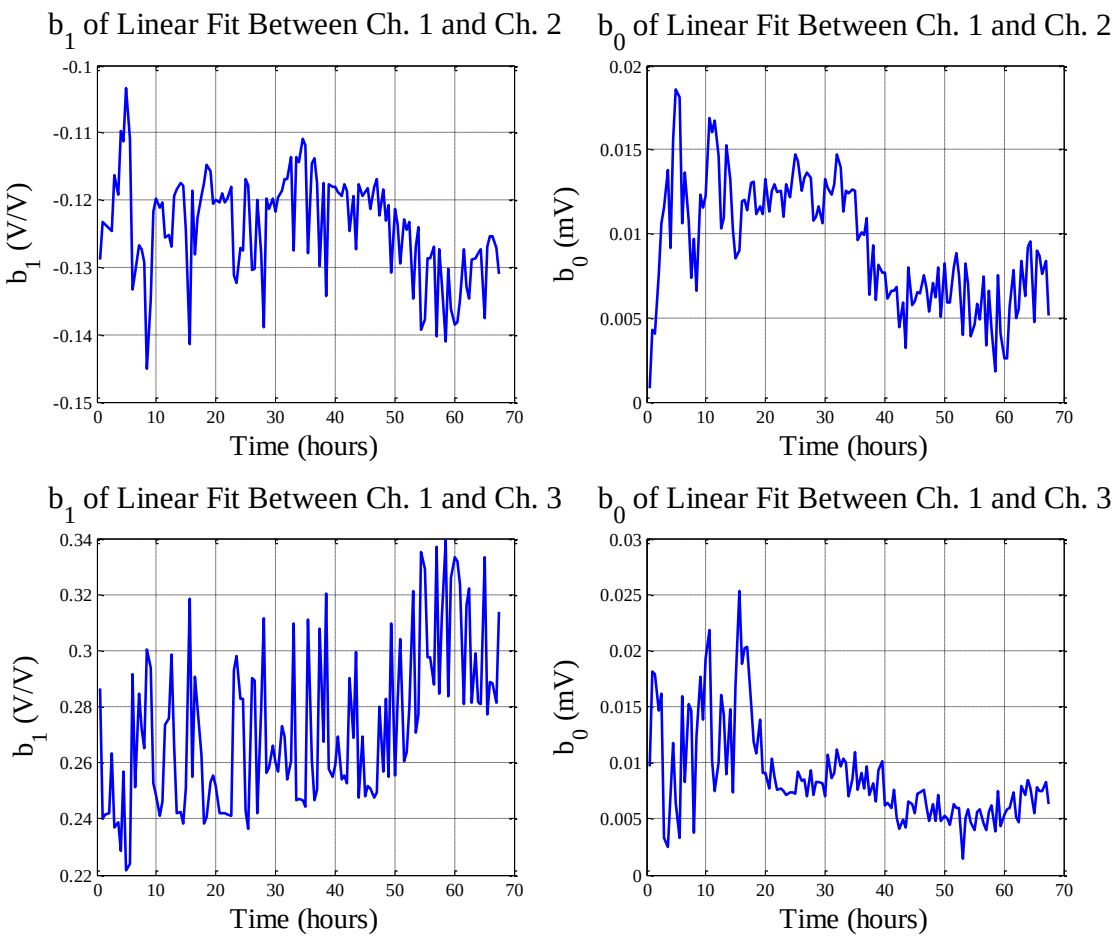

Figure 2. 16 Linear fit parameters (both b_0 and b_1) for mapping between actuator and sensor group 1.

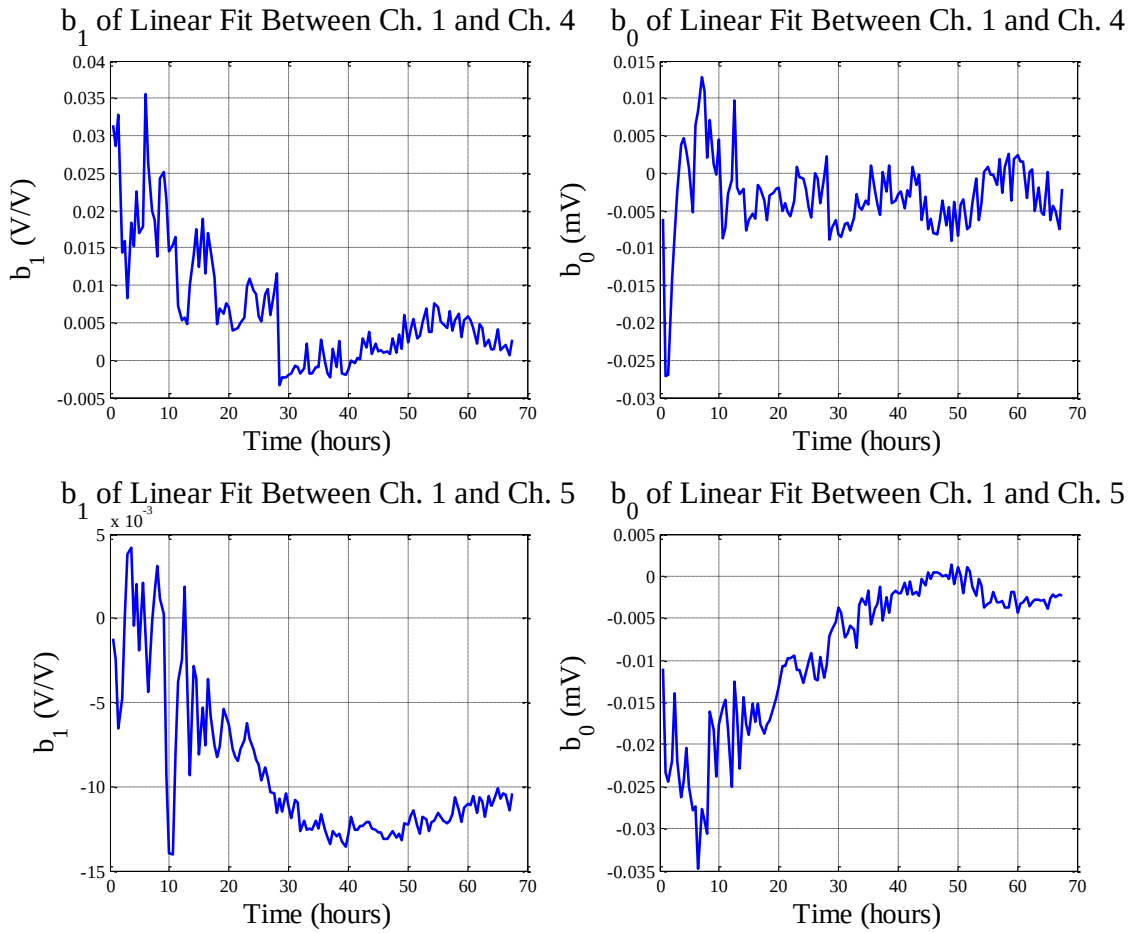

Figure 2. 17 Linear fit parameters (both b_0 and b_1) for mapping between actuator and sensor group 2

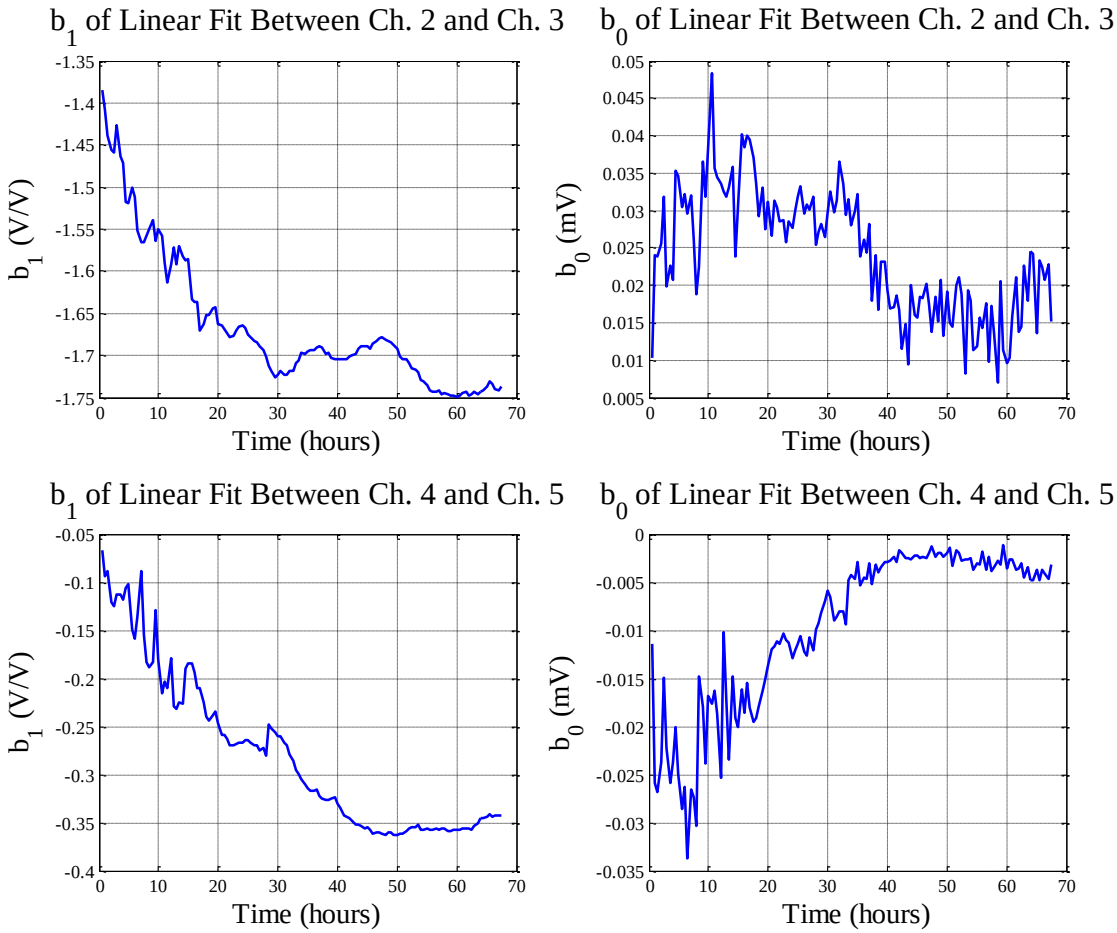

Figure 2. 18 Linear fit parameters (both b_0 and b_1) for mapping between sensors in group 1 (top) and sensors in group 2 (bottom).

Furthermore, using the anomaly observed in the linear regression parameter, b_1, the normalized anomaly trend estimated with respect to the healthy state regression line slope (i.e. b_{1_0}) and using the following root square deviation form:

$$A_n = \sqrt{\frac{(b_{1_n} - b_{1_0})^2}{b_{1_0}^{\ 2}}} \qquad (2.5)$$

where A_n is the damage index at the nth point in the slow scale time axis. The plots of the computed damage indices for the linear mappings between Ch. 2 and 3 and Ch. 4 and 5 are displayed in Figure 2.19 and Figure 2.20, respectively. Both damage indices show strong anomalies over the slow scale time axis. However, both plots demonstrate undesirable features, namely the large valleys between 30-50 hours in the damage index of Ch. 2 and 3 and the damage decline after 50 hours in the damage index of Ch. 4 and 5.

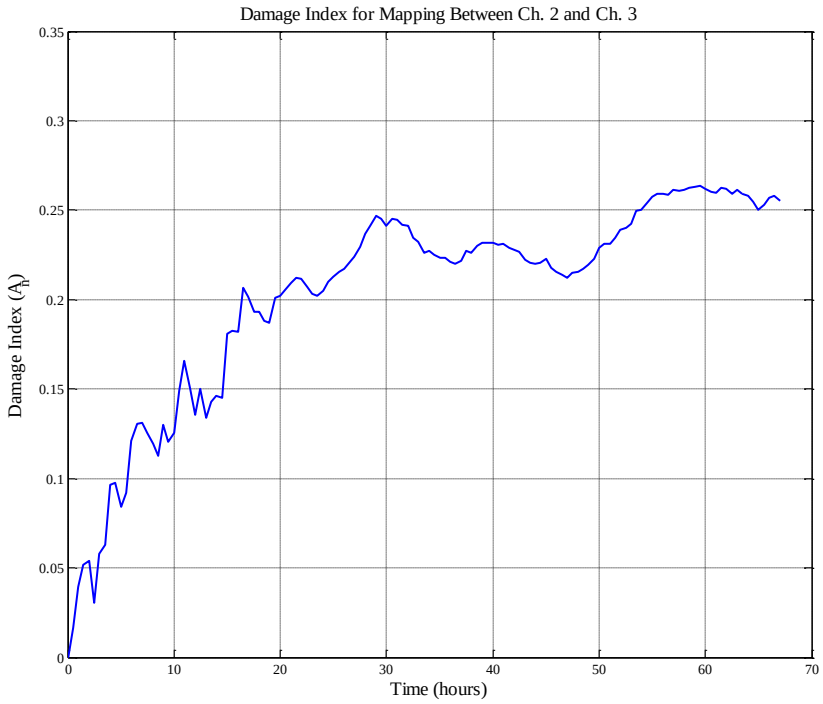

Figure 2. 19 Plot of the damage index computed from linear mapping between sensors in group 1.

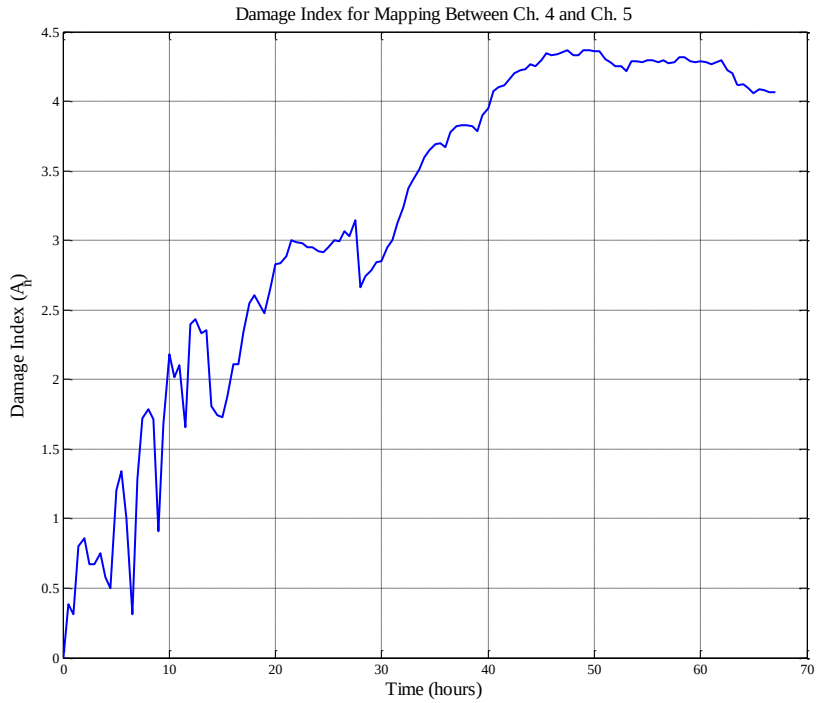

Figure 2. 20 Plot of the damage index computed from linear mapping between sensors in group 2.

2.2.3.5 Correlation Analysis Based Damage Estimation

In addition to linear regression, correlation analysis (CRA) method (a type of linear system identification, [7]) was also evaluated for the slow scale state estimator. Mapping across sensor signals was also performed assuming a linear time invariant relation between the signals from individual channels. For example, the signals from one channel can be assumed as the input, $x(t)$, and signals from another channel can be assumed as the output, $y(t)$, and the transformation between these channels can be expressed as:

$$y(t) = \sum_{k=0}^{\infty} h(k)x(t-k) + v(t) \qquad (2.6)$$

Where the correlation function between the input $x(t)$ output $y(t)$ is given by

$$R_{yx}(\tau) = \sum_{k=0}^{M} h(k)R_x(\tau - k) \qquad (2.7)$$

where $R_{yx}(\tau)$ and $R_x(\tau)$ are the cross correlation and autocorrelation coefficients matrices obtained from equations 7) and (2.9).

$$\hat{R}_{yx}(\tau) = \frac{1}{N}\sum_{t=1}^{N-\tau} y(t+\tau)x(t)^*, \tau = 0,1,2,\ldots \qquad (2.8)$$

$$\hat{R}_{xx}(\tau) = \frac{1}{N}\sum_{t=1}^{N-\tau} x(t+\tau)x(t)^* \tau = 0,1,2,\ldots \qquad (2.9)$$

The correlation function can be alternatively written in matrix form as follows:

$$\begin{bmatrix} R_{yx}(0) \\ R_{yx}(1) \\ \vdots \\ R_{yx}(M) \end{bmatrix} = \begin{bmatrix} R_x(0) & R_x(1) & \cdots & R_x(M) \\ R_x(-1) & R_x(0) & \cdots & R_x(M-1) \\ \vdots & \vdots & \ddots & \vdots \\ R_x(-M) & R_x(-M+1) & \cdots & R_x(0) \end{bmatrix} \begin{bmatrix} h(0) \\ h(1) \\ \vdots \\ h(M) \end{bmatrix} \qquad (2.10)$$

Solving for the transfer function $h(t)$ requires the autocorrelation matrix to be inverted, which is computationally expensive for matrices of large dimensions. Accordingly, only the first 3,000 points of the selected data were used for this method. Figure 2.21 displays the actual and predicted out from CRA using channel 2 as the input and channel 3 as the output. Figure 2.22 displays the actual and predicted out from CRA using channel 4 as the input and channel 5 as the output. Both predictions from CRA did

not closely replicate the actual output. Consequently, CRA was observed not to be an appropriate method for modeling this system.

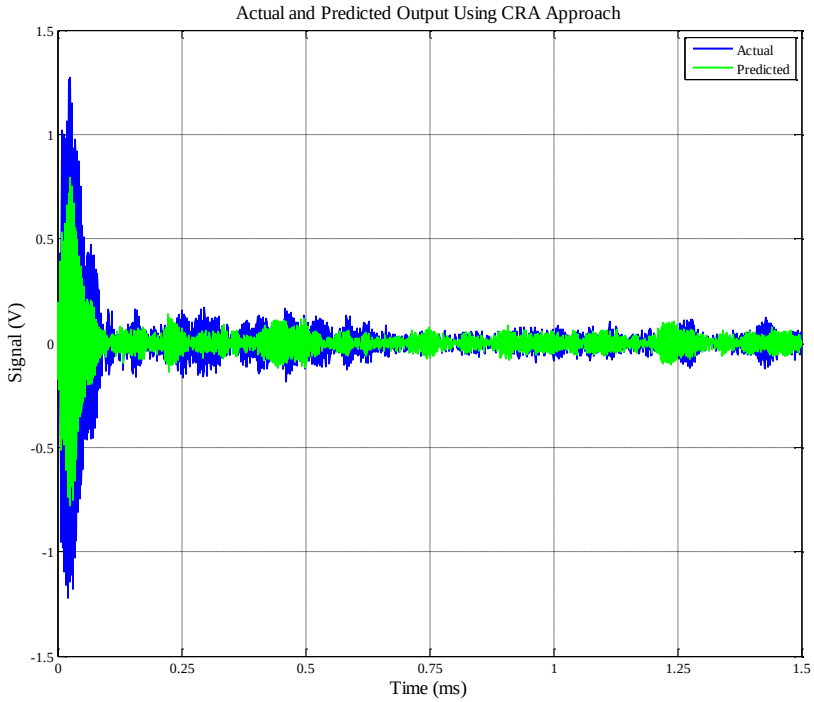

Figure 2. 21 Predicted and actual output using CRA mapping between sensors in group 1.

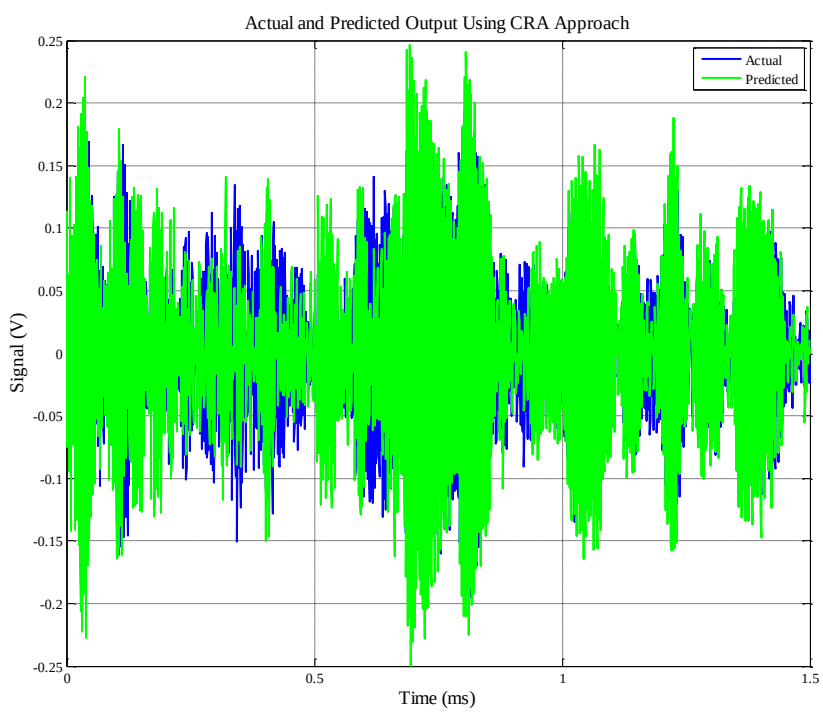

Figure 2. 22 Prediction and actual output using CRA mapping between sensors in group 2.

While the output prediction of CRA was not optimal, the damage index was still computed for the tests using an absolute difference based formula. The damage index was computed according to the expression:

$$A_n = |\varepsilon_n - \varepsilon_0| \tag{2.11}$$

where n is the chirp cycle number. ε_n is the ℓ^2-norm of the prediction error defined by the following expression:

$$\varepsilon_n = \sqrt{\left(y_{ob_1} - y_{p_1}\right)^2 + \left(y_{ob_2} - y_{p_2}\right)^2 + \cdots + \left(y_{ob_i} - y_{p_i}\right)^2} \tag{2.12}$$

where y_{ob_i} is the observed output of the system and y_{p_i} is the predicted output of the system at point i in the nth chirp cycle. The damage index was computed for the CRA method on mappings between channels 2 and 3 and channels 4 and 5. The plots of A_n over the slow scale axis are displayed in Figure 2.23 and Figure 2.24. CRA mapping between Ch. 2 and 3 did not demonstrate a substantial slow scale anomaly. The computed damage index contained a significant component of noise. The damage index between Ch. 4 and 5 demonstrated an anomaly up to 25 hours, but did not reflect and damage growth thereafter. Additionally, this damage index displayed significant noise throughout the slow scale axis. As a result, the CRA method does not effectively describe the system or the damage growth within the system.

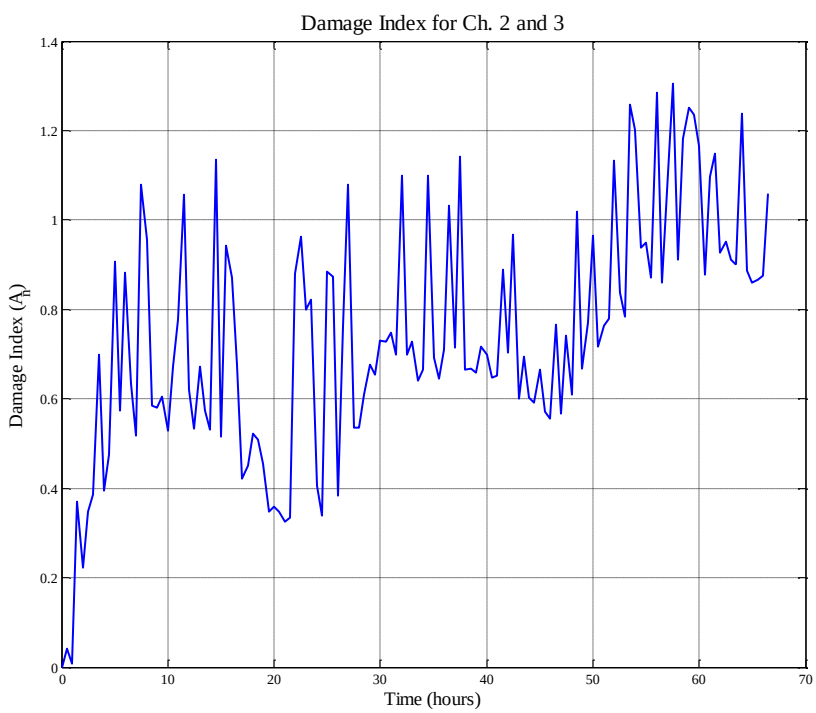

Figure 2. 23 Computed damage index from CRA mapping between sensors in group 1.

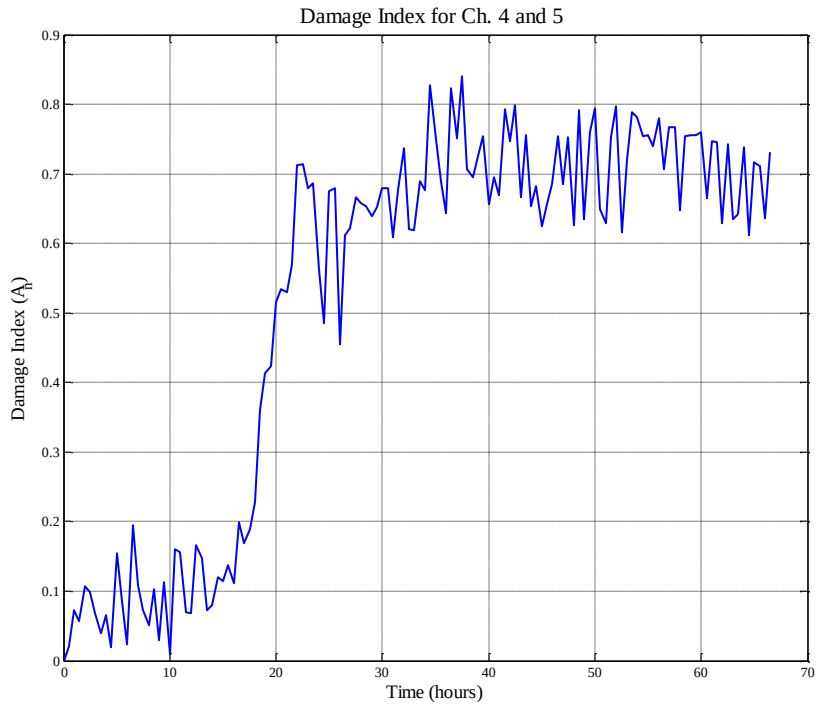

Figure 2. 24 Computed damage index from CRA mapping between sensors in group 2.

2.2.3.6 Empirical Transfer Function Estimation Based Damage Estimation

In addition, another linear system identification technique known as empirical transfer function estimation (ETFE), [7] was also evaluated for the time series anomaly trend estimation. Linear mapping was performed across channels using the ETFE. With this approach, the relationship between the input and output channels is identified by the following system equation:

$$\boldsymbol{y} = P^n(j\omega)\boldsymbol{x} \tag{2.13}$$

In this equation, the transfer function, $P^n(j\omega)$, is expressed as:

$$P^n(j\omega) = \frac{S_{xy}^n(j\omega)}{S_{xx}^n(j\omega)} \tag{2.14}$$

where $S_{xy}^n(j\omega)$ and $S_{xx}^n(j\omega)$ are the cross-spectral power densities and auto-spectral power densities respectively. The spectral densities are calculated using the cross-covariance coefficients, $C_{xy}^n(m)$, and auto-covariance coefficients, C_{xx}^n, as follows:

$$S_{xy}^n(j\omega) = \sum_{k=-M}^{M} C_{xy}^n \omega(k) e^{-j\omega k} \tag{2.15}$$

$$S_{xx}^{n}(j\omega) = \sum_{k=-M}^{M} C_{xx}^{n}\omega(k)e^{-j\omega k} \tag{2.16}$$

where $\omega(k)$ is the lag window used to smoothen the data and M is the trimming parameter for the window. Using the ETFE method, the transfer function was computed and the output channel was predicted and compared to the actual output data. In Figure 2.25, channel 2 was used as the input channel and channel 3 was used as the output channel. The plot overlays the predicted output over the actual output. The resulting response did not closely follow the actual output of the channel. Similarly, in Figure 2.26, channel 4 was used as the input and channel 5 was used as the output. The resulting predicted output was plotted on top of the actual output. Accordingly, the ETFE method did not closely predict a response close to the actual output. Consequently, the empirical transfer function estimation method was concluded to not be an appropriate method to identify the system.

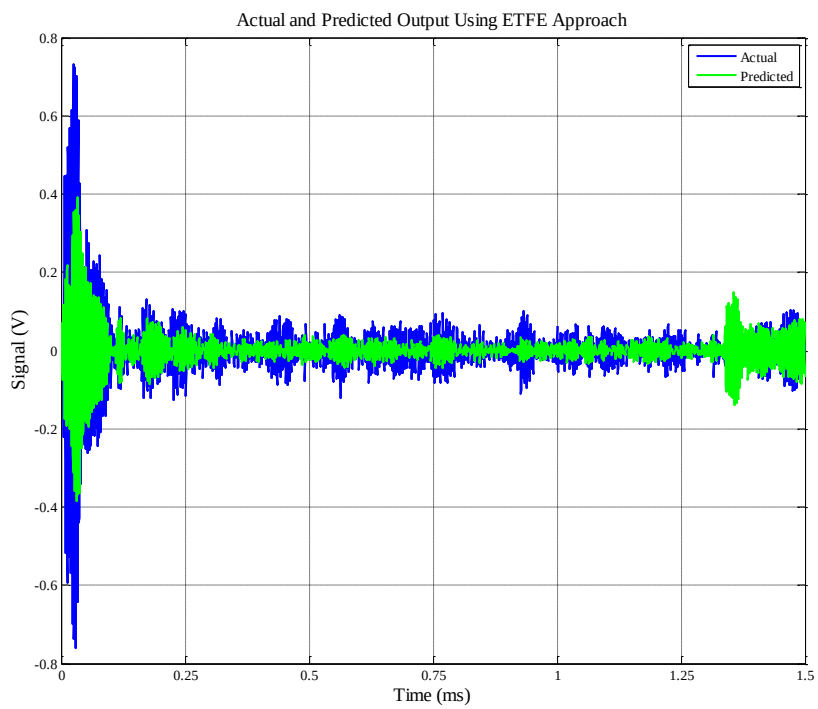

Figure 2. 25 Predicted and actual output using ETFE mapping between sensors in group 1.

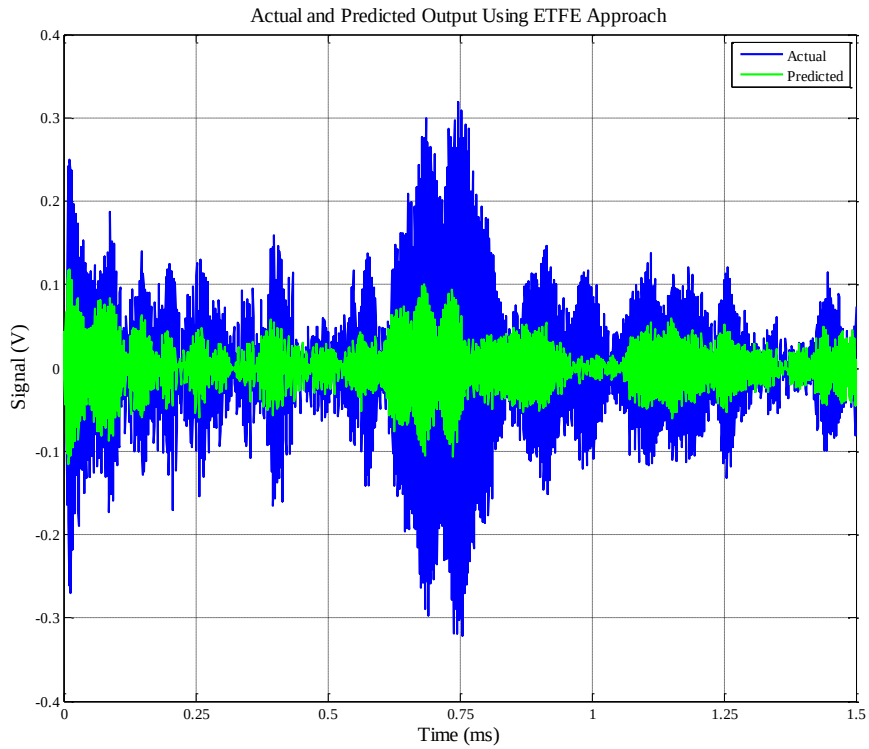

Figure 2. 26 Predicted and actual output using ETFE mapping between sensors in group 2.

While the output prediction of ETFE was not optimal, the damage index was still computed for the tests using a root square deviation based formula. The damage index was computed using the prediction error according to the formulas in equation 2.11 and Eq. 2.12. Both computed indices demonstrate erratic behaviors. The mapping between Ch. 2 and 3 (refer Figure 2.27) did not present an underlying anomaly and demonstrated significant components of noise. The damage index computed for the mapping between Ch. 4 and 5 (refer Figure 2.28) presents an underlying anomaly but has a significant amount of oscillations. Moreover, this damage index does not grow after 40 hours, indicating a blind zone forming. In summary, ETFE was not able to effectively describe the system or capture the overall damage growth within the system effectively.

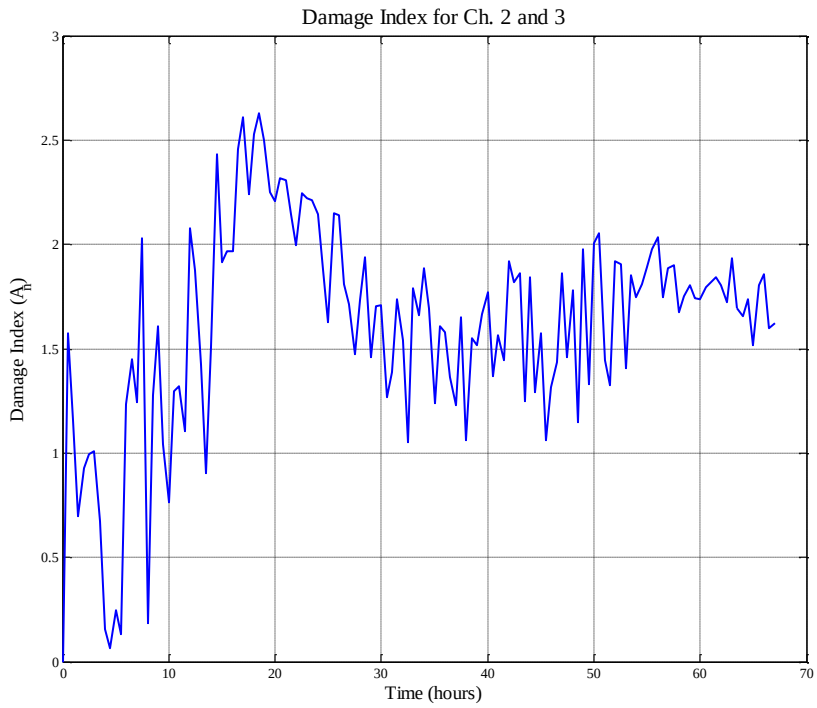

Figure 2. 27 Computed damage index from ETFE mapping between sensors in group 1.

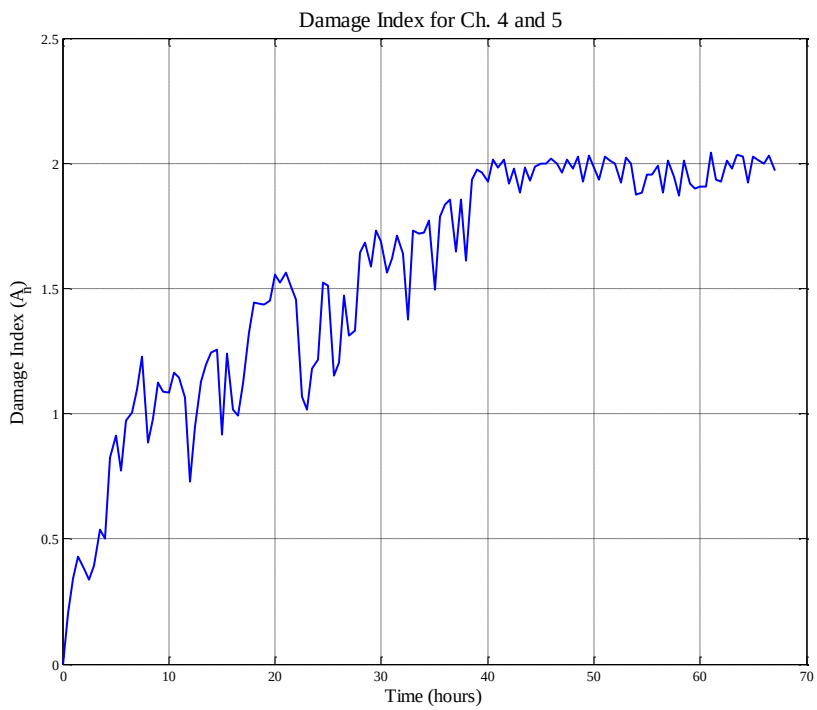

Figure 2. 28 Computed damage index from ETFE mapping between sensors in group 2.

2.2.3.7 Bayesian Forecasting with Gaussian Process Based Damage Estimation

In addition to the linear system identification techniques, nonlinear techniques were evaluated for the slow scale state estimator. Nonlinear estimation was performed across channels using a Bayesian forecasting approach [1,8]. The goal of the forecasting approach is to compute the posterior distribution of the test output, y_{n+1}. The framework accomplishes the prediction by using a random test input, x_{n+1}, a set of n training data points, $\boldsymbol{D} = \{x_i, y_i\}_{i=1,\dots,n}$, and prescribed likelihood and noise functions. The likelihood function can be defined as a prior over the space of possible functions to model the random output by $f(y_i|\alpha; i = 1,2,\dots,n+1)$. Additionally, the noise function can be described as a prior over the noise, $f(\vartheta|\beta)$, where ϑ is an appropriate noise vector that accounts for electrical and physical sources of noise within the specimen. With these factors prescribed, the conditional probability of system as described by the probabilistic model can be written as follows:

$$f\left(y_{n+1}\middle|\{x_{i=1,\dots,n}, \alpha, \beta\}\right) = \int \left(y_{n+1}\middle|\{x_{i=1,\dots,n}, y, \vartheta\}\right) f(a|\alpha) f(\vartheta|\beta) da\, d\vartheta \tag{2.17}$$

The integral in Eq. 2.17 is nontrivial to evaluate. Various methods have been developed to compute the integral including evidence maximization and Monte Carlo simulation. Accordingly, the integral becomes much simpler to evaluate if the underlying function of the signal is governed by a Gaussian distribution. Consequently, the exact analytical form can be written as follows:

$$f\left(y_{n+1}\middle|\{x_{i=1,\dots,n}\}, \boldsymbol{K}_{n+1}\right) = \frac{1}{(2\pi)^{n+1/2}|\boldsymbol{K}_{n+1}|^{1/2}} e^{-\frac{1}{2}(y_{n+1}-\mu)^T \boldsymbol{K}_{n+1}^{-1}(y_{n+1}-\mu)} \tag{2.18}$$

where μ is the function mean and K_n is a nxn kernel matrix. The kernel matrix is computed from the parameterized kernel function described in a later section. Simplifying this expression under the assumption of a function mean of zero, the form can be written as follows:

$$f\left(y_{n+1}\middle|\{x_i, y_i\}, x_{n+1}, k_{ij}(x_i, x_j, \boldsymbol{\Theta})_{i,j=1,2,\dots,n}\right) = \sqrt{\frac{|\boldsymbol{K}_n|}{(2\pi)|\boldsymbol{K}_{n+1}|}} e^{-\frac{(y_{n+1}-\hat{y}_{n+1})^2}{2\sigma^2_{\hat{y}_{n+1}}}} \tag{2.19}$$

where $\hat{y}_{n+1}$ is the next step mean prediction at the output signal data point, $n+1$. The next step predicted mean can be computed by:

$$\hat{y}_{n+1} = \boldsymbol{k}^T \boldsymbol{K}_n^{-1} \boldsymbol{y}_n;\ \ k_i = k(x_{n+1}, x_i)_{i=1,2,\dots,n} \tag{2.20}$$

Similarly, $\sigma^2_{\hat{y}_{n+1}}$ is the next step predicted variance at the output signal data point, $n+1$, which can be evaluated by:

$$\sigma^2_{\hat{y}_{n+1}} = \boldsymbol{\kappa} - \boldsymbol{k}^T \boldsymbol{K}_n^{-1} \boldsymbol{k};\ k_i = k(x_{n+1}, x_i)_{i=1,2,\dots,n};\ \ \boldsymbol{\kappa} = \mathrm{k}(x_{n+1}, x_{n+1}) \tag{2.21}$$

There are many options available for prior interpolating kernel functions. The selected kernel should reflect the assumptions made about the process being modeled. More generally, a kernel function is

required to generate a positive definite kernel matrix for any set of inputs. In this instance, a kernel was created by combining the Gaussian likelihood function to model the signal and the additive measurement noise function to model the noise. The Gaussian likelihood function [8] is written as follows:

$$k_l(y_i|x_i,\theta_l^2) = \frac{1}{\sqrt{2\pi\theta_l^2}} e^{-\frac{-x_i^2}{2\theta_l^2}} \tag{2.22}$$

where θ_l is the likelihood hyperparameter. Similarly, the additive measurement noise function can be described as the following covariance function:

$$k_c(x_i,x_j) = \theta_c^2 \delta(x_i - x_j) \tag{2.23}$$

where θ_c is the scatter hyperparameter. These functions were combined to form the kernel as follows:

$$k(x_i,x_j,\Theta) = \frac{1}{\sqrt{2\pi\theta_l^2}} e^{-\frac{-x_i^2}{2\theta_l^2}} + \theta_c^2 \delta(x_i - x_j) \tag{2.24}$$

All of these Gaussian process proceedings have discussed characteristics of the probability model for fixed hyperparameters. However, to obtain the proper values for these hyperparameters, optimization must be performed. Using a fixed training data set, $D = \{x_i, y_i\}_{i=1,\ldots,n}$, the hyperparameters can be estimated by minimizing the following log likelihood:

$$L = \log(f(\Theta|D = \{x_i, y_i\}_{i=1,2\ldots m}, \mathrm{K}(\cdot))) = -\frac{1}{2}\log(\det(K)) - \frac{1}{2}\mathrm{x}^T\mathrm{K}^{-1}\mathrm{x} - \frac{\mu}{2}\log(2\pi) \tag{2.25}$$

From the log likelihood equation, hyperparameters can be determined through optimization procedures such as Polak and Ribiere nonlinear conjugate gradient method. The method is initialized by selecting a starting value for the hyperparameter, θ, and a step direction, p_k. Next, a line search is performed to determine w_j such that $\theta_{j+1} = \theta_j + w_j p_j$. Next, the algorithm computes the following equations:

$$\psi_{j+1} = \frac{g_{j+1}^T(g_{j+1} - g_i)}{g_j^T g_j} \tag{2.26}$$

where $g_j = \nabla f(\theta_{j+1})$ and

$$p_{j+1} = -g_j + \psi_{j+1} p_j \tag{2.27}$$

The algorithm loops, incrementing j until $\|g_j\| < 1$. Thereafter, the value of θ when the loop is exited is the optimized hyperparameter. The above discussed GP was used in two ways to predict the anomaly trend. First, at any given time with the selected input and output channel data the hyperparameters were estimated and compared over time to check if there is any trend or not. Second, for the given input and output channels the respective model parameters (here the hyperparameters) were estimated at the health

condition of the structure and these fixed hyperparameters were used to predict the output channel data for a given input channel data at any given time. Then, this predicted and actual output data is used to predict the error signals and associated damage index using equation (2.11) and equation (2.12). In both the above mentioned cases the purpose of GP model is to accurately model the input-output relation such that the predicted output best matches the actual output. For example, Figure 2.29 (top plot) displays the predicted channel 3 output and associated 2σ error bounds with respect to channel 2 data as input signals. Figure 2.29 (bottom plot) shows the comparison of mean predicted channel 3 output with actual measured output. Figure 2.30, top and bottom plots, shows the magnified version of Figure 2.29, top and bottom plots, respectively. Additionally, Figure 2.31 (top plot) displays the predicted channel 5 output and associated 2σ error bounds with respect to channel 4 data as input signals. Figure 2.31 (bottom plot) shows the comparison of mean predicted channel 5 output with actual measured output. Figure 2.32 top and bottom plots, shows the magnified version of Figure 2.31, top and bottom plots, respectively. The figures show that the mappings depict a significant improvement in the quality of fit when comparted to the linear system identification models.

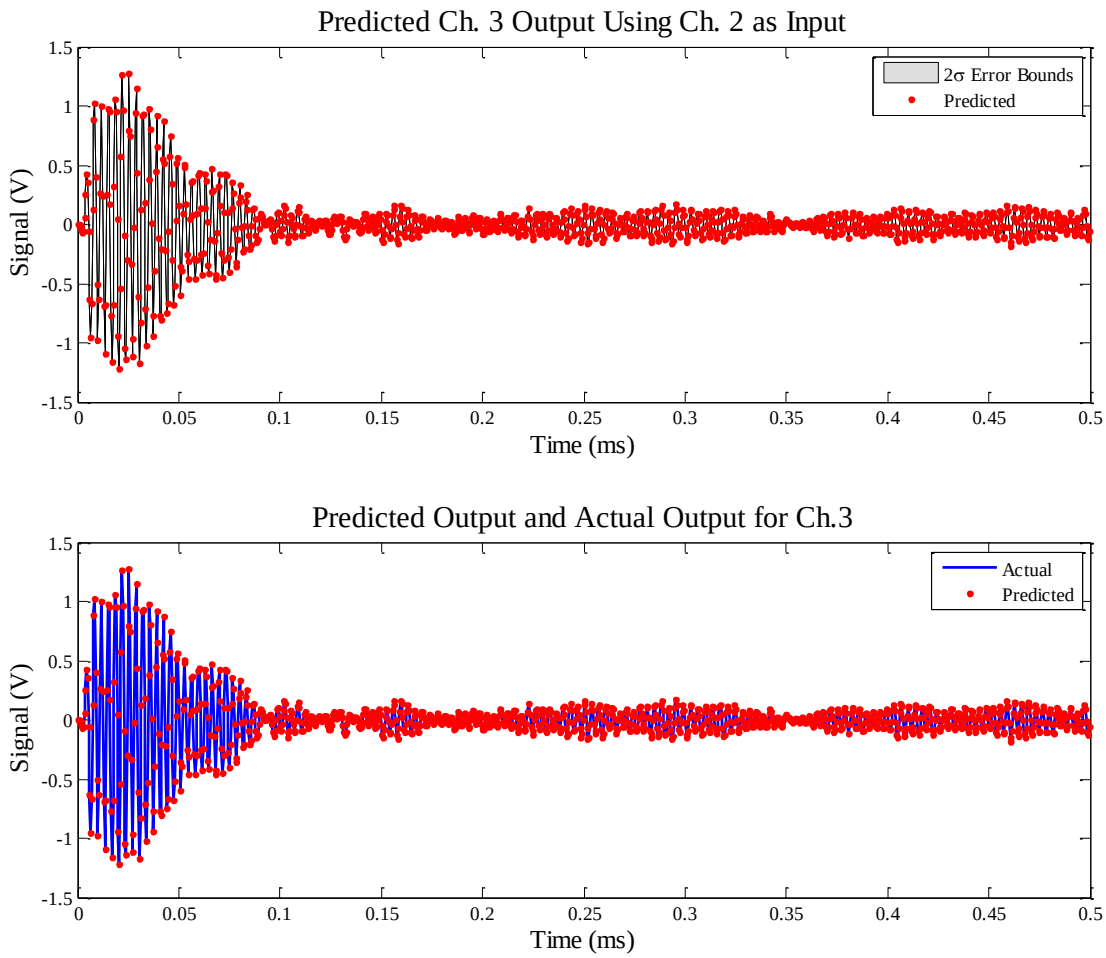

Figure 2. 29 Predicted output with two standard deviation error bounds (top) and predicted and actual output from mapping between sensors in group 1 (bottom).

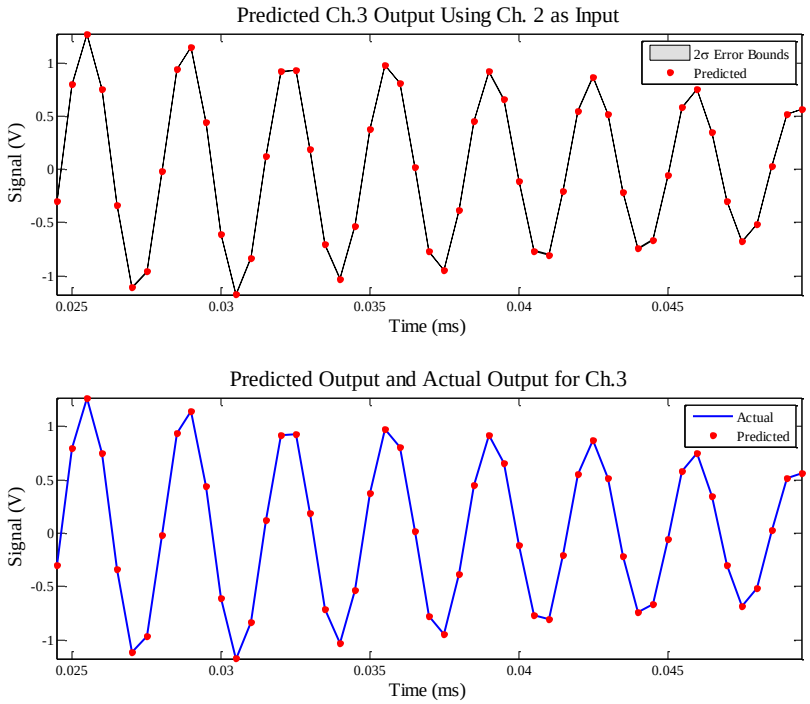

Figure 2. 30 Magnified version of Figure 2.29.

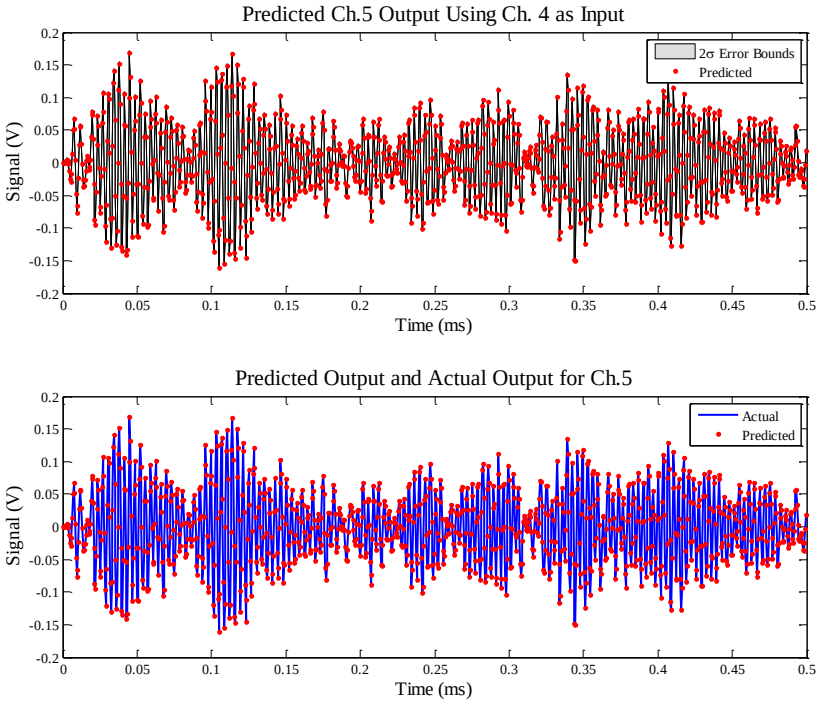

Figure 2. 31 Predicted output with two standard deviation error bounds (top) and predicted and actual output from mapping between sensors in group 2 (bottom).

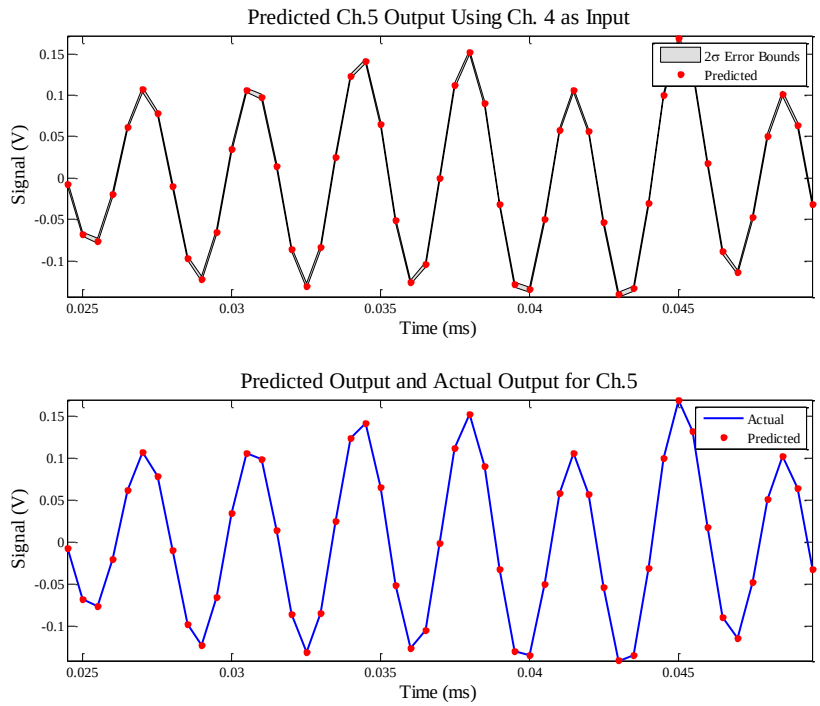

Figure 2. 32 Magnified version of Figure 2.31.

Once the mapping between the input and output signals was established at a given instant, the corresponding anomaly trend was estimated using the above mentioned two approaches. The respective results are discussed below:

Approach-1:

For the first approach of the Gaussian Process based anomaly trend prediction the hyperparameters for each Gaussian Process mapping were plotted over the slow scale time axis. Figure 2.33 depicts the hyperparameters for the mapping between Ch. 2 and 3 and Figure 2.34 depicts the hyperparameters for the mapping between Ch. 4 and 5. In both Gaussian Process mappings, the scatter hyperparameter, θ_c, demonstrates significantly better anomaly trend over the slow scale time axis compared to the likelihood hyperparameter, θ_l. To note that the hyperparameter (θ_c) capture the scatter between the input-output mapping. It is assumed as the structural damage grows due to small microstructural defect there would be more ultrasonic signal reflections or anomaly. This increasing anomaly in form of ultrasonic reflections is ideally to be captured by the scatter hyperparameter. In both cases, the likelihood parameter is much smaller than the scatter hyperparameters. A weighted combination of these hyperparameters to create a hybrid damage index will result in the scatter hyperparameter dominating the overall shape of the damage index.

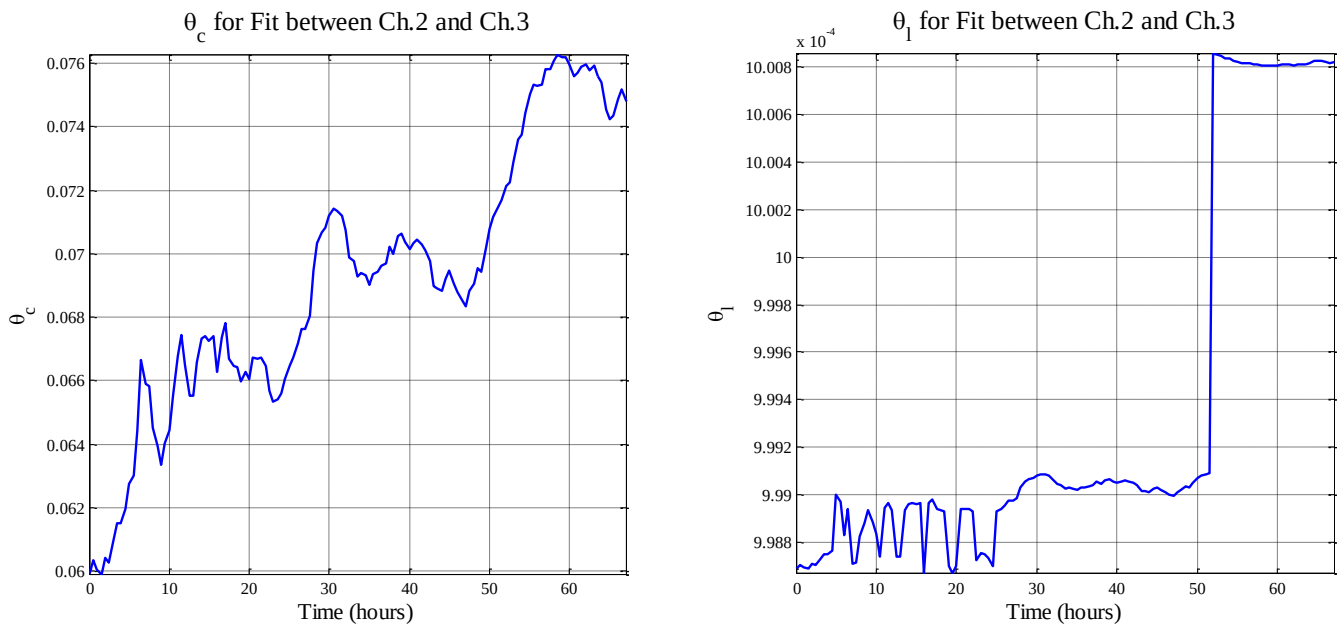

Figure 2. 33 Hyperparameters for Gaussian Process model computed between sensors in group 1.

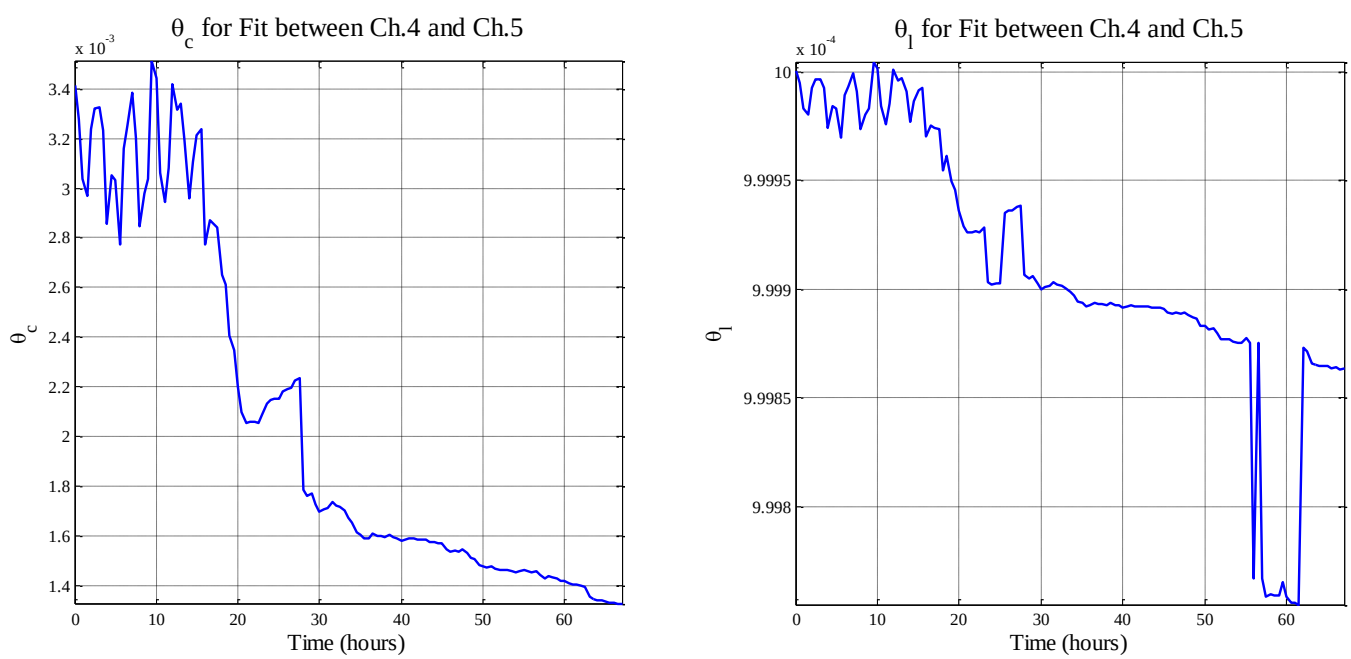

Figure 2. 34 Hyperparameters for Gaussian Process model computed between sensors in group 2.

The ℓ^2-norm of each pair of hyperparameters was computed and plotted over the slow scale. Figure 2.35 and Figure 2.36 display the ℓ^2-norm of the hyperparameters for Ch. 2 and 3 and Ch. 4 and 5, respectively. Both plots take a similar form of the scatter hyperparameters plot since it is much larger than the likelihood hyperparameter. Additionally, the scatter hyperparameter of Ch. 2 and 3 is much larger than that of Ch. 4 and 5.

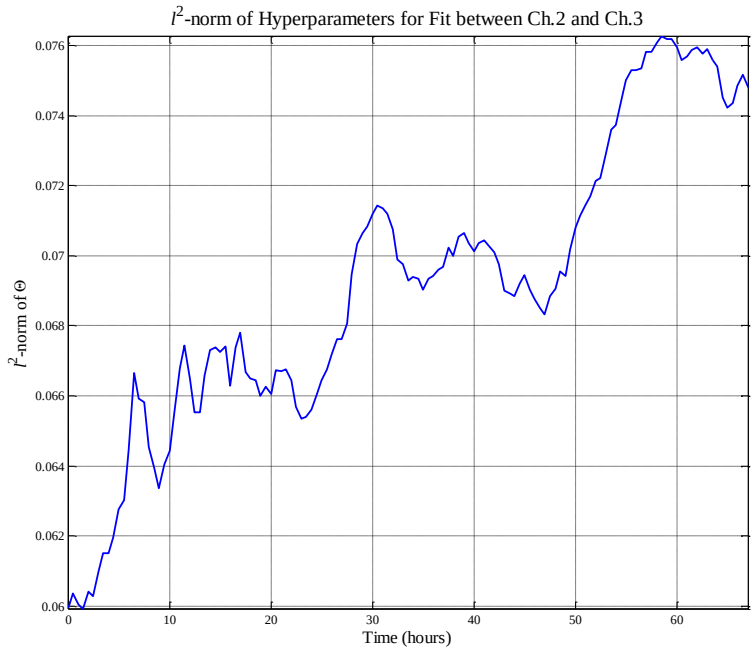

Figure 2. 35 ℓ^2-norm of hyperparameters computed between sensors in group 1.

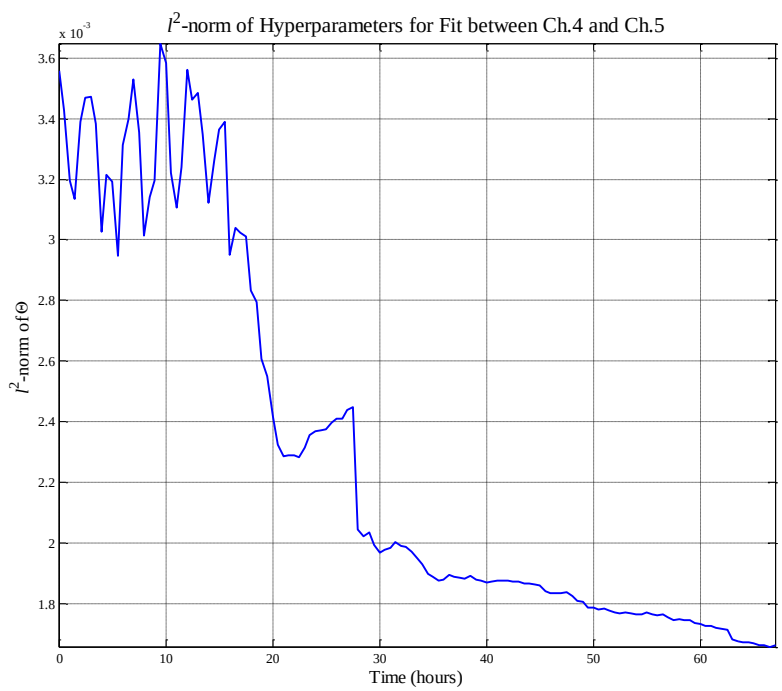

Figure 2. 36 ℓ^2-norm of hyperparameters computed between sensors in group 2.

Approach 2:

The ℓ^2-norm of prediction error was also computed using Eq. 12, but using Gaussian Process mapping. This is to track anomaly trend over slow scale time. The computed prediction error ℓ^2-norm for Gaussian Process mappings between sensors in group 1 and in group are shown in Figure 2.37 and Figure 2.38 respectively. Both plots demonstrate a significant anomaly over the slow scale time axis. However, the trend is similar as the trend estimated through above discussed ℓ^2-norm of hyperparameters (refer Figure 2.36 and 2.37). Similar as Figure 2.36 in Figure 2.38 it can be seen that the prediction error decreases very quickly before 30 hours and does not decrease as significantly afterwards. The lack of variance indicates that there exists a blind zone in sensor group 2 signals as observed through previously discussed methods.

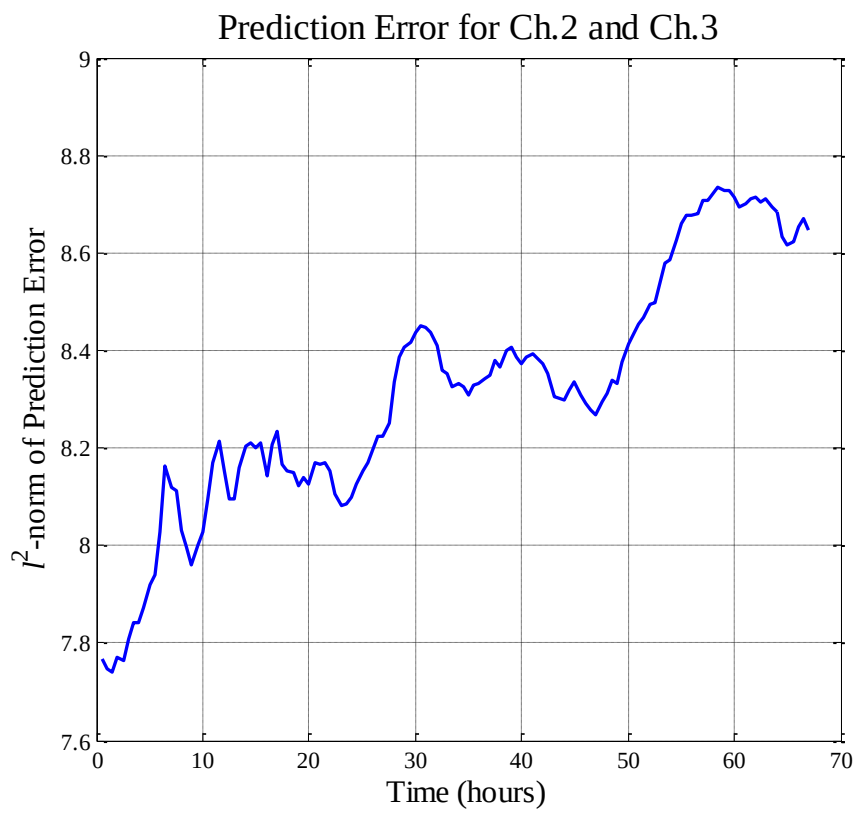

Figure 2. 37 Computed prediction error for Gaussian Process mapping between sensors in group 1 (between channel 2 and 3).

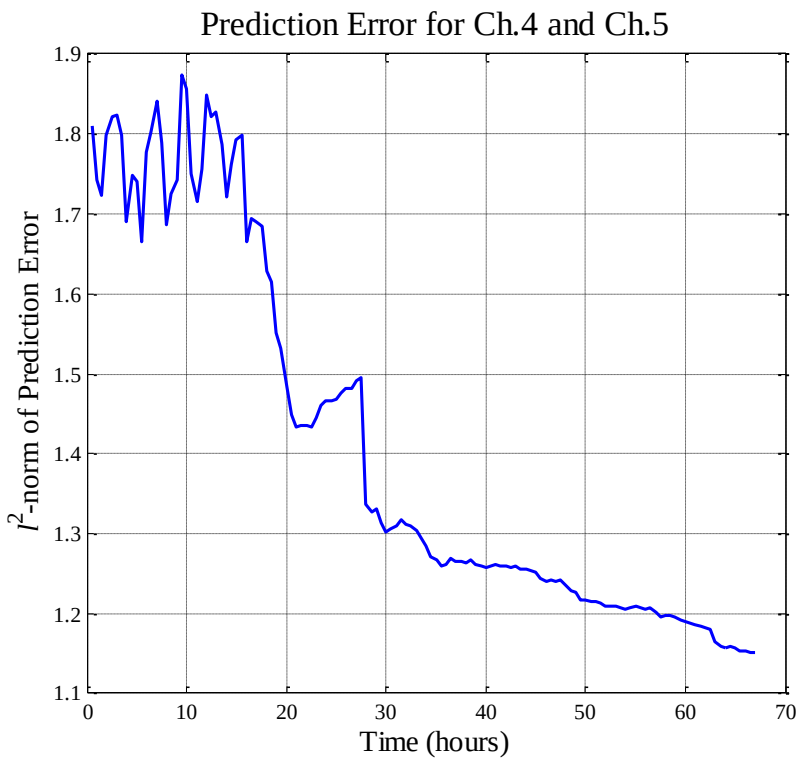

Figure 2. 38 Computed prediction error for Gaussian Process mapping between sensors in group 2 (between channel 4 and 5).

In addition, from the prediction error $\boldsymbol{\ell^2}$-norm, an equivalent healthy state referenced damage index was also computed for the Gaussian Process mappings using Eq. 2.11. The plots of the damage index for the mapping between Ch. 2 and 3 and Ch. 4 and 5 depicted in Figure 2.39 and Figure 2.40, respectively. Unlike Figure 2.37 and 2.38, in both cases, the damage indices demonstrate upward anomaly trends. However, they also demonstrate the same undesirable characteristics (e.g. local valleys) as the prediction error plots discussed in previous sections. Consequently, these recurrent issues are due to the sensor configuration on the specimen. The configuration appears to limit the amount of information each sensor is able to receive since blind zones and other impediments are formed during damage growth. As a result, the implementation of a multi-node data fusion technique is necessary to obtain a complete description of the overall anomaly. This is discussed below.

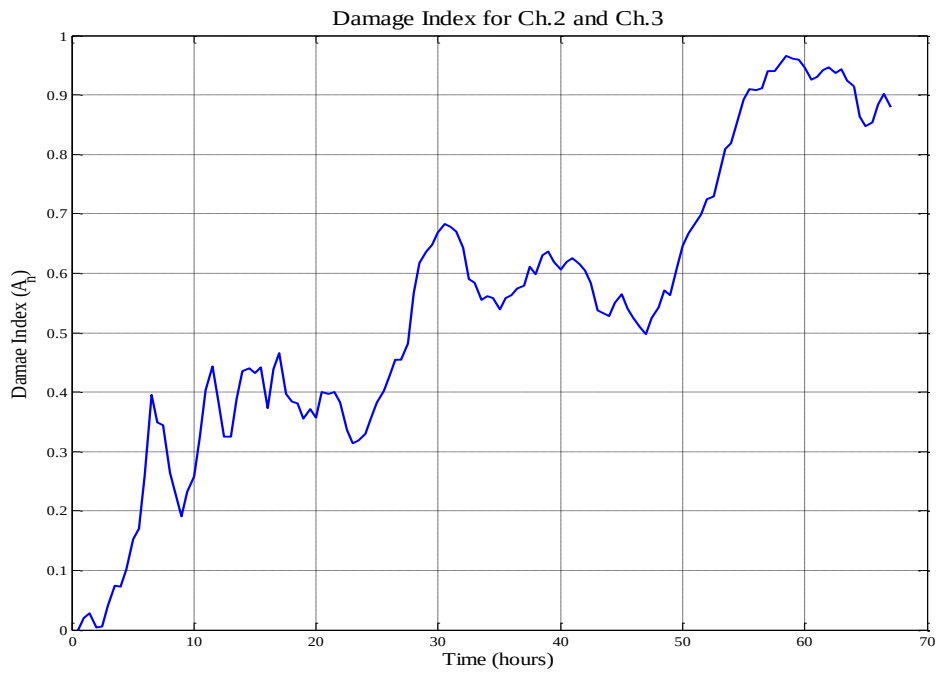

Figure 2. 39 Computed baseline referenced damage index for Gaussian Process mapping between sensors in group 1 (between channel 2 and 3).

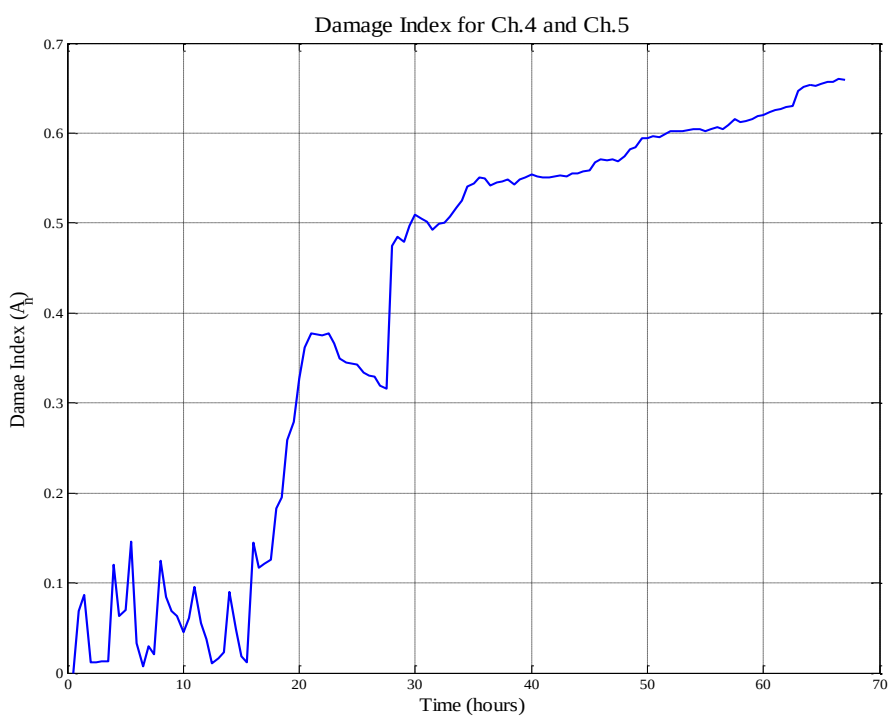

Figure 2. 40 Computed baseline referenced damage index for Gaussian Process mapping between sensors in group 2 (between channel 4and 5).

2.2.4 Multi-Node Sensor Data Fusion

Since the system identification methods presented in earlier sections alone fail to demonstrate a complete picture of the structural degradation from a single pair of sensor channels, multi-node data fusion is necessary. Dimension reduction through principal component analysis (PCA) was chosen as the method for sensor fusion. PCA identifies the direction of the principal components where the variance in changes in dynamics is a maximum. To perform PCA on the damage indices, the data path depicted in Figure 2.41 was implemented. First, consecutive channels were mapped using the Gaussian Process as discussed earlier. From these Gaussian Process mappings, the damage index for each pair of channels was computed using the prediction error method in equations (2.11) and (2.12). Next, these damage indices were processed using PCA dimension reduction technique where the final damage index is computed along the direction of the first principal component.

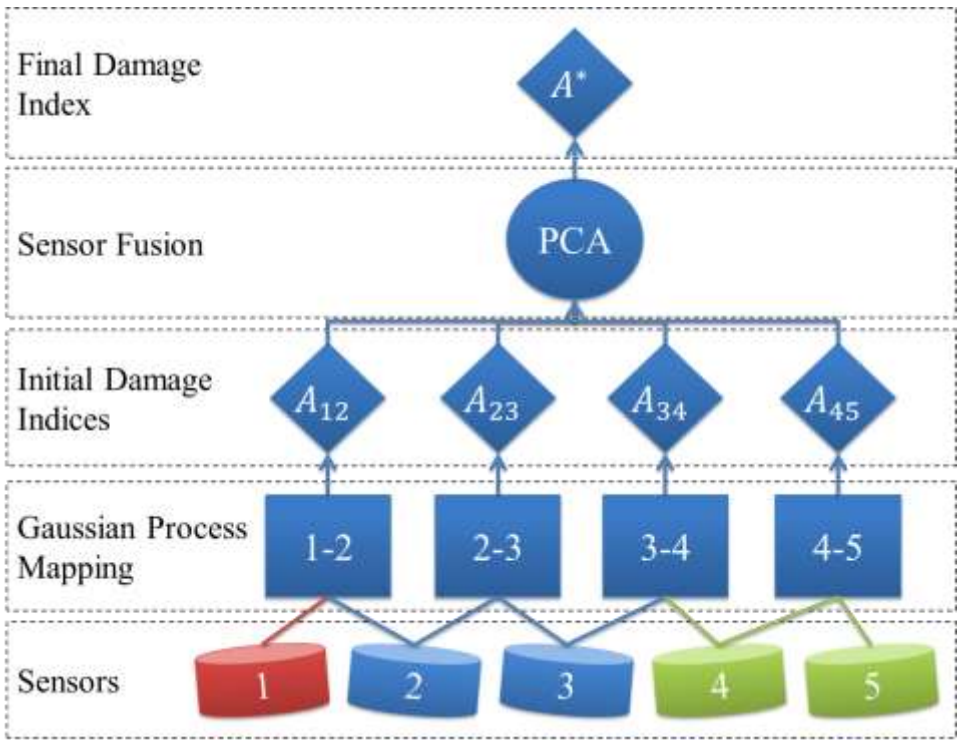

Figure 2. 41 A diagram of the data path for PCA dimension reduction.

To perform PCA, the damage index time series matrix was generated according to the following expression:

$$\boldsymbol{A} = [\boldsymbol{A_{12}} \quad \boldsymbol{A_{23}} \quad \boldsymbol{A_{34}} \quad \boldsymbol{A_{45}}] \tag{2.28}$$

where A_{ij} is the damage index computed from the Gaussian Process mapping between Ch. i and Ch. j. From the $\boldsymbol{A}$ matrix, the covariance matrix, $\boldsymbol{C_A}$, is computed. With the covariance matrix, the principal components can be computed by solving the eigenvalue problem:

$$\boldsymbol{\lambda v} = \boldsymbol{C_A v} \tag{2.29}$$

where the size of the eigenvalue $\boldsymbol{\lambda}$ corresponding to an eigenvector $\boldsymbol{v}$ of covariance matrix $\boldsymbol{C_A}$ equals the variance in the direction v. With these values, a transformation can be obtained to fuse the damage index matrix, $\boldsymbol{A}$, into a single damage index time series. The transformation can be defined as the following:

$$\boldsymbol{A}^* = \boldsymbol{A_{mxn}\Phi_{nx1}} \tag{2.30}$$

where m is the number of measurement points at a given instant and n is the number of cross sensor channel mappings. Also, $\boldsymbol{\Phi}$ is the vector containing the principal component weights and A^* is the new damage index vector for the system. Figure 2.42 displays the damage index time series of the Gaussian Process mappings between Ch. 1 and 2, Ch. 2 and 3, Ch. 3 and 4, and Ch. 4 and 5. These damage index time series were used to compose the damage index matrix, $\boldsymbol{A}$. From the plots of these time series, the wide variability in characteristics of the damage indexes is apparent. For instance, the mapping between Ch. 3 and 4 demonstrates a sharp increase initially, but increases very little after approximately 30 hours. In contrast, the damage index between Ch. 2 and 3 increases much slowly in the early periods of the experiment but experiences large peaks at 30 hours and approximately 58 hours. As a result, by combining the different damage index time series, a more complete picture of the damage growth within the structure can be obtained. Figure 2.43 depicts the resulting damage index time series, which is some sort of equivalent stress corrosion crack growth trend in real time**.** The new damage index $\boldsymbol{A}^*$, demonstrates a complete picture of the damage growth by incorporating features from the original damage index time series. Also, It is clearly evident within the plot that a through wall crack (refer Figure 2.44) occurred at approximately 28 hours since there is a significant change in the damage index value. As a result, by using sensor fusion with the damage index time series, a superior, more complete picture of the damage growth within the structure is obtained.

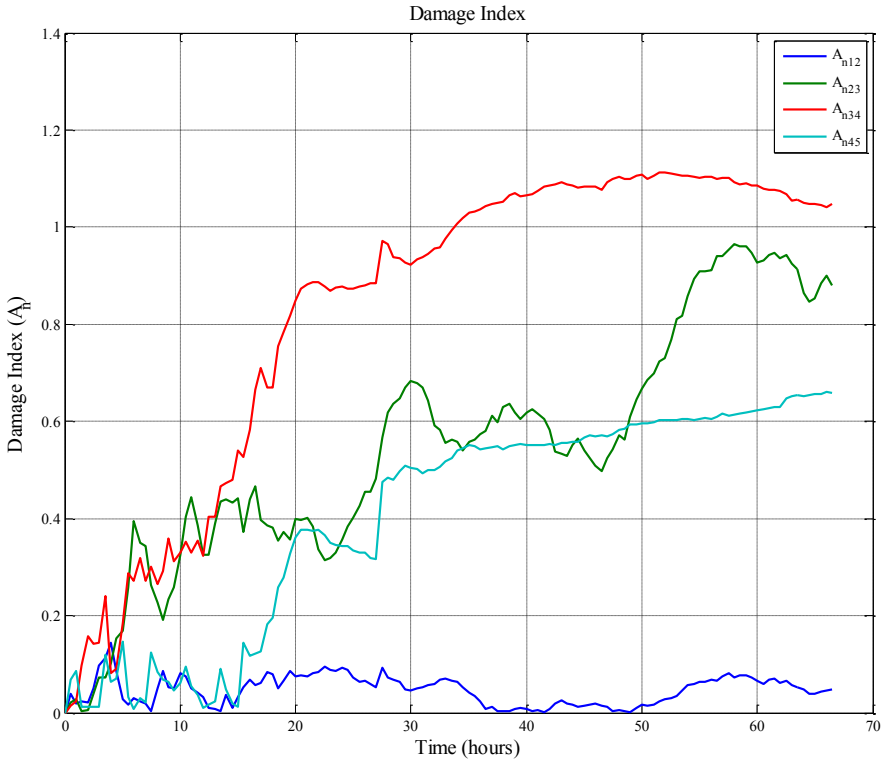

Figure 2. 42 All damage index time series from Gaussian Process mapping.

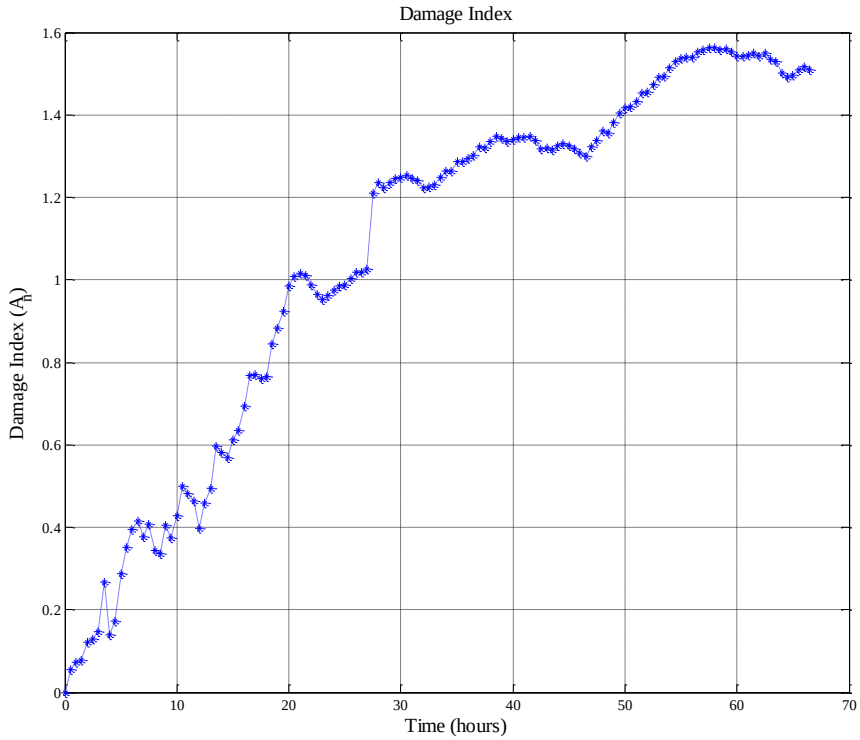

Figure 2. 43 Computed damage index using Gaussian Process mapping and PCA based sensor fusion.

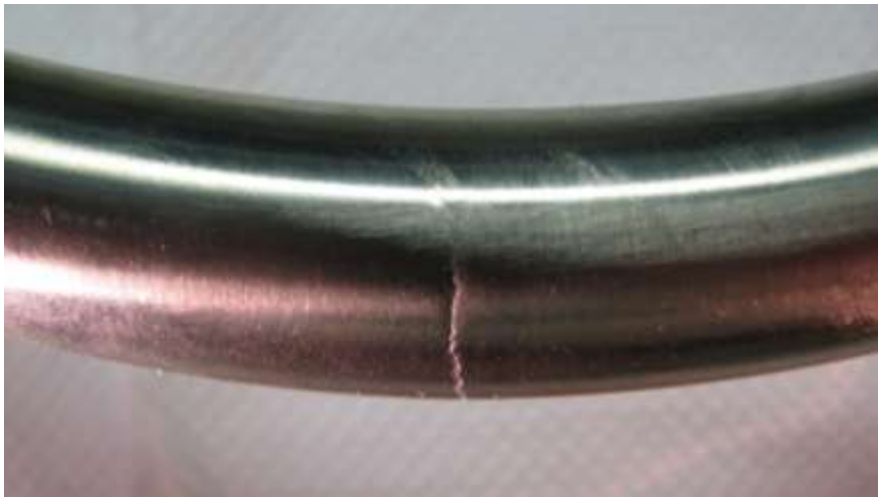

Figure 2. 44 A picture of the U-bend pipe specimen after test.

Since the damage index time series matrix, $\boldsymbol{A}$, increases (due to increasing number of measurement instances, m, as time grows) in size at every state estimation instances, computing the final damage index vector, $\boldsymbol{A}^*$, could vary due to mathematical error within the PCA algorithm. To note that at each new instance, when a new sensor data set is available both $\boldsymbol{A}$ and $\boldsymbol{A}^*$ matrices are recalculated in real time with an additional row of data associated with the newly acquired sensor data set. To determine the effect a growing damage index time series matrix would have on the final damage index vector, the damage index time series was plotted recursively at quarter life, half-life, three quarters life, and end of life and can be seen from Figure 2.45. This plot demonstrates that computing the final damage index vector recursively only affects the value of the damage index by small fractions due to mathematical error. Similarly, Figure 2.46 displays the final damage index computed with the complete damage index time series matrix and the upper and lower range of the damage indices when computed recursively at each pulse interval. The plot also demonstrates that the damage index only fluctuates by very small amounts when computed recursively. Hence, computing the final damage index vector recursively using PCA will not cause major fluctuations within the final damage index vector due to mathematical error.

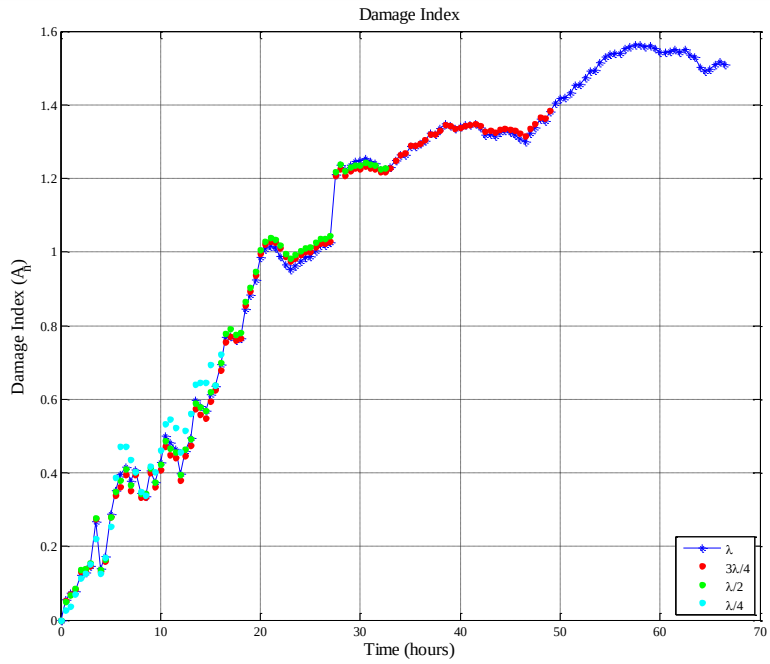

Figure 2. 45 The damage index computed with Gaussian Process and PCA at quarter-life, half-life, three quarters life, and end of life.

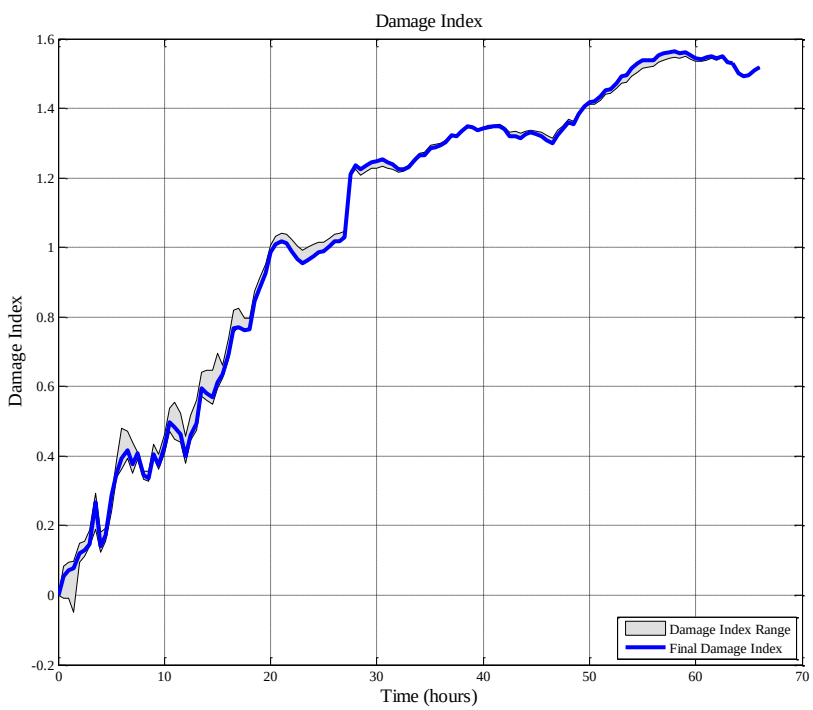

Figure 2. 46 The damage index computed recursively at each damage level with the Gaussian Process and PCA and range in computed damage indices due to mathematical error.

2.3 Conclusion

In this work, the effectiveness of various linear and nonlinear system identification techniques and necessity of sensor fusion was verified for real time structural degradation (here stress corrosion cracking) monitoring in nuclear reactor components. Utilizing the ANL's steam generator tube integrity test intended to evaluate SCC performance for an US-NRC sponsored program; an U-bend pipe specimen was interrogated using the designed online SCC monitoring system. Piezoelectric actuators and sensors were permanently bonded to the structure in two groups at opposing ends of the pipe. The actuator was used to excite the structure with broadband ultrasonic signals while the sensor recorded the response. Using the input and output data, different system identification techniques were tested for their effectiveness in modeling the response and capturing the damage growth within the structure. The experiment revealed that the linear system identification techniques such as linear regression, CRA, and ETFE, did not effectively describe the system transfer function and associated time response. In contrast, the nonlinear technique, Gaussian Process modeling, effectively predicted the transfer function or input-output mapping of the system. However, the Gaussian Process alone failed to completely describe the damage growth within the structure using a single sensor pair necessitating the use of multi-node sensor data fusion. Sensor data fusion was performed on the computed damage indices from the Gaussian Process models for consecutive pairs of sensors using PCA. Sensor fusion of the damage indices demonstrated to be effective in depicting the growth of damage within the structure.

3 A Bayesian Statistic Based Probabilistic Framework for Online Fatigue Usage Factor Monitoring & Remaining Life Forecasting in Nuclear Reactor Components

(Subhasish Mohanty, William Iverson, William K Soppet, Saurin Majumdar and Ken Natesan)

3.1 Introduction

Real time estimation of environmental fatigue usage factor and remaining life of nuclear reactor component is helpful in improving the safety of current generations of light water nuclear reactors and next generation advanced reactors. Utilization of real time measurements of field variables such as stress and strain measurements along with the use of conventional fatigue usages factor estimation tools such as Miner's Rule and the procedure discussed in NUREG/CR-6909 can help to estimate the fatigue usage factor of reactor component in real time. In addition, since large scatter exists in stress/strain versus life data, this scatter can be incorporated in to the real-time usage factor estimation framework through advanced Bayesian statistics based probabilistic modeling techniques such as Gaussian Process (GP). In the present chapter, an integrated GP based Bayesian framework is discussed for real-time and probabilistic fatigue usage factor monitoring & remaining life forecasting in nuclear reactor components. The proof of concept was demonstrated through live constant amplitude fatigue experiments of 316 stainless steel specimens under different conditions such as a) 300 ^{O}C high purity water, b) 300 ^{O}C pressurized water reactor (PWR) primary loop water and c) room temperature in-air condition. In addition, the proof of concept was also demonstrated through simulated fatigue loading with random strain transient and PWR water condition. The theoretical backgrounds behind the proposed concept supported with numerical results are briefly discussed below.

3.2 Theoretical Background

Real time monitoring of usage factor and prediction of remaining useful life can be done for reactor components subjected to reactor environmental fatigue loading. Both usage factor and remaining useful life can be monitored and assessed as safety tools. This monitoring can be done through multiple steps: first, online mean in air usage factor estimation based on ASME in-air strain-fatigue life curve, second, online environmental factor estimation based on US-NRC guide lines, and finally, online probabilistic usage factor estimation to incorporate the scatter in strain-fatigue life curves associated with microstructural structural variability. These steps are discussed below.

3.2.1 Online mean usage factor and remaining useful life prediction under in-air-fatigue loading

Usage Factor, which serves as an expression of life used on a component, is the most effective measurement of fatigue's effect on any given component. Usage Factor is calculated for each individual stress or strain cycle a component undergoes. These cycles are defined as peak and valley pairs. These peaks and valleys can be detected within stress or strain data as the local minima or maxima. Once raw stress or strain data are available, those can be reduced to its peak-valley form. Stress or strain data can directly be acquired in real time using sensors. For example, in a nuclear reactor, component strain

gauges (both uniaxial and multi-axial) can be placed at different hot spots to acquire strain data either continuously or intermittently. Then a standard method, such as the rain flow counting method [9], can be used for stress/strain cycle counting and the corresponding cyclic peak and valley stress/strain amplitude determination. However, if the cycles used for testing are repetitive, in that they go to a uniform minimum and maximum about zero, the rain flow method isn't required and only determining the cyclic peak and valley stress/strain amplitude will suffice. Upon calculation of each stress/strain cycle, usage factor can be found using the following Miner's rule,

$$UF_i = \sum_{k=1}^{i} \frac{n_k}{N_k} \tag{3.1}$$

where:

$UF_i =$ Usage factor at ith fatigue cycle
$i =$ Number of stress or strain cycle amplitudes in loading
$n_k =$ Number of cycles for a given stress or strain amplitude
$N_k =$ Fatigue life of the kth loading cycle (stress or strain)

Fatigue life, N_i, otherwise interpreted as the cycles to failure for a given cycle's amplitude, can be found using the applicable S-N fatigue curve and logarithmic interpolation. For components undergoing fatigue loading under in-air and room temperature conditions, equations of best fit exist from earlier work [10-14]. For austenitic stainless steels the cycle to failure for a given strain amplitude can be found using:

$$\ln(N) = 6.891 - 1.920\ln(\varepsilon_a - 0.112) \tag{3.2}$$

where:

$N =$ Fatigue life, or cycles to failure
ε_a = Strain cycle amplitude, in percent

In real time Eq. 3.2 can be used to estimate the fatigue life at the ith loading cycle (N_i) for a given strain amplitude (ε_a). Once N_i is available using Eq. 3.1 the real time mean usages factor can be estimated. In addition, Eq. 3.1 and 3.2 can be used in calculating remaining useful life, or time to failure. For example, in order to predict remaining useful life for constant amplitude fatigue loading, at least two points of data are required. With this data which relates cycles of stress or strain under which the component has been exposed to usage factor, a linear regression can be done as follows:

$$N_f = b_0 + b_1 UF \tag{3.3}$$

where:

$$b_1 = \frac{n\sum_{i=1}^{n}(x_i y_i) - \sum_{i=1}^{n}(x_i)\sum_{i=1}^{n}(y_i)}{n\sum_{i=1}^{n}(x_i{}^2) - (\sum_{i=1}^{n} x_i)^2}$$

$$b_0 = \bar{y} - b_1\overline{UF}$$

where:

N_f = Predicted cycles for a given usage factor
b_1 = Slope of least squared regression line
b_0 = Cycles undergone intercept of least squared regression line
$x_i = i^{th}$ usage factor data point
$y_i = i^{th}$ cycles undergone data point
$\overline{UF} =$ Mean of usage factor data points
$\bar{y} =$ Mean of cycles undergone data points
n = Number of data points

Once a linear regression has been computed for a given set of data points, the predicted time to failure can be assessed as the point where the usage factor is equal to one. Time to failure can be expressed either as cycles or as time if all cycles have a constant period. Based on the stress or strain cycles undergone by the component in question, the regression may not be perfectly linear, however, even in random loading, linear regression produces good approximations for failure times, and remaining useful life.

3.2.2 Probabilistic modeling of usage factor and remaining useful life

While mean curves for fatigue life are useful in determining when components will fail, they do not provide any insight in the variability of predicting remaining life to failure or usage factor, which can be large. The variability arises due to scatter in stress/strain-life curves which arise due to micro structure variability even though tests were conducted with similar materials under similar circumstances. Using Bayesian statistics based Gaussian Process (GP) probabilistic inference techniques [1, 3, 8, 15-21]; a given historical S-N data set can be mapped offline and can be used in real-time to estimate the mean N_i in Eq. 3.1 and its associated confidence bound. Once the real-time N_i and the associated confidence bound estimated at i^{th} fatigue cycle estimated, the corresponding UF_i and associated confidence bound in usages factor can be estimated in real time. In this context, GP can be incorporated into the present fatigue life monitoring framework. The implementation of GP for probabilistic prediction of Usage Factor and remaining life are described below. First, the historical (or known) strain-fatigue life data is mapped using:

$$f(\boldsymbol{N}|\boldsymbol{\varepsilon_a},\boldsymbol{\theta}) = \frac{1}{(2\pi)^{\mu/2}\sqrt{\boldsymbol{K}}}\exp(-\frac{1}{2}(\boldsymbol{N}-\mu)^T\boldsymbol{K}^{-1}(\boldsymbol{N}-\mu)) \tag{3.4}$$

where:

N = the vector of historical strain- fatigue life data
$\boldsymbol{\varepsilon_a}$ = strain cycle amplitudes
$\boldsymbol{\theta} = a\ set\ of\ hyper\ parameters\ \{\theta_1, \theta_2 \ldots\}$

The hyperparameters $\boldsymbol{\theta}$ have to be estimated prior to the online prediction process and are provided as prior input information. The hyperparameters have to be estimated by minimizing the log likelihood functions given as:

$$L = \log(f(\boldsymbol{\theta}|H = \{\varepsilon_a, N_i\}_{i=1,2\ldots m})) = -\frac{1}{2}\log(\det(\boldsymbol{K})) - \frac{1}{2}\mathbf{N}^T\mathbf{K}^{-1}\mathbf{N} - \frac{\mu}{2}\log(2\pi) \tag{3.5}$$

Gaussian Processes can be used to model the entire historical (available) strain amplitude versus fatigue life data $H = \{\varepsilon_a, N_i\}_{i=1,2\ldots m}$ to a probabilistic input-output map as a black box model. Then the model can be used to predict the output N_i for a given input strain amplitude ε_a at a given instant of time or fatigue cycle. In the above equations, **K** is the kernel matrix which is some sort of covariance matrix which transfers the input-output data to a probabilistic high-dimensional space using a chosen kernel function given as below [8]:

$$k(\varepsilon_{a_i}, \varepsilon_{a_j}) = \varepsilon_{a_i}\frac{1}{\theta_l}\varepsilon_{a_j} + \frac{1}{\theta_l} + \theta_s^2 \tag{3.6}$$

Where, $\theta_l$and θ_s are respectively the width and scatter hyperparameters. In Eq. 3.6 the first term represents some sort of covariance relation between ith and jth strain amplitude, the second term map the bias and third term maps the scatter in data, that could arises due to microstructural variability in stress/strain~life data. Eq. 3.6 represents one of the simplest forms of kernel function and many advanced form of the kernel function can be used for the purpose. A further evaluation of various kernel functions is required, which is one of our future studies. The kernel matrix **K** can be estimated as:

$$\boldsymbol{K}(i,j) = k(\varepsilon_{ai}, \varepsilon_{aj})_{i=1,2\ldots m, j=1,2\ldots m} \tag{3.7}$$

Once the hyperparameters are estimated using the above equations and historical data, the mean life and its variance of new strain amplitude (which would occur at any measured time) can be predicted in real time using:

$$\mu_N = \boldsymbol{k}_t^T\boldsymbol{K}_{\boldsymbol{H}}^{-\mathbf{1}}\boldsymbol{N}_{\boldsymbol{H}}$$
$$\sigma_N^2 = \kappa_t - k_t^T\boldsymbol{K}_{\boldsymbol{H}}^{-\mathbf{1}}\boldsymbol{N}_{\boldsymbol{H}} \tag{3.8}$$

where:

$\mathbf{K_H}$= (m x m) historical kernel matrix
$\mathbf{k_t}$ = (m x 1) vector

and κ is a scalar and can be found by partitioning the larger (m+1) x (m+1) kernel matrix as:

$$\mathbf{K_t} = \begin{pmatrix} \boldsymbol{K_H} & \boldsymbol{k_t} \\ \boldsymbol{k_t^T} & \boldsymbol{\kappa} \end{pmatrix} \tag{3.9}$$

with:

$$k_t(i,j)_{i\,=\,1,2\ldots m, j=m+1} = k(\varepsilon_{ai}, \varepsilon_{aj})_{i\,=\,1,2\ldots m, j=m+1}$$
$$\kappa = K(\varepsilon_{ai}, \varepsilon_{aj})_{i\,=\,m+1, j=m+1}$$

Once the mean and variance are calculated at any given time, the mean life and 2σ (95.4 %) confidence upper and lower limit of life corresponding to strain amplitude can be found as:

$$N_{mean} = \mu_N$$

$$N_{upper} = \mu_N + 2\sigma_N$$
$$N_{lower} = \mu_N - 2\sigma_N \tag{3.10}$$

Then the real time usage factor and the associated 2σ confidence bounds can then be determined using the following equations:

$$UF_m = \sum_{i=1}^{k} \frac{1}{N_{mean}}$$
$$UF_u = \sum_{i=1}^{k} \frac{1}{N_{lower}}$$
$$UF_l = \sum_{i=1}^{k} \frac{1}{N_{upper}} \tag{3.11}$$

As the component is exposed to each loading/fatigue cycle, the usage factor mean and confidence bounds can be estimated in real time. These confidence bounds will compound due to the nature of the usage factor as a recursive function, dependent on all cycles through which the component is strained. In order to estimate the confidence bound projections for time to failure, linear regressions can be done on the mean usage factor curve as well as the curves established for upper and lower estimates of usage factor. This can be achieved through using a similar procedure to estimate mean time to failure described through Eq. 3.3.

The mean usage factor curve can be estimated two ways. While the NUREG or ASME curves exist as least squared regression of data, a Gaussian Process provides a mean directly estimated from historical in air fatigue life data independent of other environmental conditions. While the NUREG or ASME based approach can generate mean usages factor, however utilizing a Gaussian Process provides addition confidence limits in real time usages factor estimation.

3.2.3 Online mean and probabilistic usage factor and remaining useful life prediction under light water reactor environment condition fatigue loading

In air usage factor curves are very different than usage factor curves for components functioning in a light water reactor environment. The mean usage factor curves in various environments, specifically a light water reactor environment, can be expressed using an environmental fatigue correction factor [10-14]. In this real time fatigue monitoring application, this factor is to be calculated in real time and depends not only on stress or strain amplitude but also on additional environmental factors. For the ith fatigue cycle the environmental fatigue correction factor can be defined as such:

$$F_{en} = \frac{N_{air}}{N_{LWR}}$$

(3.12)

where:

F_{en_i} = Environmental fatigue correction factor
N_{air} = Fatigue life in air
N_{LWR} = Fatigue life in light water reactor environment

This allows the environmental fatigue correction factor to be defined as follows with respect to usage factor:

$$UF_{LWR_i} = \sum_{k=1}^{i} F_{en_k} \cdot U_{air_k} \tag{3.13}$$

where:

F_{en_k} = Environmental fatigue correction factor
UF_{LWR_i} = Mean usage factor in a light water reactor environment
U_{air_i} = Mean usage factor in an air environment for a single cycle

In Eq. 3.13, the mean environmental UF_{LWR_i} is to be estimated in real time for each ith fatigue cycle cumulatively. Whereas the in-air usages factors U_{air_k} have to be estimated both using deterministic Eq. 3.1 and 3.2 or by using probabilistic mean usage factor UF_mdescribed by Eq. 3.4 through Eq. 3.11. However the environmental field variable (e.g. temperature, water chemistry such as oxygen concentration, etc.) dependent corrections factors F_{en_k} have to be estimated in real time using the equation provided in NUREG/CR-6909 [12]. For stainless steel the expression for mean environmental fatigue correction factor is as follows:

$$\ln(F_{en}) = 0.734 - T'\dot{\varepsilon}'O'$$

$O' = 0.281$

$\dot{\varepsilon}' = 0$ $\quad (\dot{\varepsilon} > 0.4\%/s)$
$\dot{\varepsilon}' = \ln(\frac{\dot{\varepsilon}}{0.4})$ $\quad (0.0004 \le \dot{\varepsilon} \le 0.4\%/s)$
$\dot{\varepsilon}' = \ln(\frac{0.0004}{0.4})$ $\quad (\dot{\varepsilon} < 0.0004\%/s)$

$T' = 0$ $\quad (T < 150°C)$
$T' = \frac{T-150}{175}$ $\quad (150 \le T < 325°C)$
$T' = 1$ $\quad (T \ge 325°C)$

(3.14)

S = Sulfur content in percent by weight
T = Temperature in degrees Celsius
DO = Dissolved oxygen content in parts per million
$\dot{\varepsilon}$ = Strain rate in percent per second

The above mentioned equation is dependent on certain environmental factors: temperature, dissolved oxygen level, and strain rate, and gives the mean environmental correction factor at any given fatigue cycle and can be found for each stress cycle in real time. In calculating strain rate, average values should be used to determine relevant parameters. However, when calculating temperature, the maximum temperature for a given cycle should be used, as this provides the most conservative estimate. When calculating remaining life, the same linear regression procedure should be used for light water reactor environments as air environments.

These mean curves can be used as reference points for fatigue failure in PWR environments; however, they do not give adequate scope for the variance for fatigue life in a PWR setting. In order to define this variance, a similar GP based procedure described through Eq. 3.4 to 3.11 can be followed to model the historical strain/stress versus life data for under PWR environment. Accordingly the upper bound of the environmental usages factor, $UF_{en\,u}$, and lower limit of the environmental usages factor, $UF_{en\,l}$, can be estimated using Eq. 3.11. To note that the NUREG equation includes the effects of environmental field variables (e.g. temperature, water chemistry such as oxygen concentration, etc.) as independent variables in addition to the strain/stress amplitude. However in the present GP model, the historical data $H = \{\varepsilon_a, N_i\}_{i=1,2\ldots m}$ obtained through environmental fatigue tests are directly considered in the input-output mapping. Hence, in this the strain is the only independent variable. However, the present GP model can easily be augmented to multivariate mapping model with explicitly defining temperature, oxygen concentration, etc. as additional independent variables. This is one of our future research interests.

In the present work, when referencing the historical data for GP based estimation of lower and upper bound of the usages factor, the environmental fatigue correction factor need not be used. The historical data references strain amplitudes in a pressurized water reactor environment, meaning that the effect of the environment is already accounted for.

3.3 Numerical Results

3.3.1 *High purity water and elevated temperature live fatigue test*

Currently at Argonne National Laboratory different fatigue tests are being conducted under department of energy (DOE)'s light water reactor sustainability program. The tests are being conducted for both stainless steel grades (e.g. 316 SS) and low alloy steel (e.g 508) for both base metal and weld (similar/dissimilar) specimens under either in-air room temperature or in-air elevated temperature or under high purity water, elevated temperature or under PWR water, elevated temperature conditions [22]. In the particular example discussed in this subsection, live fatigue monitoring (both live estimation of fatigue usage factor and remaining life forecasting) was conducted on a 316 SS specimen undergoing fatigue testing in a high purity water environment (with DO<5 ppb, Ph=6.4, conductivity <=0.1 uS/cm). The water was maintained at 300 ^{o}C and under pressurized conditions similar in the case of a PWR type rector. The specimen was inside a water tight autoclave and connected to the test frame load cell and actuator through pull rods. Figure 3. 1 shows the environmental (in this case high purity water) test frame and real time fatigue monitoring system. The fatigue monitoring system was developed based on a National Instrument (NI) -PXI chassis with LABVIEW based codes for real-time data acquisition and

MATLAB based codes for real time signal processing and live estimation of fatigue usages factor and remaining useful life.

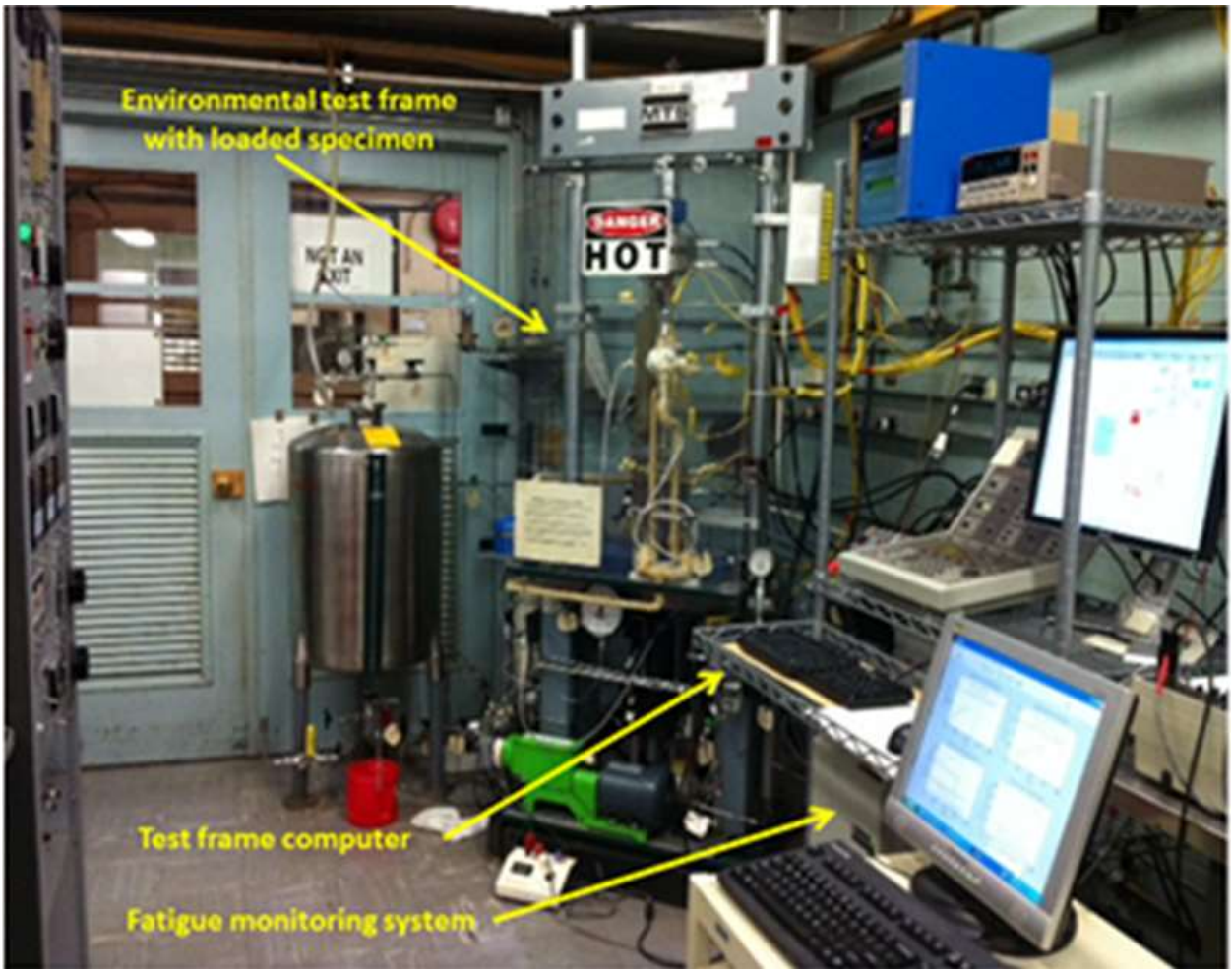

Figure 3. 1 ANL environmental test frame with live fatigue monitoring system.

During fatigue testing, frame stroke signals were collected intermittently through the above mentioned fatigue monitoring system. Since the autoclave is watertight no extensometer could be used for measurement of strain. Typically in a strain control fatigue test, specimen gauge area strains are measured using an extensometer and used for controlling the test. Rather, in this case the crosshead stroke displacement was measured through a Sapphire made displacement sensor and the measured stroke displacement was used for controlling the fatigue test. However, for the purpose of fatigue usages factor monitoring, the stroke measurement were converted to equivalent strain in real time using the following stroke to strain mapping relation:

$$\varepsilon = a_0 + a_1 d_s + a_2 d_s^2 + a_3 d_s^3 + a_4 d_s^4 + a_5 d_s^5 + a_6 d_s^6 + a_7 d_s^7 \tag{3.15}$$

Where, ε and d_s are strain (%) and stroke (mm), respectively. Whereas the polynomial constants are $a_{i=0,1\ldots7}$ = -0.0021055, 2.3843, -74.608, 1704, -12834, 46379, -81825, 56605. The above mapping relation is based on in-air tensile test data earlier conducted at ANL, under similar temperature of 300 ^{O}C and for 316 SS specimen. To note that, in the present fatigue usages factor calculation (based on strain versus life curve based approach) only peak equivalent strains are required and it is assumed that the use of above tensile test based mapping relation can appropriately predict the equivalent peak strains given the peak stroke measurements. In the in-air tensile test a high temperature extensometer was used to measure the gage area strain of the specimen. It is assumed that in real nuclear power plants both uniaxial and multiaxial rosette strain gauge can be mounted outside of the coolant system pipe or pressure vessel to monitor the real time strain in the associated components. In the present test, load cell signals were also collected intermittently to crosscheck the performance of the strain measurement based fatigue monitoring algorithms. It is of note that, in real reactor it may not be always practical to equip the reactor components with load cell and to monitor fatigue usages factor based on load cell (equivalent stress) measurements. However, in the present case, similar to a stroke signal, the load cell measurements can be converted to equivalent strain. For example in this case after converting load to engineering stress, said engineering stress was converted to engineering strain using following expression:

$$\varepsilon = \varepsilon_p + \varepsilon_e = \frac{(\sigma-\sigma_y)}{h} + \frac{\sigma}{E} \tag{3.16}$$

In Eq. 3.16 ε_e and $\varepsilon_p$are the elastic and plastic strain component of total strain ε, h is the hardening constant, E is the elastic modulus and $\sigma_y$is the yield stress, respectively. A preliminary linear isotropic hardening approximation is assumed for estimating the hardening constant h using a strain versus strain curve. For example in this case the hardening constant $h = 244.26\,MPa$, $E = 157.212\,GPa$ and $\sigma_y = 156.067$ were used to transform the stress to strain. The above parameters are estimated using the stress-strain data obtained through an in-air 300 ^{o}C tensile test earlier conducted as part of the LWRS program at ANL [refer T04 tensile test in reference 22]. Figure 3.2 shows the intermittently collected stress history during the entire fatigue test of total 4373 cycles, while figure 3.3 show example of detail stress path during 100-150 seconds. Similarly Figure 3.4 shows the intermittently estimated (from stroke signal) strain history during the entire fatigue test of total 4373 cycles. During the fatigue test each individual cycle load cell and stroke sensor measurements were recorded in a text file, from which the peak and valley for load and stroke with respect to each cycle were determined. These were used to determine the amplitude of each cycle strain either through stroke to strain mapping or through load/stress to strain mapping discussed above. Once the cyclic strain amplitude estimated it was used to estimate the corresponding strain rate to reach that strain amplitude. Once the cyclic strain rate was estimated it was further used to estimate the cyclic environmental correction factor F_{en_k} using Eq. 3.14. Figure 3.5 shows the real time estimated environmental correction factor time history over the entire 4373 fatigue cycles. From the Figure 3.5 it can be seen that the F_{en_k} time history remains flat over the entire fatigue life, because the constant stroke control leads to constant strain amplitude. Use of nearly constant strain amplitude leads to this nearly constant F_{en_k} time history. However, in a real time application with realistic arbitrary stress/strain transients the F_{en_k} time history may not remain flat. This is discussed in a later part of this section through a simulated example. In addition to F_{en_k} at each cycle 'i', the corresponding in-air usage factor was calculated using the Eq. 3.1 and 3.2. This

information was then used to update the ith cycle environmental usage factor UF_{LWR_i} as described through Eq. 3.13. Figures 3.6 and 3.7 respectively show the stroke (or strain) and load (or stress) measurements based real time estimated mean usages factor (blue line) using NUREG-6909 based approach discussed above. From the figures it can be found that both stroke (or strain) and load (or stress) based approach the mean usages factor prediction looks similar. This cross validates both the approaches.

However, in the NUREG based approach discussed above, there is no confidence bound associated with the mean prediction. The estimation of a probabilistic confidence bound is necessary for usages factor estimation since micro structure variability related scatter in stress/strain- life curve can lead to large variation in usage factor estimation either for offline calculation or in the present case of online calculation. To address this issue, in the present work, the GP based approach discussed earlier was also used to estimate the cyclic mean usages factor and the associated confidence bound. For the purpose, once the strain cyclic strain amplitude is estimated in real time, the corresponding fatigue cycle N_i is found using Eq. 3.4. However in Eq. 3.4 the hyperparameters first must be estimated using the historical stress/strain- life data ($H = \{\varepsilon_a, N_i\}_{i=1,2\ldots m}$) and through optimizing the log likelihood function given in Eq. 3.5. These hyperparameters are fixed values and are used as input to the online estimation algorithm. In the present work the strain amplitude versus fatigue life data for stainless steel under high temperature water are used for estimating the hyperparameters. This data is taken from the Japan Nuclear Energy Safety Organization report: JNES-SS-1005 [14]. These data corresponds to PWR water condition fatigue test data and as shown in Figure 3.8. First these stress/strain-life data were converted by logarithmic scaling. It is our assumption that scaling logarithmically will convert the original data to scaled data which follows a normal distribution pattern, and then the Gaussian Process can be used for mapping the stress/strain-life data ($H = \{\varepsilon_a, N_i\}_{i=1,2\ldots m}$). Figure 3.9 shows the histogram and probability density function approximately at 0.6% strain amplitude for PWR water environment case. This example figure confirms that the scaled stress/strain-life data approximately follows Gaussian/Normal distribution. Note that, in the GP mapping all the data shown in Figure 3.8 were used to form the GP model training data i.e. $H = \{\varepsilon_a, N_i\}_{i=1,2\ldots m}$. For a given strain amplitude at a given instant of time the GP model probabilistically interpolate the corresponding fatigue life. In addition, in the present case of high purity water condition, it is assumed that the scatter effect due to microstructural variability will be similar as in the case of PWR water condition.

For each cycle once the strain amplitude is estimated, the corresponding mean fatigue cycle N_i and associated 2σ (95.4%) confidence bounds were estimated using Eq. 3.10. Figure 3.10 shows the GP estimated logarithmically scaled mean N_i and associated 2σ confidence bound at different fatigue cycles. From the figure it can be seen that mean N_i and associated 2σ confidence bound remain fairly constant although these are calculated in real time. This is because of the constant stroke (and hence strain) amplitude fatigue test. This may not be the case for real life random loading case. Using these GP estimated mean fatigue life and the associated 2σ confidence bounds, the ith cycle mean usages factor and the associated confidence bounds were updated in real time using Eq. 3.11. From the Figure 3.6 and 3.7 it can be seen the GP estimated mean usages factor and associated confidence bound based on stroke/strain sensor measurements and load/stress sensor measurements. From the figures it can be seen that the GP estimation yields fairly similar results for both stroke/strain and load/stress based approach. In addition it can be seen that GP based mean usages factor history have similarity with the NUREG based mean usage factor history. The mean curves may not exactly match each other because of the data

set used in the both the cases and the extent of approximation used in both the cases. The purpose of the present work is to demonstrate how in real time probabilistic usages factor can be calculated and rigorous validation is beyond the scope of this exercise.

Similar to the usage factor, the remaining useful life (RUL) can be estimated in real time either using above discussed NUREG based usage factor calculation or GP based usages factor calculation. However, unlike the NUREG based approach the GP based approach can generate not only the mean RUL but also the associated 95.4% confidence bound. As discussed earlier the RUL is calculated based on linear approximation of real time estimated fatigue cycle versus usages factor data and using Eq. 3.3. Figure 3.11 and 3.12 shows the time history of stroke/strain and load cell/stress sensor measurement based RUL forecasting, respectively.

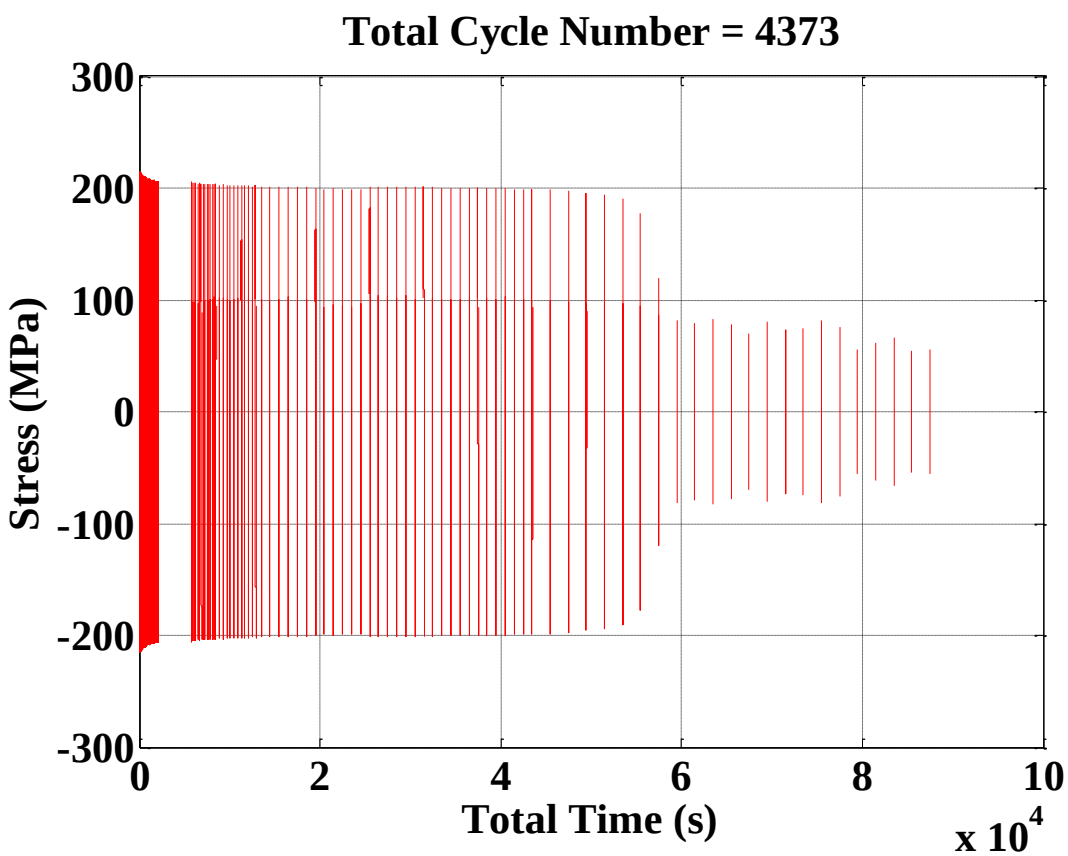

Figure 3. 2 Intermittent cyclic stress history for the high purity water fatigue test (F11).

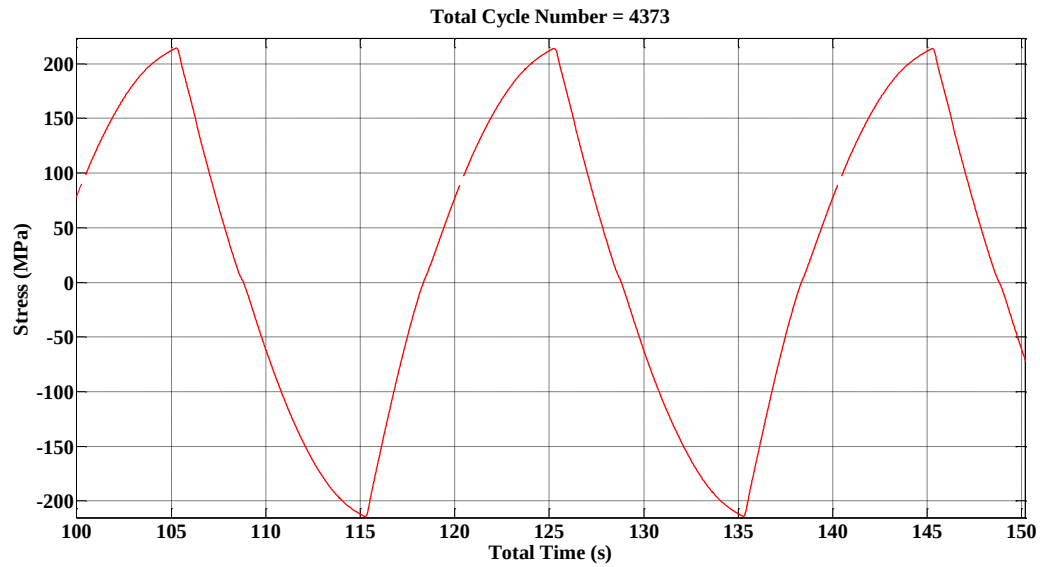

Figure 3. 3 Magnified (between 100-150 seconds) stress history of F11 test.

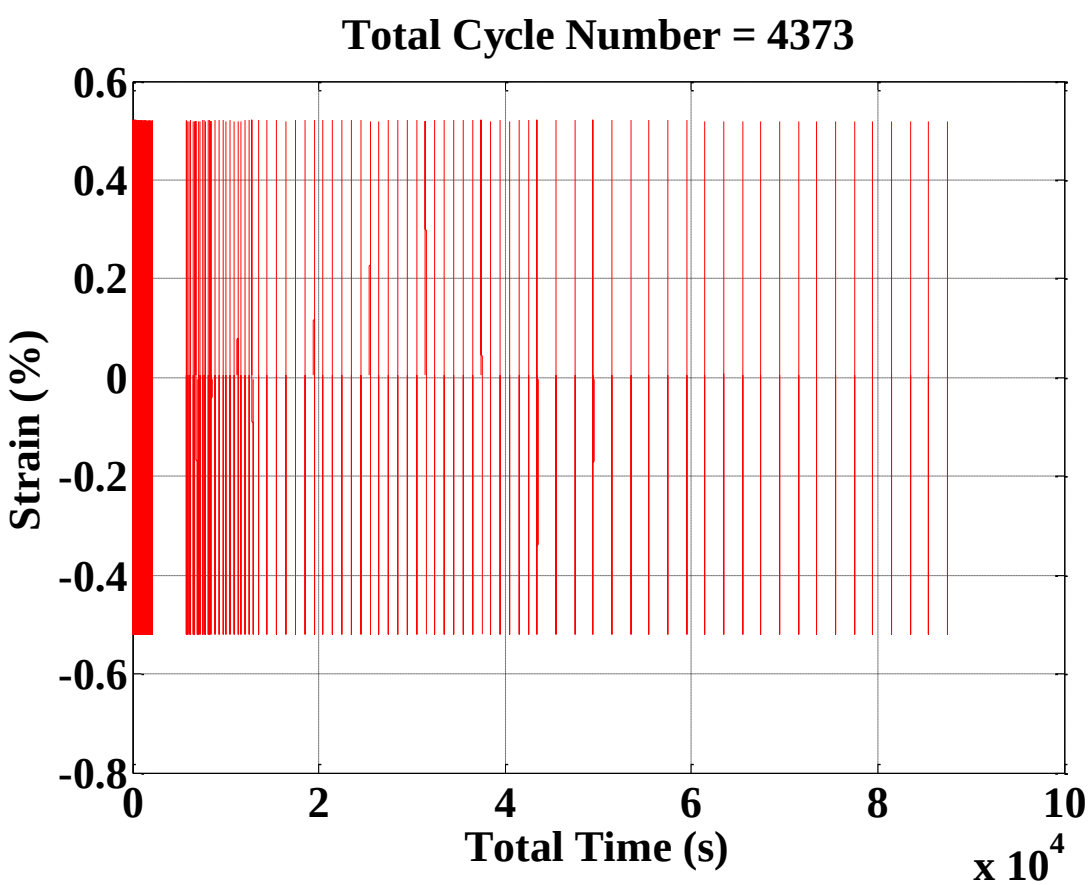

Figure 3. 4 Intermittent transformed cyclic strain history for the high purity water fatigue test (F11) using stroke-strain mapping.

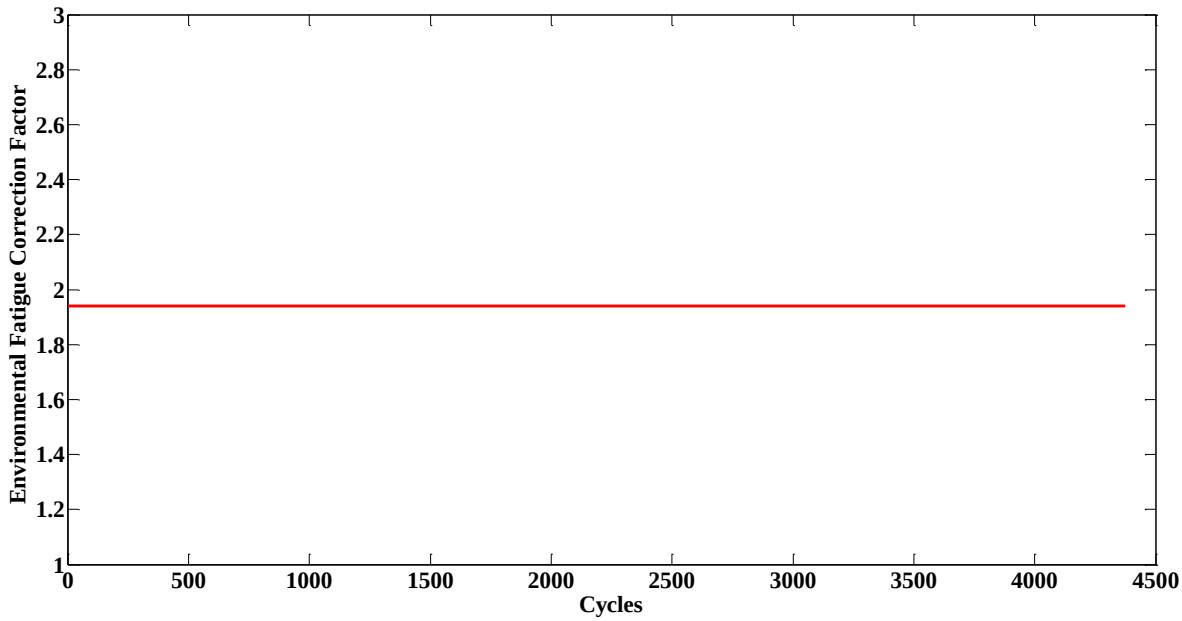

Figure 3. 5 Time history of environmental correction factor F_{en_k}.

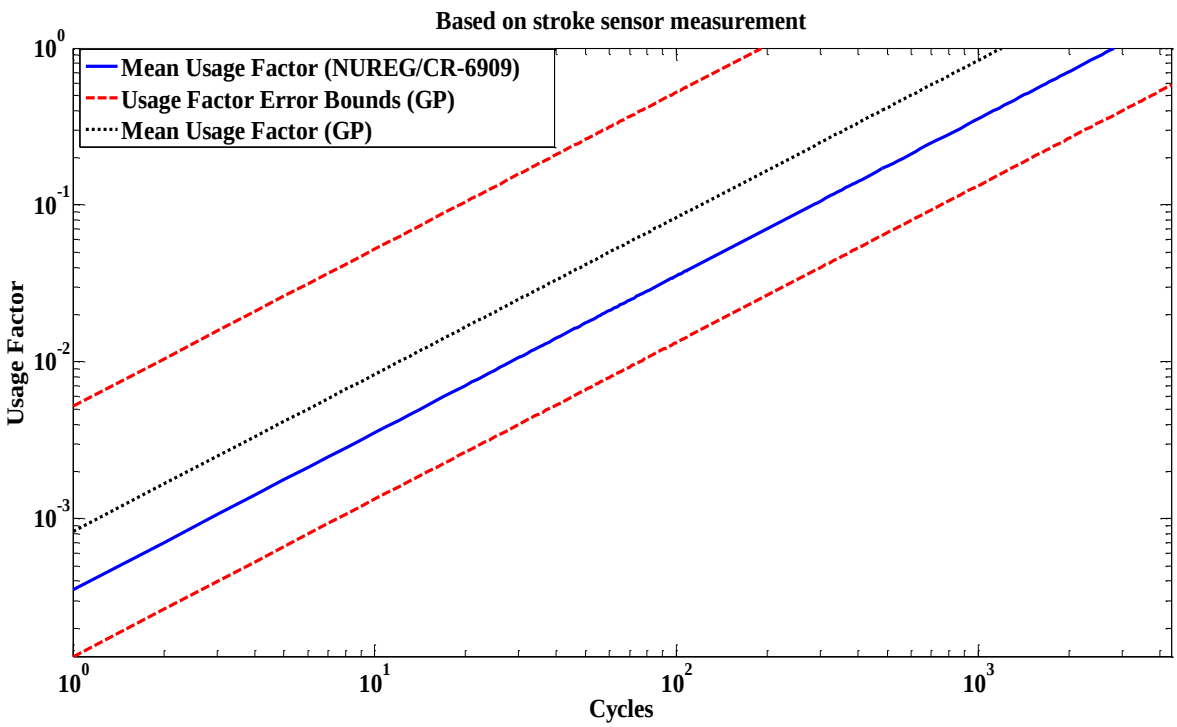

Figure 3. 6 Stroke sensor measurement based real time estimated usages factor time history for the high purity water fatigue test (F11) using both NUREG-6909 based approach and GP based approach.

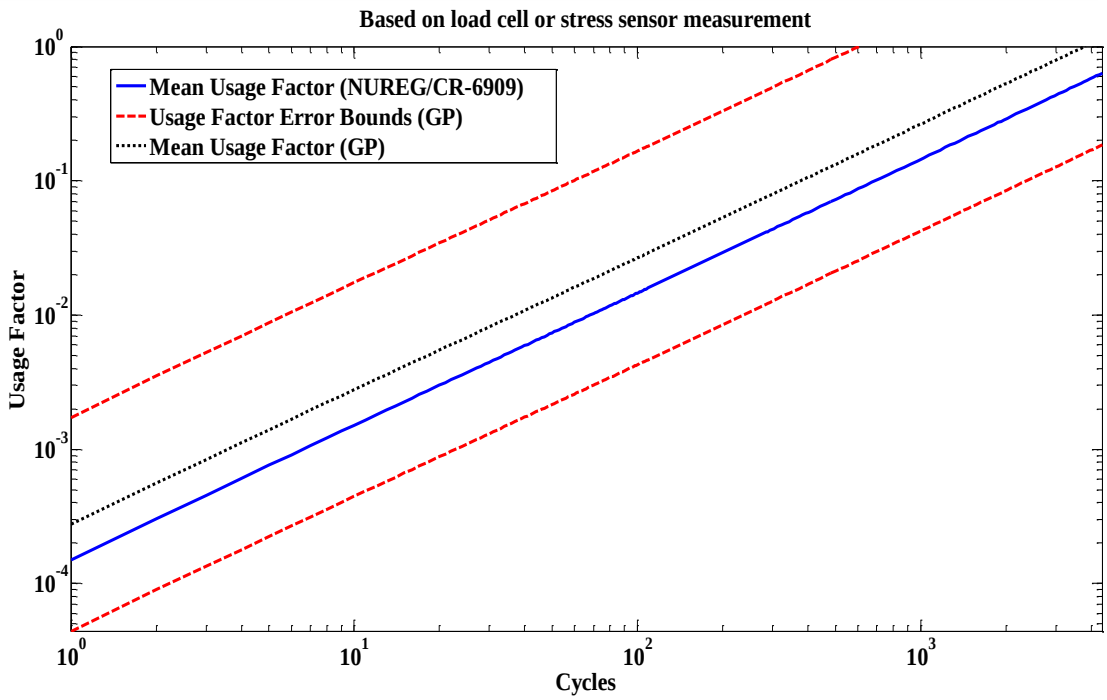

Figure 3. 7 Load cell measurement based real time estimated usages factor time history for the high purity water fatigue test (F11) using both NUREG-6909 based approach and GP based approach.

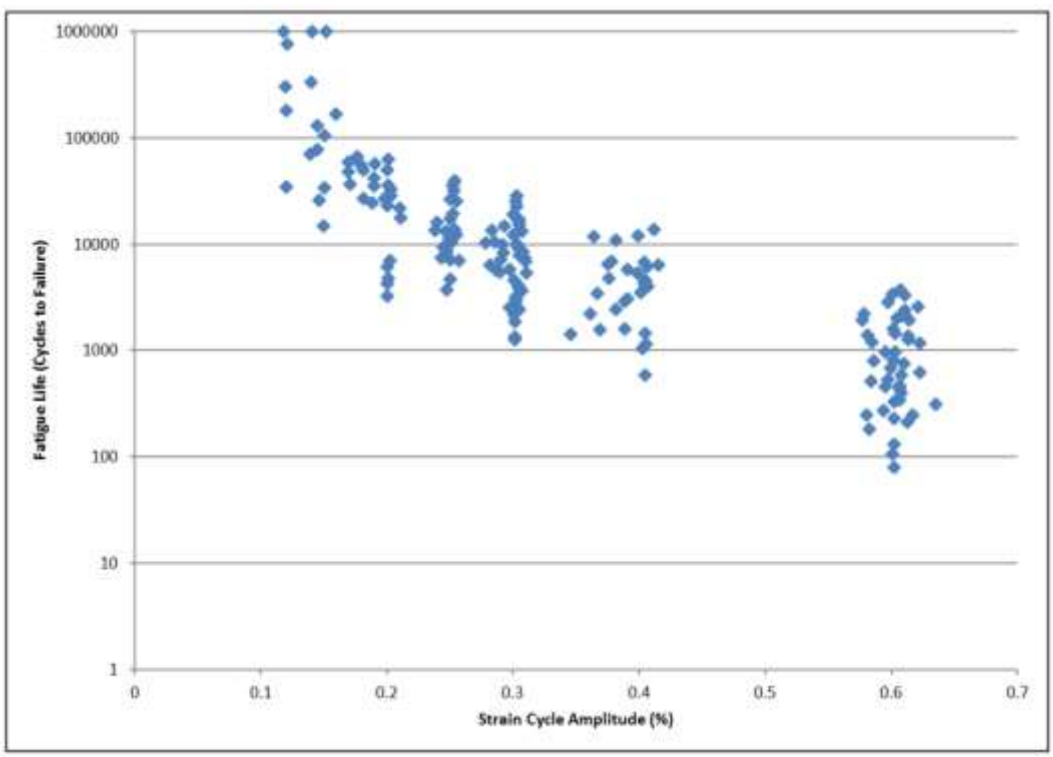

Figure 3. 8 Strain Amplitude vs Fatigue Life for stainless steel in PWR high temperature water.

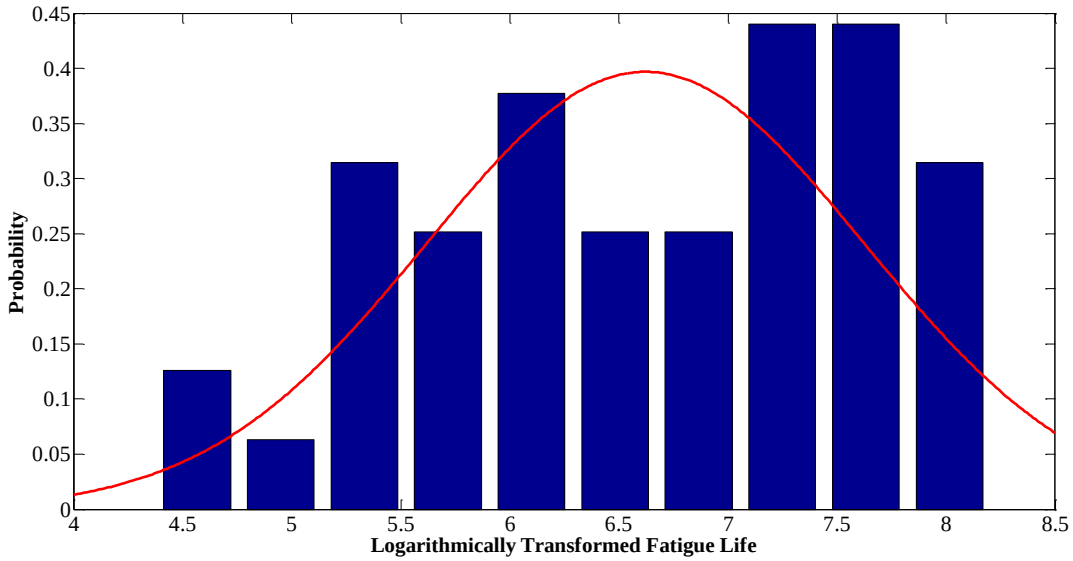

Figure 3. 9 Example histogram and probability density function of logarithmically scaled fatigue life approximately at 0.6 % strain amplitude for PWR data shown in Figure 3.8.

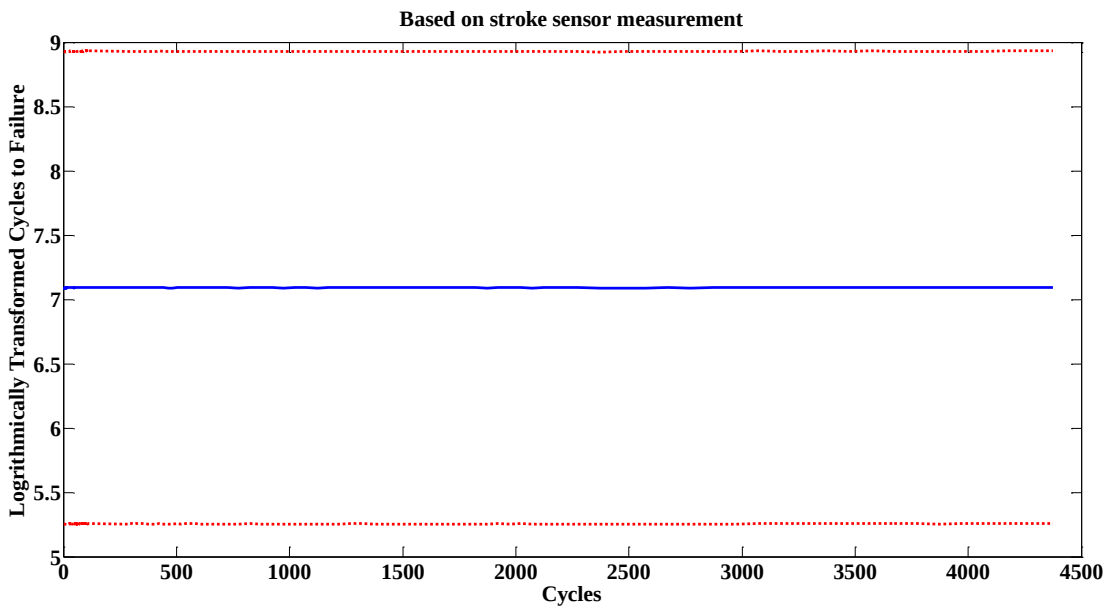

Figure 3. 10 GP estimated logarithmically scaled mean cycle to failure and associated 2σ confidence bound as estimated at any given fatigue cycle.

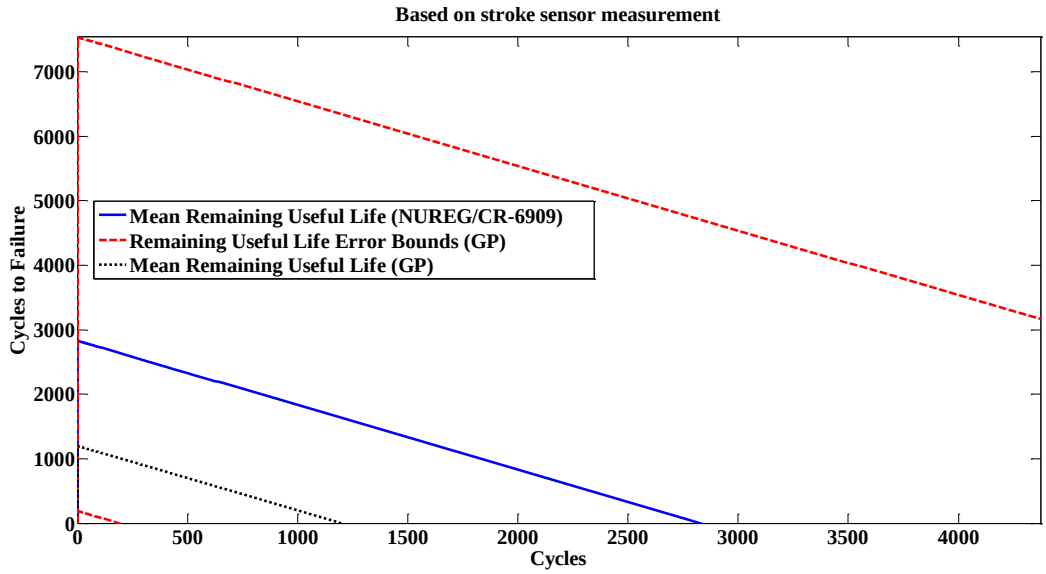

Figure 3. 11 Stroke sensor measurement based real time forecasted fatigue life for the high purity water fatigue test (F11) specimen at any given fatigue cycle.

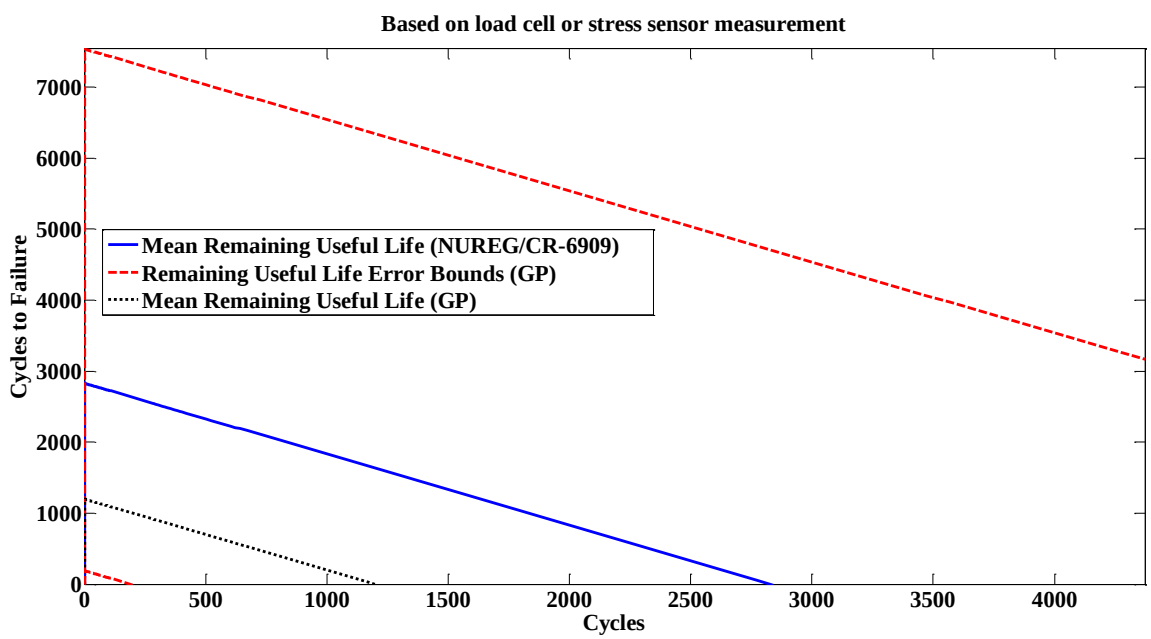

Figure 3. 12 Load cell sensor measurement based real time forecasted fatigue life for the high purity water fatigue test (F11) specimen at any given fatigue cycle.

3.3.2 PWR water and elevated temperature live fatigue test

A further test was run on a 316 stainless steel sample using water at 300° C with water chemistry more reflective of a PWR environment. For the purpose the water chemistry was maintained with following parameters: with gauge area target temperature of 300°C, water chemistry: 1000 ppm B as H_3BO_3, 2ppm Li+ as LIOH, 20% H_2/Bal N_2 cover gas and DO < 5ppb, Ph 6.3, conductivity $\leq$ 23 uS/cm. The test was run in the same set-up as the high purity water test previously discussed. Again, the same online monitoring hardware-software system was employed to monitor fatigue usage factor and remaining useful life for the test in real time. Again, stroke and load were collected, although only the data from the stroke sensors (measuring equivalent strains) sensor are discussed here, as that would more than likely be the setup in a real nuclear reactor, where strain can easily be measured. The test was cut short after 499 cycles as an anomaly was discovered in the testing setup. Text files were again collected intermittently for each cycle, from which peak and valleys for stroke were determined. As with the previous test, the intermittently collected stroke was converted to strain using equation 3.15. This intermittent strain history is show in figure 3.13. Again, using the same methodology as in the previous test, strain rate was calculated from the strain amplitudes and used, in conjunction with temperature and dissolved oxygen content, to determine an environmental fatigue correction factor (F_{en_i}). Figure 3.14 shows these results for each cycle calculated in real time for all 499 cycles. It can be noted that the time history remains flat, again due to the constant strain amplitude causing a constant strain rate. Temperature and dissolved oxygen content were also kept constant throughout the test.

The mean in-air fatigue life was found to determine an in-air mean usage factor by using Eq. 3.1 and 3.2. This was used in conjunction with the F_{en_k} to determine a mean fatigue life and usage factor according to the NUREG method. This method is appropriate; however it lacks a scope to include the effect of large scatter in fatigue life. To alleviate these issues again, the GP based approach discussed above was used to determine bounds for fatigue life and thereby usage factor based on historical PWR strain amplitude- fatigue life data. This uses the same process (Eq. 3.4-3.11) as the previous test. This process is assumed valid as the normal distribution is followed by the data used here, which is the same data used in the previous test. Figure 3.15 shows the real time estimated mean and corresponding error bounds for (taken from the GP) for logarithmically transformed fatigue life. Much like figure 3.14, these values are flat due to the constant strain cycles. Figure 3.16 shows the correspondingly estimated usage factor time histories. Again, we see that both the GP and NUREG based usages factor fall well within the GP estimated confidence bounds, again validating both methods, while also providing valuable confidence interval data to account for scatter resulting from microstructure variability. Again, a linear regression was employed for determination of remaining useful life. The time history for remaining useful life is shown in figure 3.17.

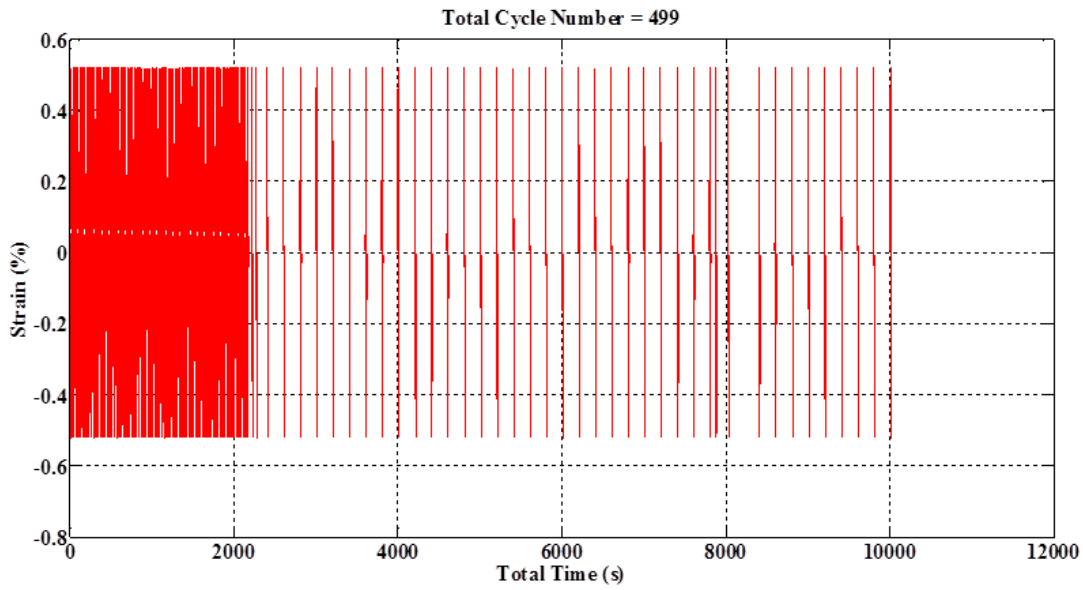

Figure 3. 13 Intermittent transformed cyclic strain history for the LWR water fatigue test (F12) using stroke-strain mapping.

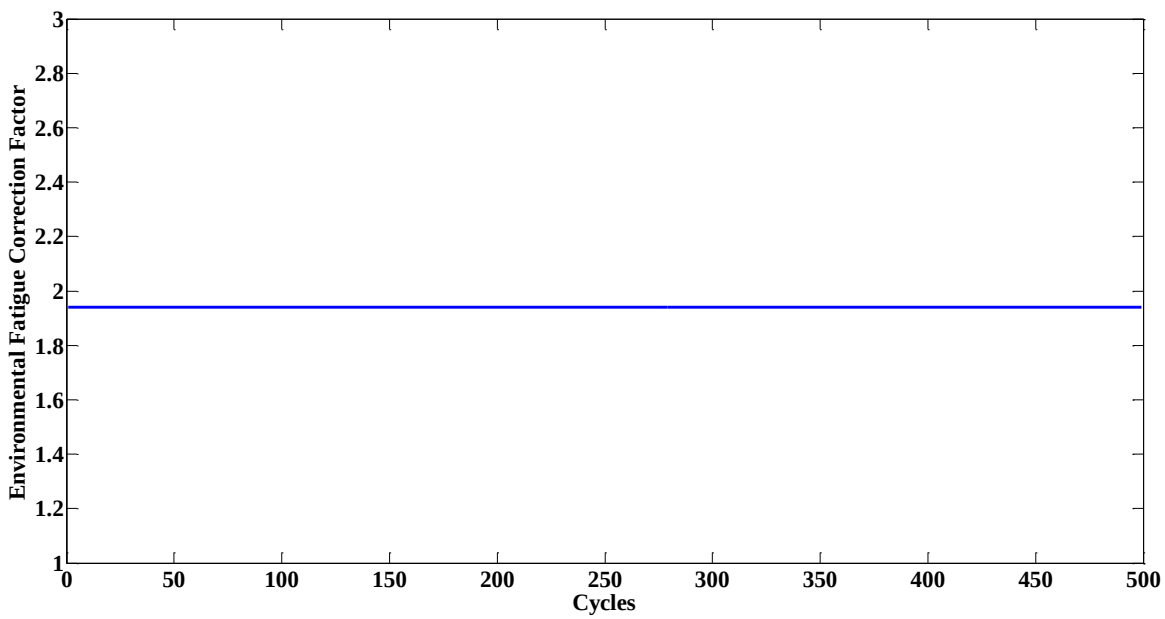

Figure 3. 14 Time history of environmental correction factor F_{en_i}.

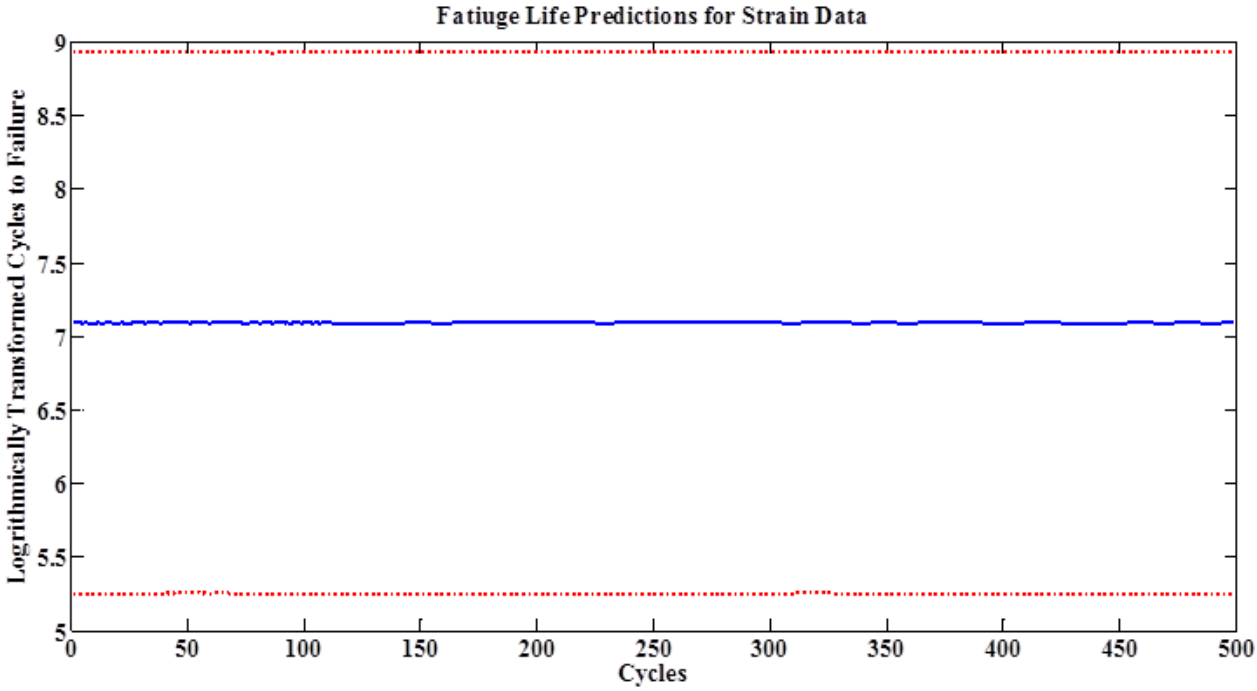

Figure 3. 15 GP estimated logarithmically scaled mean cycle to failure and associated 2σ confidence bound as estimated at any given fatigue cycle.

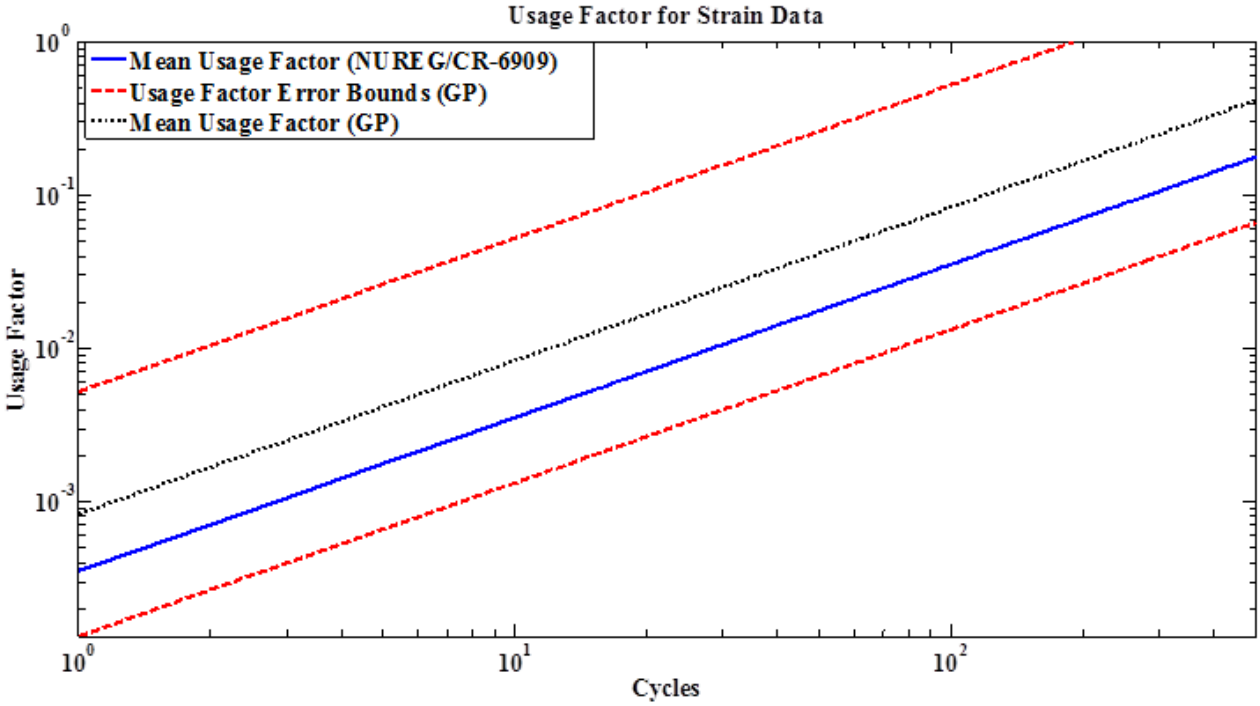

Figure 3. 16 Stroke sensor measurement based real time estimated usage factor time history for the PWR water fatigue test (F12) using both NUREG-6909 based approach and GP based approach.

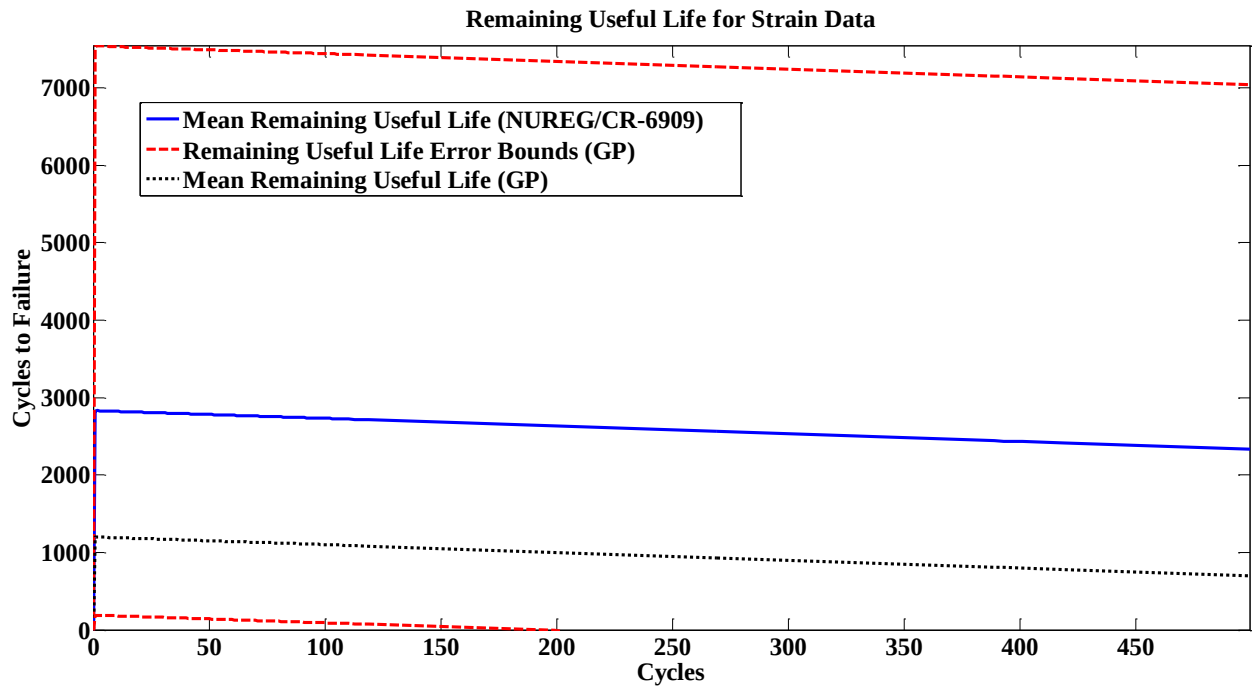

Figure 3. 17 Strain gage sensor measurement based real time forecasted fatigue life for the PWR water fatigue test (F12) specimen at any given fatigue cycle.

3.3.3 In-air and room temperature live fatigue test

A further test was run on a 316 stainless steel sample in a room temperature air environment. The test was run in an in-air set up, which provided added advantage of directly measuring the spacemen gage area strain using an extensometer. The test was conducted under room temperature condition. Compared to the previous two discussed test cases there was no need for a stroke to strain conversion. Text files were again collected continuously for each cycle, from which peak and valleys for strain were determined. Unlike the previous two cases in the present case, the data were collected continuously for each individual cycle. The test was run to failure, which occurred at 9096 cycles. Again here, imagining a similar real reactor condition where strain can easily be monitored, in the present discussed case, only strain data was used in estimation of usage factor and remaining useful life. This strain history is show in figure 3.18.

The mean in-air fatigue life was found to determine an in-air mean usage factor by using equations 1 and 2. This was used to determine a mean fatigue life and usage factor according to the NUREG method. Again, the GP based approach was used to determine bounds for fatigue life and thereby usage factor based on historical in-air strain amplitude- fatigue life data. This uses the same process (Equations 3.4-3.11) as the previous test. This process utilized in- air strain amplitude- fatigue life data from the JNES report: JNES-SS-1005 [14] and the taken strain-life data is shown in Figure 3.19. The same Gaussian Process was run on this set of data; however in-air historical data was used instead. Figure 3.19 shows data used to model the scatter, while figure 3.20 shows the example histogram and corresponding probability distribution function for .2% strain. This figure confirms that the scaled data approximately

follows a Gaussian or Normal Distribution. Again, a similar process was used to determine a mean and error bounds for fatigue life. Figure 3.21 shows the real time estimated mean and corresponding error bounds for (taken from the GP) for logarithmically transformed fatigue life. Much like figures 3.10 and 3.15, these values are flat due to the constant strain cycles. The fatigue life values were used to determine real time usage factor. Figure 3.22 shows these results of usage factor plotting by using both GP and NUREG based approaches. Again, we see that the NUREG and GP based approach estimate similar mean usages factor history, again validating the GP based methods, while also providing valuable confidence bounds to account for scatter resulting from microstructure variability. Again, a linear regression was employed for determination of remaining useful life. The time history for remaining useful life is shown in figure 3.23.

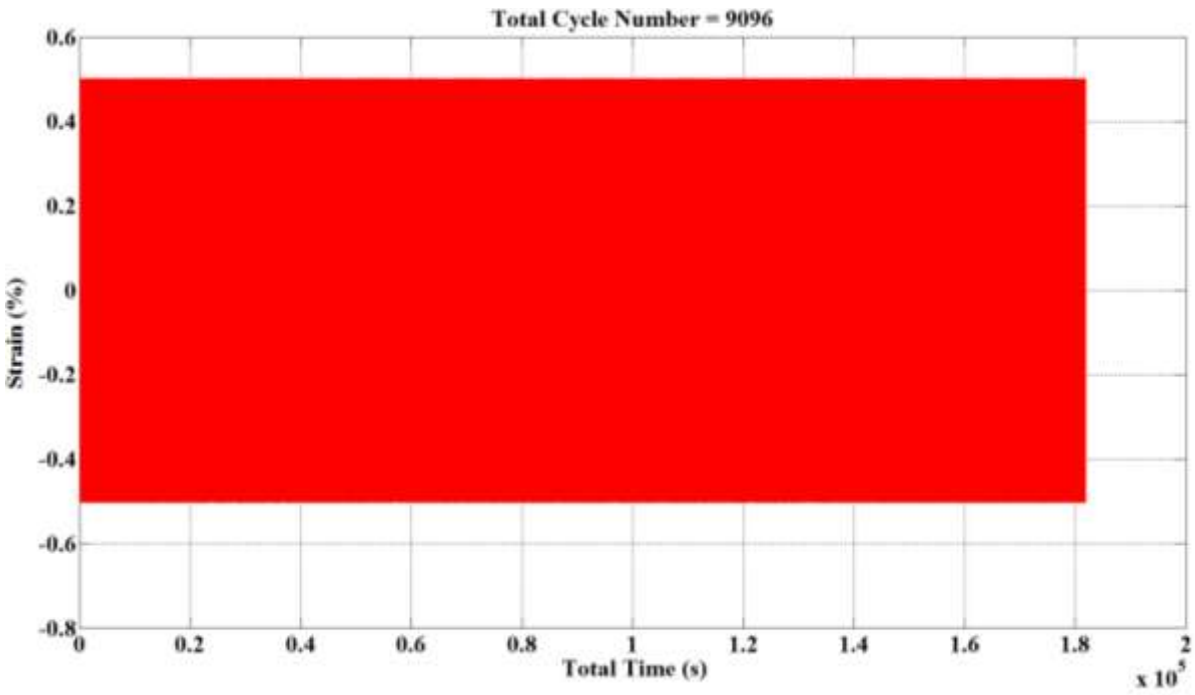

Figure 3. 18 Cyclic strain history for the in air fatigue test (F09).

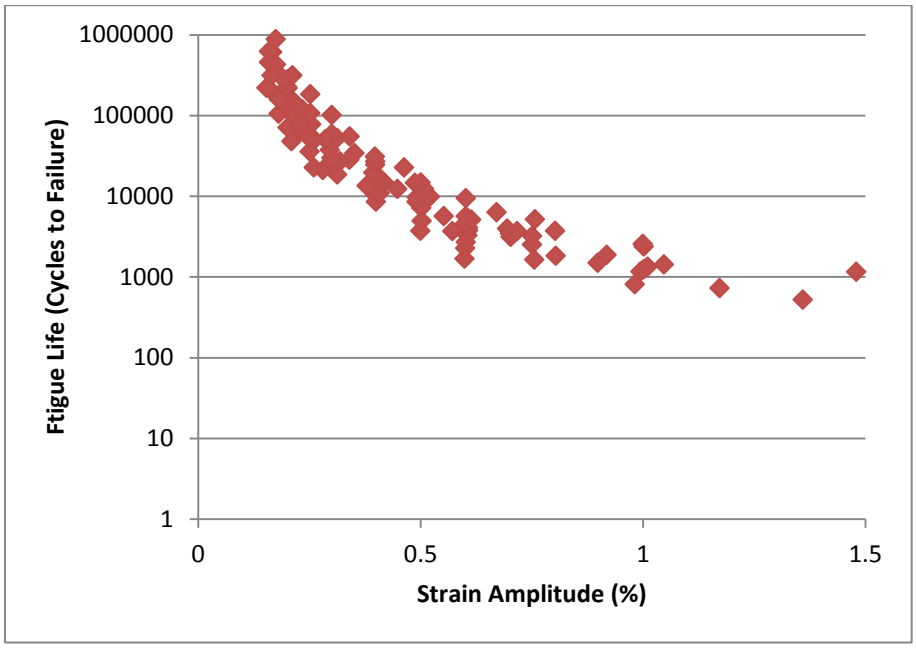

Figure 3. 19 Strain amplitude vs in-air test fatigue life for stainless steel .

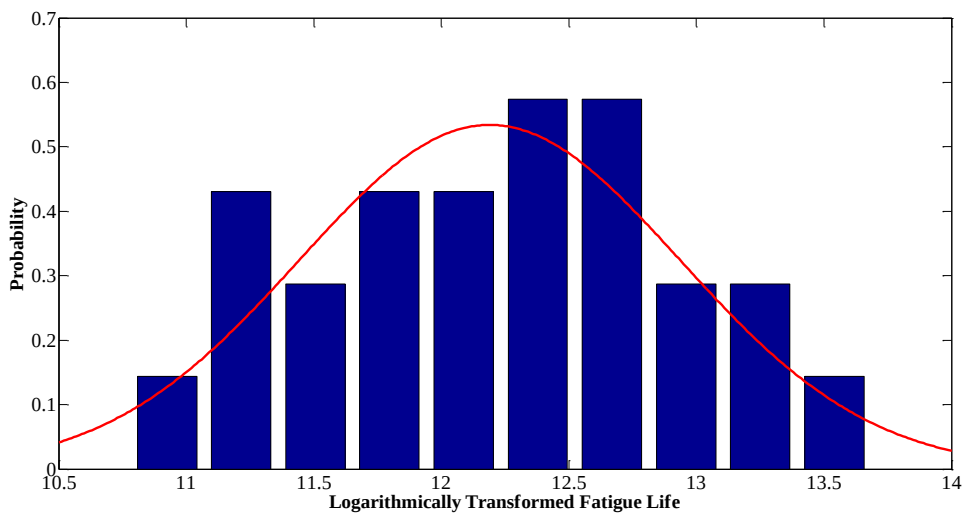

Figure 3. 20 Example histogram and probability density function of logarithmically scaled fatigue life approximately at 0.2% strain amplitude for in-air condition data shown in Figure 3.19.

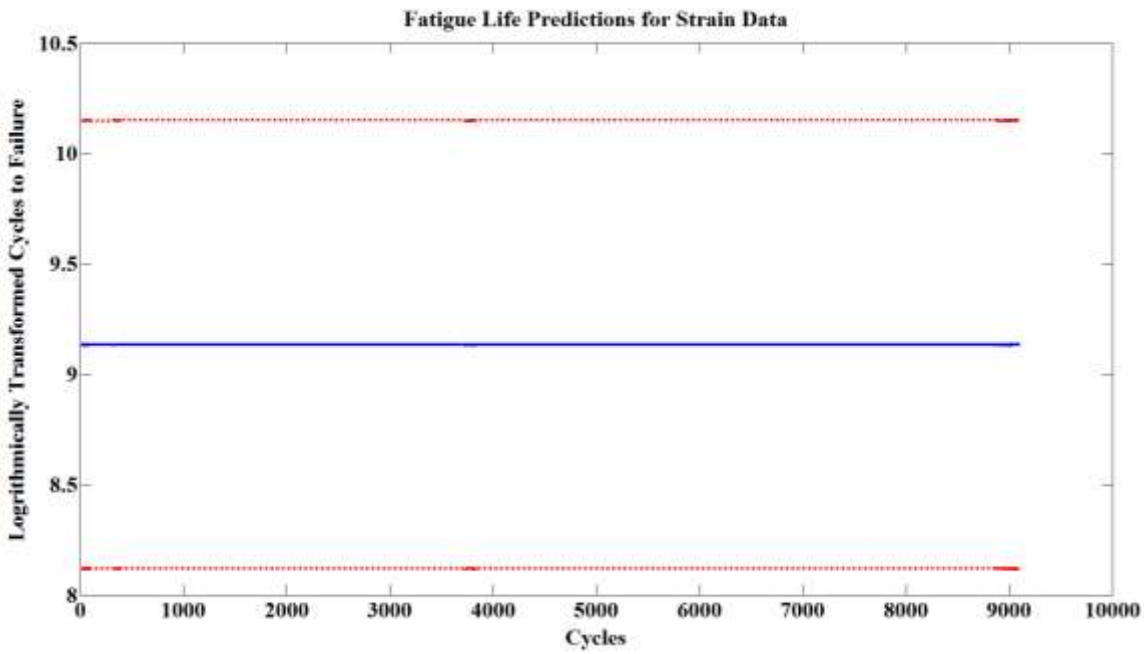

Figure 3. 21 Strain gage sensor measurement based real time forecasted fatigue life for the in air fatigue test (F09) specimen at any given fatigue cycle.

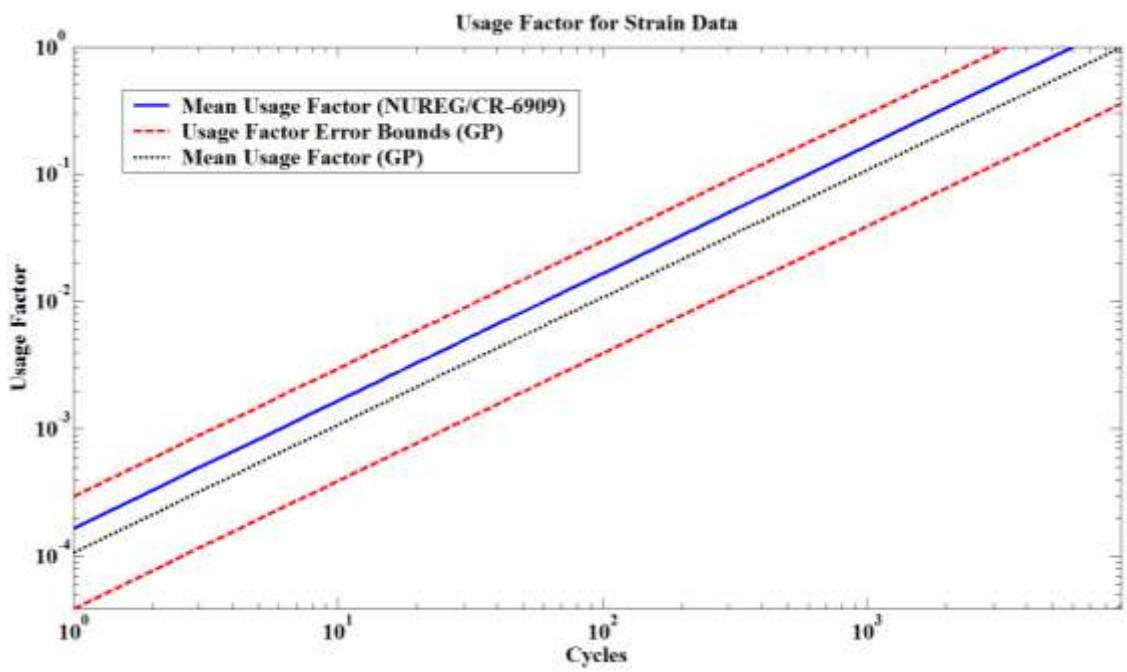

Figure 3. 22 Strain gage measurement based real time estimated usage factor time history for the in air fatigue test (F09) using both NUREG-6909 based approach and GP based approach.

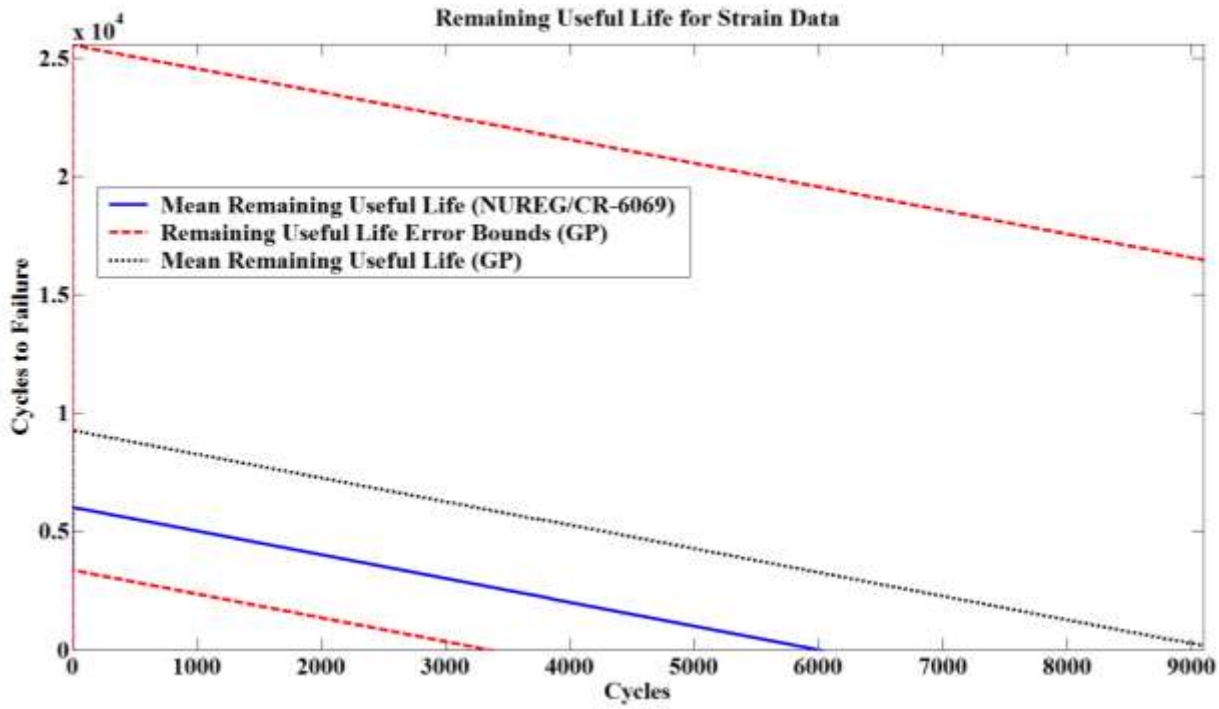

Figure 3. 23 Strain gage sensor measurement based real time forecasted fatigue life for the in air fatigue test (F09) specimen at any given fatigue cycle.

3.3.4 Simulated random strain transients under PWR water condition

Finally, in order to simulate arbitrary random loading conditions in an actual reactor environment, MATLAB was used to create a series of triangular strain waves with pseudorandom amplitudes. Each cycle passes through zero and its positive and negative amplitude, allowing for a simple method of amplitude calculation. For the purpose 100 cycles with amplitudes between 0.2 % and 0.8% strain were generated, each with a cyclic period of two years, a realistic approximation for a reactor refueling cycle. The simulated strain history is shown in Figure 3.24. The random cycles were input into text files which were then read by the program, simulating a live data collection process.

Using Eq. 3.14, and using the same temperature and dissolved oxygen levels as in the PWR water test, the environmental fatigue correction factor was calculated for each cycle. Due to the variance in cycle amplitude, the strain rate was not constant and was as such reflected in the time history, shown in figure 3.25. Compared to the previously discussed PWR water case of environmental fatigue correction factor, the present time history of environmental fatigue correction factor is not flat, as random cycles were used in the simulation. In the same way as the high purity water and PWR water tests, PWR historical data was referenced in the creation of a Gaussian Process. This historical data has already been shown to have the necessary normality for a Gaussian Process. The logarithmically transformed fatigue life (mean, upper and lower bounds) time history is shown in figure 3.26 as it would be estimated through GP in real time. While previous tests have provided flat data here, we see variability due to the variability in strain cycle amplitudes. Using the established process, usage factor curves were generated and these are shown in figure 3.27 for both GP and NUREG based approach. Similar as previous cases

the GP based approach not only estimated the mean usages factor but also the associated confidence bound for the discussed strain time history. This shows the microstructural variability associated scatter can be incorporated in the usages factor results. In addition, we can still use a linear regression to determine remaining useful life, and this has been employed with the results shown in figure 3.28. Due to the large oscillations, the first 10-20 cycles do not accurately reflect remaining useful life; however a general downward trend can be noted in all of the curves with shapes similar to results in earlier sections of this report. The downward trend may be difficult to see, due to poor scaling on the original graph, so a zoomed in error bound reflecting the true downward trending behavior is provided in figure 3.29 that shows the lower bound in Figure 3.28.

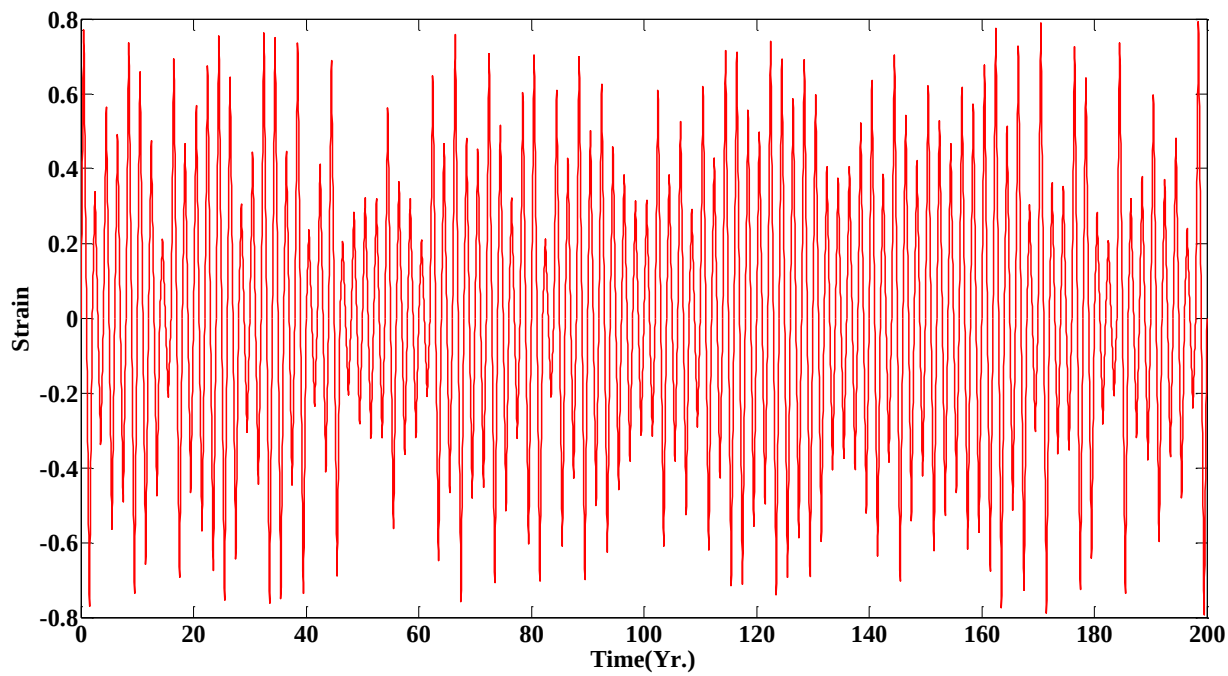

Figure 3. 24 Pseudorandom cyclic strain history.

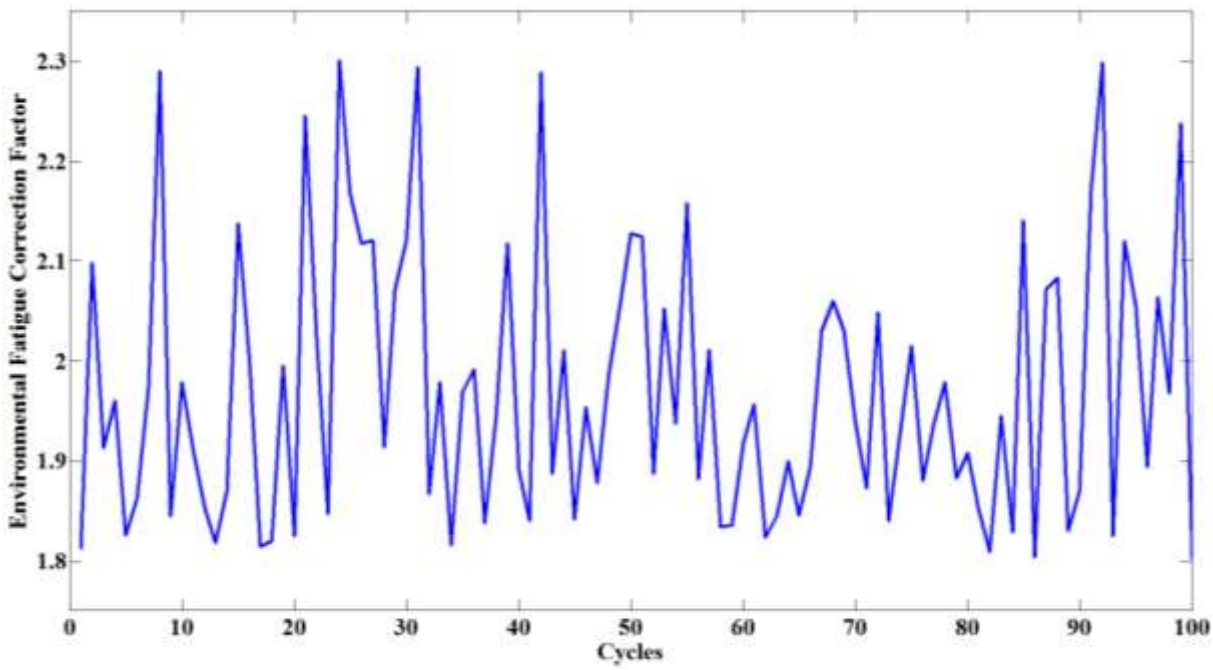

Figure 3. 25 Time history of environmental correction factor F_{en_i}.

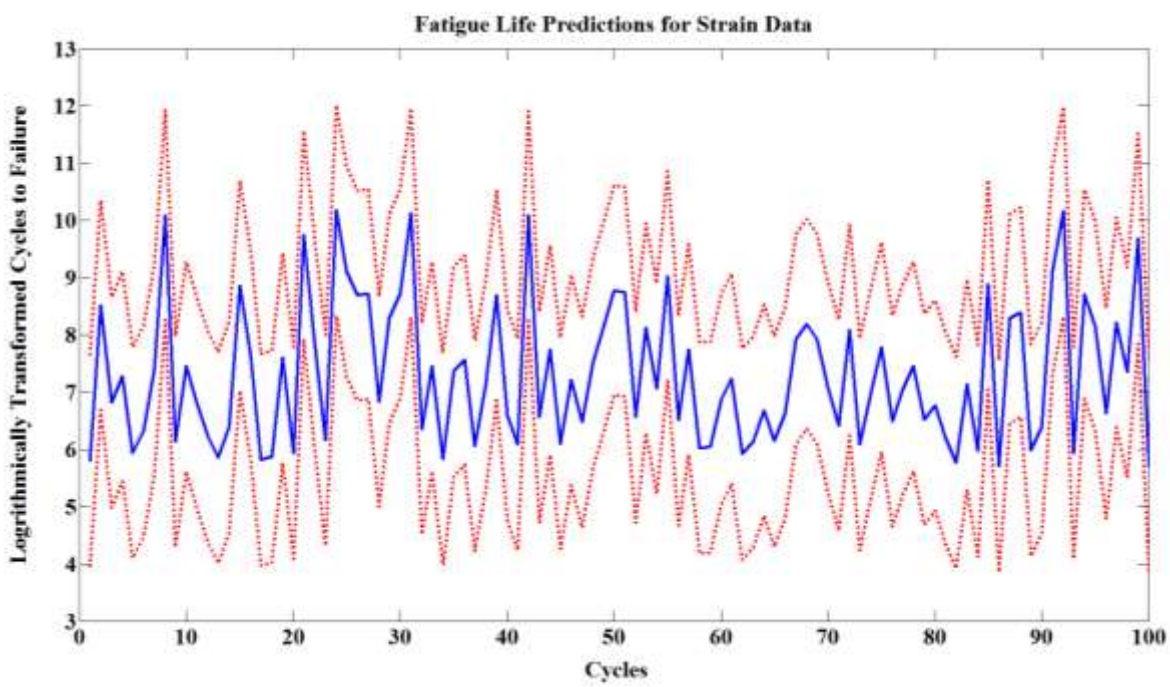

Figure 3. 26 Predicted logarithmically transformed time history of fatigue life (mean, upper and lower bounds), as it would be estimated through GP in a realistic reactor condition.

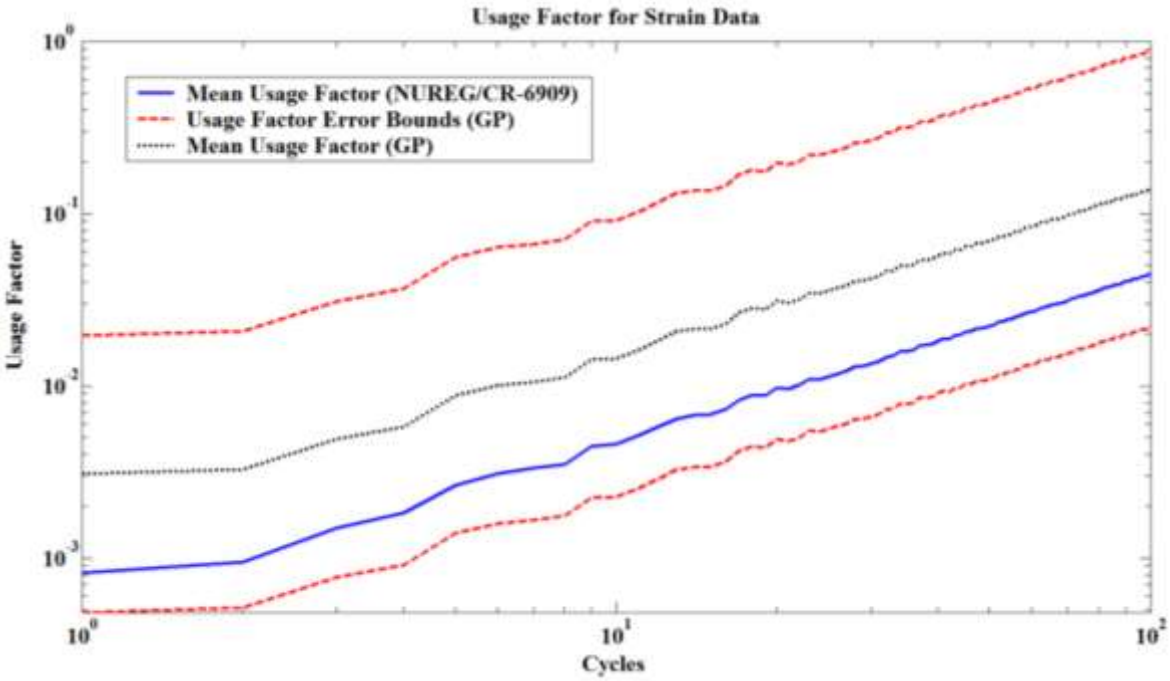

Figure 3. 27 Estimated usage factor time history for pseudorandom cycles using both NUREG-6909 based approach and GP based approach.

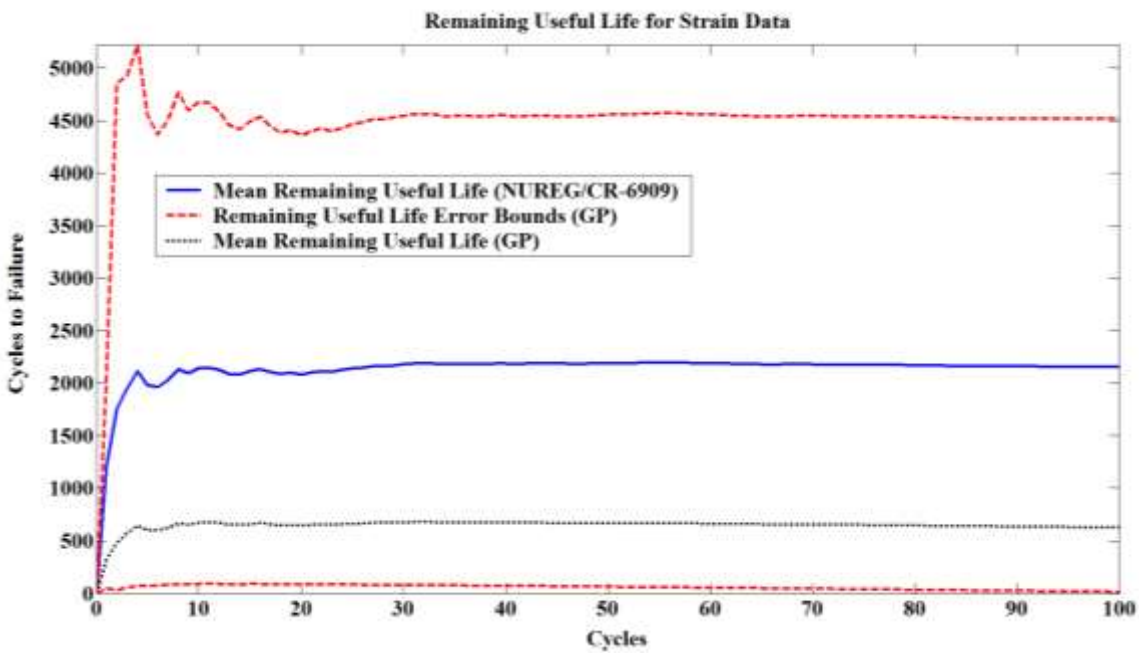

Figure 3. 28 Forecasted time history of fatigue life for random cycles.

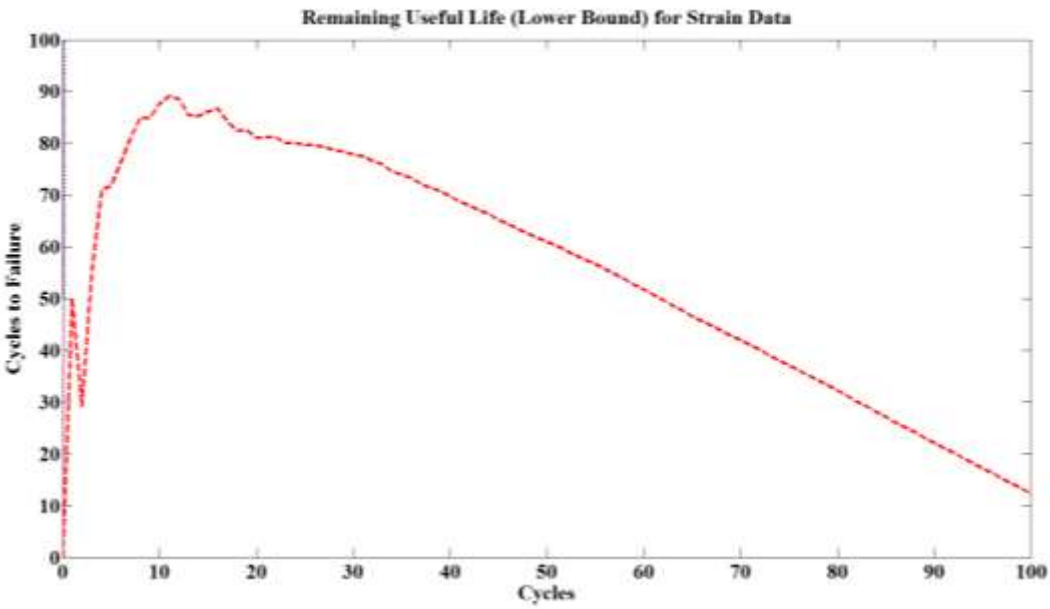

Figure 3. 29 Magnified Figure 3.28 showing clear decreasing trend of cycles to failure (zoomed to show lower bound in Figure 3.28).

3.4 Conclusions

Online fatigue monitoring and life forecasting tools can be used to accurately monitor fatigue damage in real time, that can reduces risk in operating nuclear reactors and allows for more current, accurate knowledge of remaining useful life. In the present work a Gaussian Process based probabilistic and NUREG based deterministic framework is discussed to estimate both the time to failure and usage factor in real time. This approach will help for more accurate component life monitoring in real time and hence will help in efficient management of nuclear reactor component life cycles improving both safety and economic benefits.

The proposed framework validated against simplified laboratory scale live tests and using simulated complex transients. The presented research results are based on our preliminary efforts on real time and probabilistic fatigue monitoring of nuclear reactor components, and need advanced validation.

References

1. Mohanty, S., Structural Health Monitoring and Condition Based Fatigue Damage Prognosis of Complex Metallic Structures, PhD Thesis, Arizona State University, Tempe, Arizona, 2010.

2. Mohanty S., Chattopadhyay A., Wei J., Peralta P., Unsupervised time-series fatigue damage state estimation of complex structure using ultrasound based narrowband and broadband active sensing. Journal of Structural Durability and Health Monitoring, 2009, 5(3):227-250.

3. Mohanty, S, Chattopadhyay, A., and Peralta, P., "Adaptive residual useful life estimation of a structural hotspot." Journal of Intelligent Material Systems and Structures, 2010, 21(3): 321-335.

4. Bakhtiari S., Mohanty S., Prokofiev I., Tregoning R., Condition based prognostics of passive components – a new era for nuclear power plant life management, International Atomic Energy Agency conference, 2012, IAEA-CN-194-097.

5. International Atomic Energy Agency, Advanced surveillance, diagnostic and prognostic techniques in monitoring structures, systems and components in nuclear power plants. IAEA Nuclear Energy Series, 2013, NP-T-3.14.

6. http://www.ne.anl.gov/facilities/eda/steamgen.html

7. Ljung L, System Identification Toolbox. The Mathworks, Inc., Massachusetts, 1995.

8. Rasmussen C., Williams C., Gaussian Processes for Machine Learning. MIT Press, Massachusetts, 2006.

9. Musallam, M., and Johnson., C. M., "An Efficient Implementation of the Rainflow Counting Algorithm for Life Consumption Estimation," IEEE Transactions on Reliability, 2012, 61(4): 978-986.

10. Carney, C. and Gillman. T., "Stress-Based Fatigue Monitoring: Methodology for Fatigue Monitoring of Class 1 Nuclear Components in a Reactor Water Environment," Electric Power Research Institute, 2011.

11. Chopra, O. K. and Shack, W. J., "Review of the Margins for ASME Code Fatigue Design Curve-Effects of Surface Roughness and Material Variability," Report, Argonne National Laboratory, September 2003, NUREG/CR-6815.

12. O. Chopra and G. L. Stevens. "Effect of LWR Coolant Environments on the Fatigue Life of Reactor Materials," United States Regulatory Commission, 2014, NUREG/CR-6909.

13. Guidelines for Evaluating Fatigue Analysis Incorporating the Life Reduction of Metal Components Due to the Effects of the Light-Water Reactor Environment for New Reactors, United States Nuclear Regulatory Commission, 2007, Guide 1.207.

14. Environmental Fatigue Evaluation Method for Nuclear Power Plants, Japan Nuclear Energy Safety Organization, March 2011, Report no. JNES-SS-1005.

15. Snelson, E., "Flexible and Efficient Gaussian Process Models for Machine Learning," Ph.D. Thesis, University of London, 2007.

16. Lawrence, N "Probabilistic Non-Linear Principal Component Analysis with Gaussian Process Latent Variable Models," Journal of Machine Learning Research, 2005, 6: 1783-1816.

17. Mohanty, S.., Das, S., Chattopadhyay, A., and Peralta, P., "Gaussian Process Time Series Model for Life Prognosis of Metallic Structure", Journal of Intelligent Material Systems and Structures, 2008, 20(8):887-896.

18. Mohanty, S., Chattopadhyay, A., Wei, J and Peralta, P., "Real time Damage State Estimation and Condition Based Residual Useful Life Estimation of a Metallic Specimen under Biaxial Loading", Structural Durability & Health Monitoring Journal, 2009, 5(1): 33-55.

19. Mohanty, S., Chattopadhyay, A., Peralta, P., and Das, S., "Off-Line and On-Line Fatigue Crack Growth Prediction Using Multivariate Gaussian Process, Journal of Experimental Mechanics, 2009

20. Chattopadhyay, A., and Mohanty, S., "Gaussian Process Damage Prognosis under Random and Flight Profile Fatigue Loading," Machine Learning and Knowledge Discovery for Engineering Systems Health Management, CRC Press, 2012.

21. Mohanty, S., Chattopadhyay, A., and Rajadas, John N. "Bayesian Nonlinear Model for Dynamic Strain Mapping and Real-time Damage State Estimation under Biaxial Random Fatigue Loading", AIAA Journal, 2012, 50 (4): 769-777.

22. Mohanty, S., Soppet, W. K., Majumdar, S. and Natesan, K. "Report on Assessment of Environmentally-Assisted Fatigue for LWR Extended Service Conditions", March 2013, ANL/LWRS-13/3.

This page intentionally left blank

Nuclear Engineering Division
Argonne National Laboratory
9700 South Cass Avenue, Bldg. 208
Argonne, IL 60439

www.anl.gov

Argonne National Laboratory is a U.S. Department of Energy
laboratory managed by UChicago Argonne, LLC